Linear electrooptic microscopy : applications to micro and nano-structured materials

Duc Thien Trinh

Linear Electrooptic Microscopy: Applications to micro- and nano-structured materials

By

TRINH Duc Thien

Laboratoire de Photonique Quantique et Moléculaire

A Thesis submitted to

ÉCOLE NORMALE SUPÉRIEURE DE CACHAN

for the degree of Doctor of Philosophy

in the subject of Physics

Examining Committee:

Sophie BRASSELET	Research Director (Institut Fresnel, CNRS)	Referee
Germano MONTEMEZZANI	Professor (Univ. Paul Verlaine, Metz)	Referee
Ady ARIE	Professor (Univ. Tel-Aviv, Israel)	Examinator
Vasyl SHYNKAR	Researcher (LPQM, CNRS)	Examinator
Joseph ZYSS	Professor (ENS Cachan)	Supervisor

Cachan, 25th March, 2015

Acknowledgements

I would not have been able to complete this thesis without the support and encouragement of numerous individuals and institutions. It is my pleasure to express my sincere gratitude for all of the help and support.

First of all, I would like to express my thanks and gratitude to my supervisors, Professor Joseph ZYSS and Doctor Vasyl SHYNKAR for giving me an opportunity to join their research group as a PhD student. Their patience, optimism, frequent encouragement and guidance for the work help me to finish the hard work required for my thesis. Thank for always making time for me whenever I had questions or issues and for sharing your huge knowledge.

As well, I would like to express my sincere thanks to many peoples for their contributions to my project. I would like to thank Professor Bruno LE PIOUFLE, Professor Ady ARIE (Tel Aviv University, Israel), Professor Wieslaw KROLIKOWSKI (Australian National University, Australia) for their help and collaboration. Their valuable suggestions helped me to develop an appropriate approach towards my results. I would like to thank Mr. Joseph LAUTRU and Dr. Ludovic MAYER for their enthusiastic help, collaboration and helpful assistance.

I would like to offer my sincere thanks to Professor Isabelle LEDOUX-RAK and Professor LAI Ngoc Diep for their enthusiastic help, support and giving me a change to work in Laboratoire de Photonique Quantique et Moléculaire (LPQM). Even though very busy, Diep spent a lot of time to help and give me great suggestions which help me overcome my issues in both work and life.

I would like to thank Aurélia OLIVIER-KAISER and Clément LAFARGUE for their help and encouragement throughout the duration of my PhD. I am thankful to all members of LPQM laboratory, D'Alembert Institute, Department of Physics and Doctoral School (EDSP) for creating a great environment and for all your assistance.

I am grateful for the financial support from the Scholarship Foundation of Vietnamese Government (322 Project), and support from the Faculty of Physics, Hanoi National University of Education, Vietnam.

I would like to express my sincere thanks and pleasure to Vietnamese friends in Cachan for all your encouragement, support and sharing through the hard life of a PhD student.

Finally, I reserve my deepest gratitude to my parent, parent-in-law, my wife, my brothers and sister for their trust, support and encouragement with unconditional love.

Abstract

Complementing Second-Harmonic Generation (SHG) microscopy, a new home-made nonlinear microscope named Pockels Linear Electro-Optical Microscopy (PLEOM) based on the linear electrooptic (Pockels) effect, has been developed and used to map the second-order susceptibility $\chi^{(2)}$ of non-centrosymmetric materials with high sensitivity due to a stabilized interferometric homodyne detection scheme [1, 2]. This enables PLEOM to detect the electrooptic phase retardation of light resulting from the variation of the refractive index of nonlinear materials down to 10^{-6} radian and to investigate nonlinear materials at the nano-scale [3] towards applications in imaging of biological samples and tracking of labels therein. With PLEOM, a new imaging method allows to access besides the amplitude, the no less crucial phase response, which is not readily amenable to classical SHG microscopy. In the frame of this dissertation, we have further extended the range of applications of PLEOM to investigate nonlinear materials and structures from nano- to millimeter-scale.

Firstly, we have proposed and demonstrated a new approach towards the full vector determination of the spontaneous polarization of single ferroelectric nano-crystals used as SHG nano-probes. This method allows to remove the ambiguity inherent to earlier polarization-resolved SHG microscopy experiments, and has permitted full determination of the orientation of single domain ferroelectric nano-crystals. The electrooptic phase response obtained in the form of phase images and polarization diagrams yields the full orientation in the laboratory frame of randomly dispersed single nano-crystals, together with their electric polarization dipole. The complete

vector determination of the dipole orientation is a prerequisite to important applications including ferroelectric nano-domain orientation, membrane potential imaging and rotation dynamics of single biomolecules, especially by using a new low-cost non-invasive imaging method with a low intensity illumination beam.

The ferroelectric domain pattern of periodically poled $KTiOPO_4$ and of a two-dimensional decagonal quasi-periodic $LiNbO_3$ nonlinear crystal was determined by local measurement of their electro-optically induced phase retardation. Owing to the sign reversal of the electrooptic coefficients upon domain inversion, a 180° (π) phase shift is observed across domain barriers between domains with opposed orientations. PLEOM allows to reveal the nonlinear and electrooptic spatially modulated patterns in ferroelectric crystals in a non-destructive manner and to determine their poling period, duty cycle and short-range order as well as to detect local defects in the domain structure, such due to incomplete poling.

In addition, we have also proposed and demonstrated a new method, based on the voltage dependence of the electrooptic dephasing, to mimic the membrane potential in cells, working at this stage on nonlinear dye containing phospholipidic membranes, grown in a microfluidic set-up.

Résumé

Nous avons développé une nouvelle méthode de microscopie par effet électro-optique linéaire (effet Pockels), dite PLEOM, permettant de cartographier la susceptibilité du deuxième ordre $\chi^{(2)}$ d'un matériau noncentrosymétrique [1, 2]. Cette méthode est complémentaire de la microscopie de génération de seconde harmonique, et s'en distingue par différents aspects physiques et pratiques. Grâce à une détection interférométrique stabilisée, le retard de phase provoqué par une variation d'indice locale du matériau non-linéaire sous l'effet d'un champ électrique est détecté à 10^{-6} radians près, ouvrant la voie à l'imagerie d'échantillons biologiques ou au suivi du mouvement de nano-sondes [3]. PLEOM apporte un type de données nouveau, la "réponse en phase" du matériau, porteuse d'information physiques plus difficilement accessibles en microscopie biphotonique. Ce manuscrit décrit de nouveaux domaines de développement et d'application de PLEOM, qui a évolué vers une plateforme aux applications variées et multiéchelles, allant du nanométrique au millimétrique.

Nous avons tout d'abord montré comment déterminer le vecteur de polarization attaché à des nano-cristaux ferroélectriques uniques, en vue de leur utilisation comme nano-sondes. Cette nouvelle méthode permet, à notre connaissance de façon unique, de distinguer deux nano-cristaux mono-domaines d'orientations exactement opposées, dont les réponses en SHG ne peuvent pas être distinguées. Une image de phase électro-optique, combinée à un diagramme de polarisation, donne accès à l'orientation vectorielle d'un nano-cristal orienté aléatoirement dans le référentiel du laboratoire. Un verrou est ainsi levé pour des applications comme l'imagerie de

nano-domaines ferroélectriques, celle de potentiels électrochimiques membranaires, où l'étude de la dynamique de rotation de molécules. Deux spécificités remarquables de PLEOM en font une méthode d'avenir : la faible intensité de pompage qui assure une bien meilleure bio-compatiblilité ainsi que la simplicité de la source laser continue utilisée.

Nous avons ainsi pu utiliser PLEOM pour caractériser les domaines ferroélectriques d'un cristal de $KTiOPO_4$ périodiquement réorienté en vue d'un quasi-accord de phase, ainsi que ceux d'un cristal bidimensionnel quasi-périodique de $LiNbO_3$. Un retournement clair de la phase de 180° est observé au travers des parois de domaines, dont les coefficients électro-optiques apparaissent opposés dans le référentiel du laboratoire. PLEOM se présente ainsi comme un outil de caractérisation non destructif des propriétés de ces cristaux artificiels dont les motifs et les défauts (tels qu'une orientation localement incomplète) ont été caractérisés spatialement, et permet mesurer localement leurs propriétés non-linéaires, dont le caractère tensoriel permet d'aller au-delà des informations acquises en microscopie classique.

En outre, nous avons fait la preuve de principe d'une nouvelle expérience biomimétique, visant à étudier les potentiels membranaires cellulaires, en utilisant PLEOM sur des membranes phospholipidiques créées sur puce micro-fluidique et dopées en colorants.

List of Publications

- **D. T. Trinh**, L. Mayer, Bassam Hajj, J. Lautru, J. Zyss, and V. Shynkar, *Full determination of single ferroelectric nanocrystal orientation by Pockels electrooptic microscopy*, Applied Optics, accepted (2015).

- **D. T. Trinh**, V. Shynkar, A. Arie, Y. Sheng, W. Krolikowski, and J. Zyss, *Electro-optical interferometric microscopy of periodic and aperiodic ferroelectric structures*, Laser Photonics Rev. 9, No. 2, 214-223 (2015).
  DOI: 10.1002/lpor.201400122.

- **D. T. Trinh**, V. Shynkar, and J. Zyss, *Linear electro-optical scattering from ferroelectric nanocrystals*, Proc. SPIE 9136, 91361J (2014).
  DOI: 10.1117/12.2051911.

Contents

List of Figures

List of Tables

1

Introduction

1.1 Nonlinear Optics

Nonlinear optics embeds the study of the diverse phenomena that result from a change in the optical properties of a material in the presence of light or applied voltage. Nonlinear optical (NLO) effects are accounted for at an upstream level by considering the response of dielectric materials to an applied electric field or intense light beam at the atomic level. The propagation of an optical wave through a material produces a variation in the spatial and temporal distribution of electronic charges attached to atoms and molecules, as a result of their interaction with an optical field. The main effect of such strong interaction is a displacement of the valence electrons from their rest orbits. This perturbation creates a polarization of the material, which, in addition to the linear component accounting for linear properties

(i.e regular index and absorption), depend in a nonlinear fashion on the electric field of the optical beam. Most nonlinear effects, require a sufficiently intense laser beam so as to modify the higher order nonlinear optical properties of a material up to a measurable level. Thus, the first observation of a nonlinear effect was the discovery of second-harmonic generation (SHG) by Franken et al. in 1961 [4], shortly after the demonstration of the first laser by Maiman in 1960 [5]. The success of this experiment directly relied on the enormous increase in the illumination power supplied by the then new laser sources that allowed to reach power densities surpassing 10^9 W/cm^2, which corresponds to an optical electric field amplitude above of 10^6 V/cm that became available. NLO materials have been considered as future "optical semiconductors", and the search for new materials and their application from bulk to nano-scale has remained still very active.

1.1.1 Research on Nonlinear Optics

Since the first observation of SHG in a single mineral dielectric crystal of Quartz by Franken et al. [4], the early work in nonlinear optics concentrated on second-harmonic generation, including both theoretical principles and experiments [6]. At a quite early stage in this research, hundreds well known NLO crystals, inorganic materials belonging to the ferroelectric class and featuring a the spontaneous dielectric polarization because of the lack of inversion symmetry center, emerged as relevant candidates, with such by now well documented crystals as KDP, KD*P, $LiNbO_3$, KTP, etc... Indeed, the quadratic non-linearity is non-zero only for the smaller group of materials that lack inversion symmetry center, which are called non-centrosymmetric materials. A majority of materials being centro-symmetric, their second-order susceptibility $\chi^{(2)}$ cancels, and therefore their first non-zero nonlinearity is governed by the third-order susceptibility $\chi^{(3)}$. In contrast, due to their built-in non-zero static polarization, ferroelectric phases are inherently non-centrosymmetric and therefore endowed of a non-zero quadratic susceptibility which, as we shall further justify, can be fairly high.

SHG in the optical range is somewhat similar to harmonic generation at radio frequencies, with the significant difference that the optical wavelength is much smaller than the dimension of the interaction volume inside the nonlinear media. In nonlinear optics, this implies additional phase-matching conditions, ensuring that the phase velocity of the fundamental and second-harmonic waves are equal throughout the nonlinear material, or in other words, that the frequency dispersion has to be somehow compensated. Kleinman [7], Giordmaine [8], and Maker et al. [9] demonstrated that the phase-matching condition could be met in birefringent crystals by ensuring via adequate polarization of the interacting beams, that the crystal birefringence compensates the dispersion. Besides the use of birefringent crystals, another way to deal with phase-matching conditions had been theoretically predicted as early in 1962 by Armstrong et al. [10], where by the second-order susceptibility $\chi^{(2)}$ of nonlinear materials is spatially modulated. This eventually lead to the actual implementation of quasi-phase matched crystals which took thirty years. The first 1D quasi-phase matched crystal was fabricated by Jundt et al. based on a periodically poled $LiNbO_3$ crystal [11]. The fabrication method of quasi-phase matched crystal by an electric field poling method has opened since a new research domain at the border of optical and material sciences, bearing the promise and realization of numerous applications based on the tailoring of artificial domain structures in one- or two-dimensions [12].

An important extension of the range of nonlinear optical phenomena occurred in 1965 when Wang et al. observed significant gain in a three-wave mixing experiment [13]. Following this demonstration, parametric amplification was observed in that same year by two-wave degenerate mixing in temperature-tuned single Lithium Niobate ($LiNbO_3$) crystals [14]. Following this advance, Harris reviewed the theory and devices aspects of parametric oscillators [15, 16] which are now well known in a broad field from applications for tunable sources known as optical parametric oscillators (OPO) all the way to the generation of photon-pairs for fundamental studies in quantum entanglement [17, 18].

At an early stage, Kurtz et al. developed a powder SHG test technique that

permits a rapid semi-quantitative scanning of the NLO efficiency of materials at an early stage of development, in powder form, prior to the decision of starting a costly and possibly lengthy single crystal growth process [19]. Moreover, when applicative end-goals are at stake, it is not sufficient for candidate NLO materials to exhibit large larger $\chi^{(2)}$, but they must also satisfy secondary criteria, among which a high optical damage threshold, thermal stability and high optical homogeneity are the most important ones.

Also at an early stage, organic materials triggered a lot of interest, the first observation of SHG in such materials having been reported by Rentzepis and Pao in 1964 [20], with the demonstration of 3,4 benzpyrene and 1,2 benzanthracene based molecular crystals. In that wake of this demonstration, a detailed study of effect of molecular structure on optical SHG from organic crystals was reported by Gott in 1971 [21]. Over the two following decades, the study of nonlinear optical process in various organic molecules and crystals, and later in polymer systems due to their promising applications, has attracted a lot research groups and generated a wealth of scientific results [22, 23] which showed a number of advantages over inorganic materials towards NLO applications. In recent years, a large number of new organic compound materials with very large SHG response were proposed and demonstrated [24–27]. In this context, and further focusing on the secondary parameters related to the structural and operational robustness of the candidate nonlinear crystal, a number of simple inorganic-organic hybrid complexes were found to exhibit interesting ferrolectric properties at room temperature [28, 29], leading to the proposition of new NLO materials based on inorganic-organic hybrid compounds [30–32].

Although the relationship between optical second-harmonic generation and the electrooptic effect was pointed out by Kleinman as early as in 1962 [6, 7], It was only two year later that benzil was the first nonlinear crystal to display such relationship as shown by Heilmeier et al. [33]. A lot of NLO and electrooptic (EO) devices have been subsequently fabricated and applied.

Since 1974, when Hellwarth et al. first reported the integration of SHG and microscopy by imaging the SHG response from polycrystalline ZnSe [34, 35], nonlinear microscopy has blossomed into a whole new domain of microscopy. Developments in SHG microscopy allow to investigate NLO materials at the nano-scale and bear the potential of applications to high resolution imaging of biological objects. The field of SHG application to biological imaging has been pioneered by Freund in 1986 [36], with SHG microscopy now extended to whole-animal in vivo imaging [37, 38] by use of NLO molecules or crystals as SHG nano-probes.

1.1.2 Quasi-phase matching*

Let us recall the phase-matching condition of SHG in which an optical wave with frequency ω interacts with a nonlinear material through its second-order susceptibility so as to produce a polarization wave at the doubled frequency 2ω. The nonlinear effect being of the order of a weak perturbation to the linear response, the propagation length through the nonlinear media must be much longer than the wavelength of the fundamental beam, so that the conversion process can reach a sufficient yield. Since the nonlinear polarization wave which is at the origin of the nonlinear emission is forced by the square of the fundamental wave, it propagates with twice its wave-vector $k(\omega)$ as determined by n_ω, the refractive index of the medium at the fundamental wavelength as shown in Fig. 1.1a. The polarization wave then radiates a free second-harmonic (SH) wave which propagates at a wave-vector $k(2\omega)$ determined by $n_{2\omega}$, the refractive index of the media at the harmonic wavelength. The phase matching condition $k(2\omega) = 2k(\omega)$ imposes that $n_{2\omega} = n_\omega$. However, this condition conflicts with the monotonous growth of the index with the photon energy, that is $n_{2\omega} > n_\omega$ as a consequence of normal dispersion in most material. The fundamental and SH waves then propagate at different phase velocities as shown in Fig. 1.1a. As a result, SH waves generated from different parts of the NLO media

*This section is based on: [39, 40]

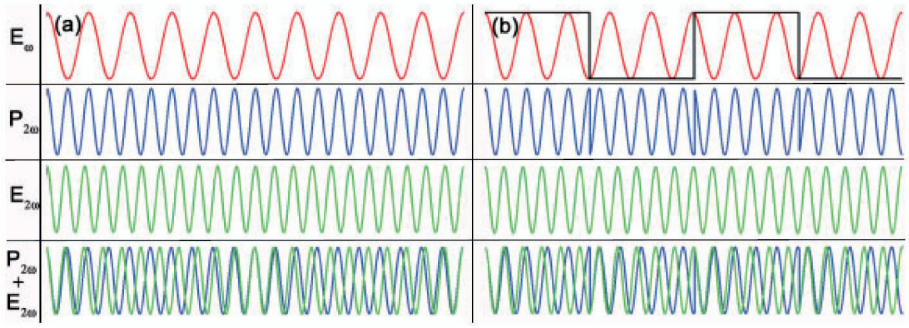

FIGURE 1.1: Electric field at ω, induced polarization at 2ω, electric field at 2ω and combined polarization and second harmonic field: (a) Homogeneous crystal. In general, as a result of dispersion, the induced polarization gets out of phase with respect to the electric field generated at the beginning of the crystal. (b) Periodic reversal of the material nonlinear coefficient allows to brings back the polarization in phase with the second harmonic wave from Ref [40].

will be out of phase with each other, thus eventually leading to destructive interference. The distance over which the relative phase of two waves changes by π is the "coherence length" $l_c = \lambda/4(n(2\omega)-n(\omega))$ or $l_c = \pi/\Delta k$ (where $\Delta k = k(2\omega)-2k(\omega)$ is the phase mismatch) which corresponds to the half period of one cycle comprising constructive and then destructive interference as displayed in Fig. 1.2c for the case of non phase-matching. This mismatch needs to be compensated via an appropriate phase-matching procedure.

For a nonlinear crystal of length L, the SH field $E_{2\omega}(L)$ at the end of this sample is given by [39, 41]:

$$E_{2\omega}(L) = i\frac{\omega}{n_{2\omega}c}E_{\omega}^{2}\int_{0}^{L} d(z)exp(-i\Delta kz)\mathrm{d}z \tag{1.1}$$

where E_ω is the fundamental field and $d(z)$ is the nonlinear coupling coefficient. For perfect conventional phase matching with $d(z) = d_{\text{eff}}$, where d_{eff} is the effective value of the nonlinear coupling coefficient (comprising the relevant combination of cartesian tensor coefficients weighed by adequate trigonometric factor accounting for the specific combination of polarization states for the interacting harmonic and fundamental beam) and $\Delta k = 0$, the intensity of the SH wave $I_{2\omega}$ is then given by:

$$I_{2\omega} = \frac{2\omega^2 d_{\text{eff}}^2}{n_{2\omega}n_{\omega}^2c^3\epsilon_0}I_{\omega}^2L^2 \tag{1.2}$$

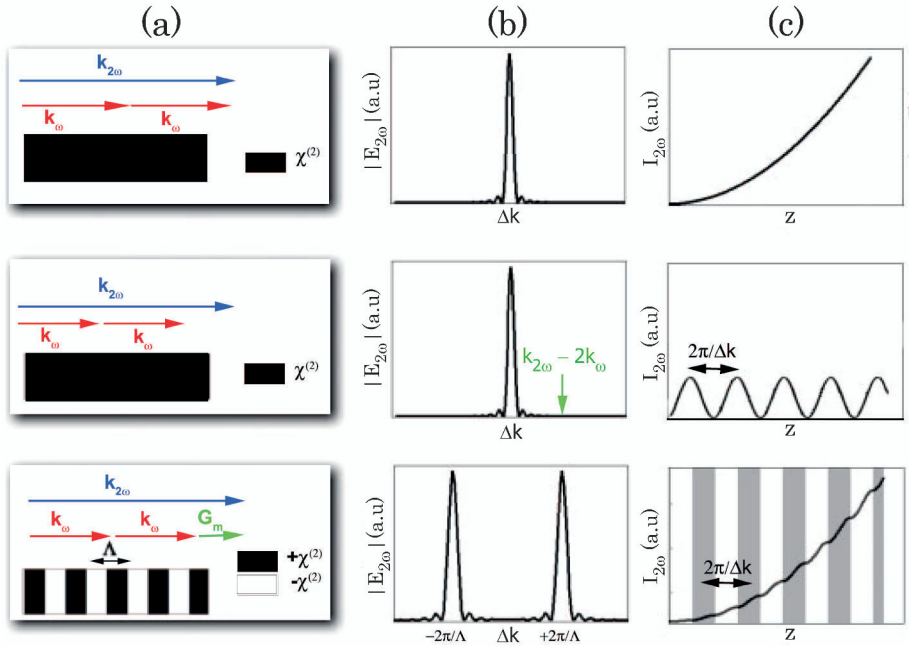

Figure 1.2: Phased matched, non-phase matched and quasi-phase matched cases. (a) Nonlinearity along the crystal and k-vector scheme, (b) absolute value of the second harmonic field with respect to the spatial frequency and (c) evolution of the SH intensity along the crystal from Ref [40].

where I_ω is the intensity of the fundamental wave.

In this case, the intensity of the SH wave is quadratically dependent on the length of the nonlinear crystal as shown in the upper part of Fig. 1.2c. As already mentioned, the most widely used method to satisfy this condition is to to use the birefringence of the crystal to compensate its dispersion [7–9]. However, there are some drawbacks to this method, such as the eventual impossibility for a given material and wavelength to ensure compensation of the frequency dispersion, and the need to use a non-diagonal coefficient of the nonlinear tensor to involve birefringence, thus precluding the otherwise preferable use of the larger diagonal coefficient.

More recently, a second method known as quasi-phase matching (QPM), has been widely used in order to overcome the phase-matching problem, in which the second order susceptibility $\chi^{(2)}$ of nonlinear materials is spatially modulated by periodically poling the material by an electric field [10, 11], as in the lower part of Fig. 1.2a. In this case, the phase mismatch is balanced by the modulation of the

nonlinear coefficient (appearing in the z dependence of the $d(z)$ local nonlinearity) as in Fig. 1.1b. Such a patterned structure is called a QPM crystal with period length of $\Lambda = 2\pi m/\Delta k$ (where m is an integer that can take an odd value). The second harmonic intensity in this case is given by:

$$I_{2\omega} \approx \frac{2\omega^2 d_{\text{eff}}^2 |G_m|^2}{n_{2\omega} n_\omega^2 c^3 \epsilon_0} I_\omega^2 L^2 \tag{1.3}$$

In this case, the intensity of the quasi-phase matched wave is smaller than that for perfect phase-matching by a factor $|G_m|^2$ (where $|G_m|$ is the Fourier coefficient of the periodical modulation of the nonlinear coefficient). Fejer et al. [39] have estimated the maximum fluctuation allowed for the period of a QPM structure to be $\delta\Lambda = 1.77\Lambda/Nm$ where N is the number of alternating domains.

Following the maturation of the electric field poling method [11, 40, 42], one- or two-dimensional QPM crystals have been fabricated with a wealth of application in frequency mixing, including commercial ones.

1.2 Nonlinear Optical Microscopy and Nano-probes

1.2.1 Nonlinear Optical Microscopy

In 1977, Sheppard et al. first suggested and then demonstrated how a nonlinear optical phenomenon could be incorporated into a high-resolution, three-dimensional scanning laser microscope [43–45]. Nonlinear optical microscopy has been developed since then in connection to different nonlinear optical phenomena, such as two-photon excited fluorescence (TPEF), second-harmonic generation (SHG) and third-harmonic generation (THG) as shown in Fig. 1.3.

The development of femtosecond lasers, the improved spatial resolution allowed by the confocal microscopy and the availability and ever improving performances of

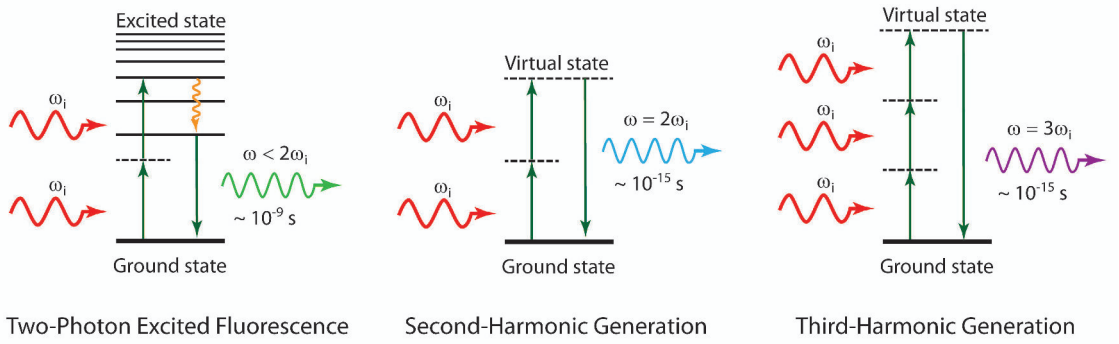

Figure 1.3: Two-photon excited fluorescence, second-harmonic generation and third-harmonic generation process in the energy-level diagram.

high sensitivity detectors such as avalanche photodiodes, have jointly provided optimal conditions for the current development of nonlinear optical microscopy. Nowadays, many variants of the well known nonlinear optical microscope are available towards different purposes, but they all derive from the template configuration shown in Fig. 1.4.

By using a light beam with very high peak intensity so as to nonlinearly excite different types of objects, TPEF, SHG or THG microscopes all need a pulsed laser source to supply the necessary optical power. In order to tune the wavelength of the fundamental beam to a given resonance or to fulfill the required phase-matching condition, different laser sources or a tunable Optical Parametric Oscillator (OPO) can be used as in Fig. 1.4. A dichroic mirror reflects the infrared fundamental light and transmits the TPEF, SHG (or THG) emitted from the sample at the focal point of the microscope objective. The emission can be directly detected by a photodiode or decomposed into x and y polarization components which can be separately detected by two avalanche photodiodes and then imaged by way of a $\{xy\}$ (2D) or $\{xyz\}$ (3D) position scanner using a piezo stage. Alternatively, the intensity of the nonlinear response at a given position in the sample can be recorded and plotted with respect to the angle of the fundamental linear polarization state which can be varied by a half-wave plate.

In the wake of the pioneering demonstration by Denk et al. [47] which helped

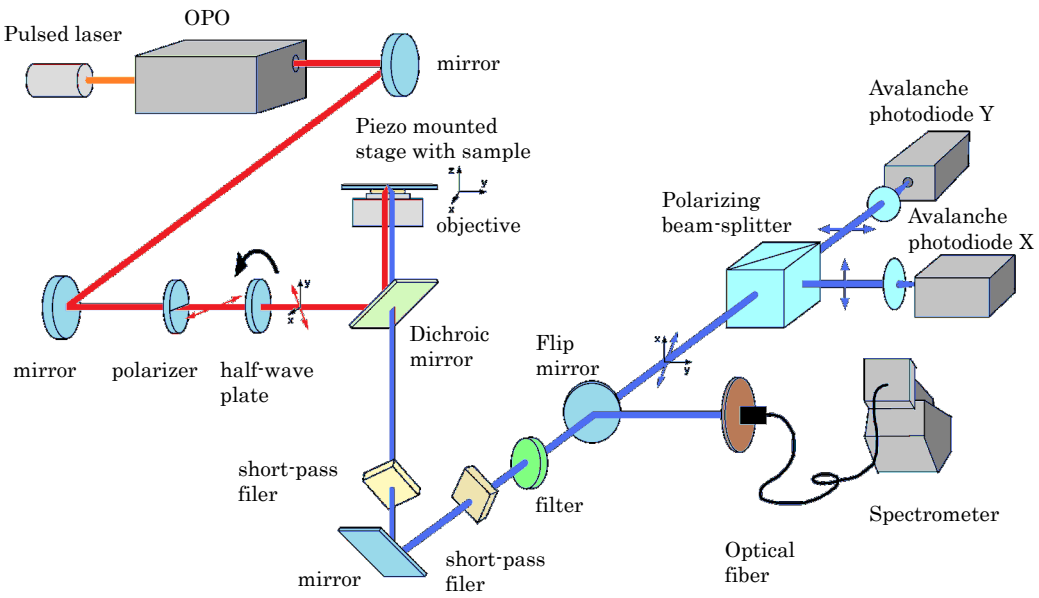

FIGURE 1.4: General scheme for the configuration of the TPEF or SHG microscopy.

convince the biological community of the relevance of nonlinear microscopy towards the imaging of living cells, tissues, embryos, and organisms, the field of nonlinear microscopy has considerably grown to encompass biological imaging, much of which still to be developed. Being both based on nonlinear optical process, SHG and TPEF microscopies share many common features, such as common dependence of outgoing light on the square of the excitation intensity, thereby offering optical sectioning without the need for a confocal aperture because of the restriction of efficient excitation in a small diffraction limited volume around the focal point.

However, unlike TPEF microscopy where the fluorescent dye used as the molecular probes can saturate, bleach, and/or generate photo-toxic by products, SHG is a coherent process involving only virtual energy transitions with none of the negative consequences of a finite excited state lifetime. Indeed, SHG probes neither bleach nor saturate even after several hours of illumination [46]. Consequently, SHG microscopy is being increasingly applied in biology.

1.2.2 Second-harmonic generation Nanoprobes*

In order to image a biological object by SHG microscopy, nonlinear materials used as the imaging probe must be used. NLO signals are strongly sensitive to size, shape, and orientation of nonlinear nano-emitter whereas the high sensitivity of SHG microscopy makes single-particle or even single-molecule detection possible. Following the advent and development of nanotechnologies, nano-scale nonlinear materials that lack an inversion center (also referred to as non-centrosymmetric materials) where developed for use as SHG nanoprobes and successfully demonstrated in various contexts.

Several SHG nanoprobes, down-scaled from otherwise well-known benchmarking inorganic materials with large second-order susceptibility $\chi^{(2)}$ have been reported, among which Barium Titanate ($BaTiO_3$) [46, 49, 50], Lead Titanate $PbTiO_3$ [50], Zinc Oxide (ZnO) [51, 52], $Fe(IO_3)_3$ [53, 54], $KTiOPO_4$ [55–58], $Sr_{0.6}Ba_{0.4}Nb_2O_6$ [59], or $KNbO_3$ [60]. Besides these traditional oxide based nonlinear optical materials, the SHG properties of some inorganic quantum dots or quantum dots with core/shell or dot-on-rod structure have been investigated such as single core/shell CdTe/CdS nano-crystals with a diameter of 10 to 15 nm [61], single CdTe/CdS core/shell rod-on-dot nanocrystals with different geometrical parameters [62], Gallium Arsenide GaAs [63] and Zinc Selenide ZnSe [64]. By using semiconductor quantum dots as probes, the imaging process can be performed by a combination of SHG microscopy with fluorescence confocal microscopy. In order to enhance the second-order susceptibility of nano-particles vie dipole-dipole interactions and resonance on local plasmons, hybrid systems combining a quantum dot with a metallic nanoparticle have also been reported [65].

Contrasting the propagation of SHG wave in bulk crystals, SHG nanoprobes scatter the signal in many directions. Due to the negligible dimension of SHG nanoprobes with respect to the wavelength of the fundamental optical wave allowing

*This section is based on: [48]

to consider it as point-wise, the phase-matching condition does not apply.

SHG nanoprobes also bear the possibility to perform multi-labelling experiments by using SHG nanoprobes with different materials and using the resonance-enhancement of SHG process when the energy of the generated harmonic photon matches that of the ground to first excited state transition.

1.3 Motivation and Outline of Thesis

Although improvements and higher efficiencies are reported almost day after day in SHG microscopy, some of its inherent drawbacks have also become more obvious in the course of this development. In particular, the requirement of a bulky and sometimes cumbersome laser source with a very high intensity or the possibility to photo-damage sensitive samples are limiting the field. Another basis limitation of SHG microscopy originates from the broadly used intensity detection method whereby photo-detectors are used to collect the intensity of the generated harmonic beam, thus hiding no less important information contained in the electric field and its phase.

Besides second-harmonic generation, another important effect associated to the second-order susceptibility $\chi^{(2)}$ is the Pockels effect, which expresses the variation of the refractive index of nonlinear materials under the application of an externally applied voltage. The conception of a new handmade nonlinear microscope fully based now on the Pockels linear electro-optical effect, so-far unexploited for imaging purpose, was put forward and further implemented during two previous doctoral thesis [66, 67]. This newly developed and unique nonlinear microscope, which came to be named PLEOM (for Pockesls Linear Electro-Optical Microscopy) allows to map the second-order susceptibility of non-centrosymmetric materials and structures, very much like a SHG microscope however in the present case with a very high sensitivity [1] and the use of a simple low power stable CW laser source. It provides a new tool to investigate the whole range of objects which can be studied by SHG microscopy, however providing crucial complementary information, such as relate to

the phase of the harmonic beam, which are not readily available form SHG.

Among the most interesting candidates for our new microscopy are the SHG nano-probes for applications in imaging and tracking. Due to their spontaneous dielectric polarization which precludes a center of symmetry, single domain ferroelectric crystals account for almost known SHG nano-probes. The orientation of these SHG nano-probes can be either random or pre-orientated by the application of an electric field or any other means of orientation. Consequently, a prerequisite towards further quantitative imaging use of such nano-probes in our Pockels microscope is the ful determination of their orientation.

Besides, quasi-phase matched nonlinear crystals are very attractive for use as frequency doubling devices in laser systems due to the spatial modulation of their second-order susceptibility which solves the phase matching condition. Since the first fabrication via an electric field poling method and subsequent demonstration of a QPM-$LiNbO_3$ crystal in [11], a large number of reports on the application of QPM crystals have been published in which the conversion efficiency of second-order nonlinear processes of interest where shown to strongly depend on the parameters of the periodic or aperiodic structure. This situation has motivated the demand for quantitative imaging and characterization of QPM patterns, in order to test the applicability of the crystals towards frequency doubling as well as improve the electric field poling process for different classes of materials as well as QPM patterns. Several methods based on the properties of ferroelectric domains have been reported in order to fulfill this demand and visualize the domain structures, such as the Čerenkov SHG imaging technique [68–71]. However, while this method provides a highly accurate visualization of domain frontiers, it fails to provide information onto the inside of the domains, or provide high resolution mapping.

Thus the **objective** of this dissertation is therefore to develop a full theoretical analysis for SHG nano-probes (or single ferroelectric domains at the nano-scale) investigated by PLEOM in which the accuracy of our theory has been confirmed by our experimental results. Alongside this purpose, we have extended the applicability of PLEOM to encompass the investigation and characterization of ferroelectric

materials with multi-domain structures, such as tailored one- and two-dimensional periodic and aperiodic ferroelectric domain structures of QPM crystals, allowing us to determine the periodicity parameters, evidence otherwise non-visible local defects, etc...

The thesis is organized as follows:

- In **Chapter 1**, we provide a brief introduction to quasi-phase matched crystals, nonlinear microscopy and nonlinear nano-probes will be the main objects of our investigations.

- In **Chapter 2**, I present a thorough introduction to PLEOM electrooptic microscopy, including its configuration, working principle, optical and electronic elements as well as the data processing chain. An alternative configuration for PLEOM is also presented in this chapter.

- In **Chapter 3**, I develop a complete theory of the Pockels scattering response from single ferroelectric $KTiOPO_4$ nano-crystals detected by PLEOM. The excellent agreement between the experimental results and the theory provides confirmation of there relevance of our model. Among the outcome, we show, for the first time to our knowledge that the orientation, and especially the vectorial features of the electric polar moment of a single random SHG nano-probe, can be inferred from PLEOM with great accuracy.

- In **Chapter 4**, we present a new, non-invasive method towards the characterization of the ferroelectric domain structure in 1D periodically poled $KTiOPO_4$ crystals (quasi-phase matched crystals) by PLEOM, including both the theoretical model and experiment in mutual agreement. The inversion of ferroelectric domains is visualized by a π phase shift, whereas the domain walls are clearly outlined by the cancellation of the signal amplitude.

- In **Chapter 5**, we extend the validity of PLEOM to map 1D quasi-phase matched crystals into 2D quasi-crystalline patterns. The domain structure of a 2D decagonal quasi-periodic $LiNbO_3$ nonlinear crystal was characterized by

PLEOM. This study confirms the ability of PLEOM to image and characterize the domain properties of any ferroelectric material with 1 or 2D periodic or aperiodic patterning of its nonlinear optical structures, opening the way to the imaging and detailed characterization of more complex electrooptic systems with tailored domain structures.

- In the **last chapter**, we summarize the results obtained during this study and discuss in conclusion the perspectives opened-up by this work.

- The **Appendix** part is gathering more detailed accounts of both experimental and theoretical issues addressed in this study. Besides, some incomplete parts of this study with different and possibly interesting results are outlined, such as pertaining to the investigation of biological membranes by PLEOM.

2

Pockels Linear Electro-Optical Microscopy

Recently, the development of nonlinear second harmonic generation microscopy (SHGM) has generated a variety of nano-scale probe instruments to study single nano objects such as quantum dots, non-centrosymmetric nano-crystals, and biological entities, etc... Although the high efficiency and improvements of SHGM have been shown day after day from thousands scientific articles, this domain still suffers from some limitations when used to study some special objects such as biological samples. The main disadvantage of SHGM stems from the laser source. By using frequency doubling in nonlinear materials, SHGM requires the use of a pulsed laser source with high power in the infrared region. And sometimes, one needs to use different laser sources or an optical parametric oscillator (OPO) to tune the wavelength of the fundamental beam. For that reason, the laser sources are expensive and bulky, not easy to operate, and dangerous for the alignment and manipulation

with invisible light. Moreover, sensitive samples such as living biological samples can be destroyed under illumination by a high intensity laser beam.

Besides second harmonic generation, another effect associated to the the second-order susceptibility $\chi^{(2)}$ is named the Pockels effect. The Pockels effect or the linear electrooptic effect is the linear variation of the refractive index of a nonlinear optical medium upon application of an external applied electric field first described by F. Pockels in 1893 [41, 72] which originates from the generic second-order susceptibility tensor $\chi^{(2)}$ attached to quadratically nonlinear materials. When a nonlinear material is exposed to an external electric field, the change of refractive index of this object can be read-out by the experienced phase shift by a light which propagates through it. By using a Mach-Zehnder interferometer to measure this phase shift, informations on the second-order susceptibility $\chi^{(2)}$ of nonlinear materials can be estimated. Following these ideas, the Pockels Linear Electro-Optical Microscope (PLEOM) based on the Pockels effect was conceived and built [66, 67]. It combines a confocal microscopy allowing to study nano-scale objects, a Mach-Zenhder interferometer, and a homodyne detection system. In this chapter, we will introduce the main features of PLEOM including its configuration and operating mode.

2.1 Confocal Microscopy*

The basic concept of confocal microscopy was developed by Marvin Minsky in the middle of 1950s (patented in 1961) [73] as shown in Fig. 2.1 when he was a postdoctoral student at Harvard University. He wanted to image the neural networks of brain tissue without staining and biological events occuring in living samples. It derives from light microscopy in which the illuminating and collecting light are focused on the same diffraction-limited spot in studied samples. Unlike conventional light microscopy which images the entire field of view of the objective lens onto the detector, confocal microscopy images only one spot. To obtain a complete image,

*This section is based on: [73–76]

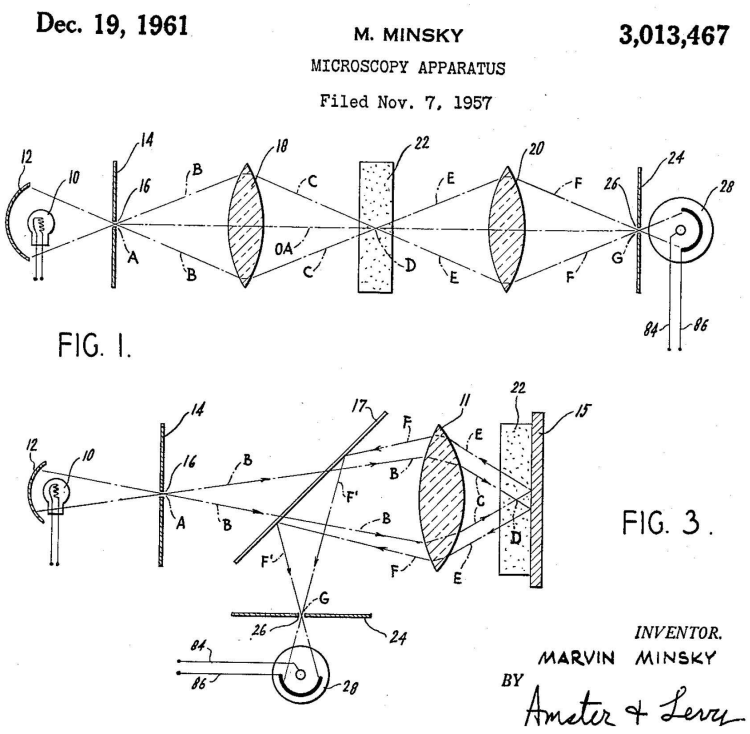

FIGURE 2.1: Confocal microscope design of Minsky in U.S.Parent 3013467 [73].

the spot is moved over the specimen and the image is built point by point. The most important aspect of confocal microscopy is that parts of the specimen not at the focal point contribute very little to the spot image. Thus confocal microscopy allows to perform very high-resolution and three dimentional (3D) measurements even within thick specimens.

Following the prioneering work by Minsky, confocal microscopy has been effectively improved with the advances in computer and laser technology leading to the laser scanning confocal microscope. After Minsky's patent had expired, practical laser scanning confocal microscopy was developed and the first commercial instrument appeared in 1987. During the 1990s, advances in optics and electronics allowed to improve the confocal microscopy system based on more stable and powerful lasers, high efficiency scanning mirror units, high throughput fiber optics, better thin film dielectric coatings, and detectors with reduced noise characteristics. Modern confocal microscopes are completely integrated optic-electronics systems where the optical

microscope plays as a central role in a complex configuration that includes one or more electronic detector, a computer (which controls all electronic devices of the system, collects and analyzes the signal data), and several laser systems with selected wavelengths.

The principle of laser scanning confocal fluorescence microscope is schematically presented in Fig. 2.2. The coherent light emitted from a laser source passes through

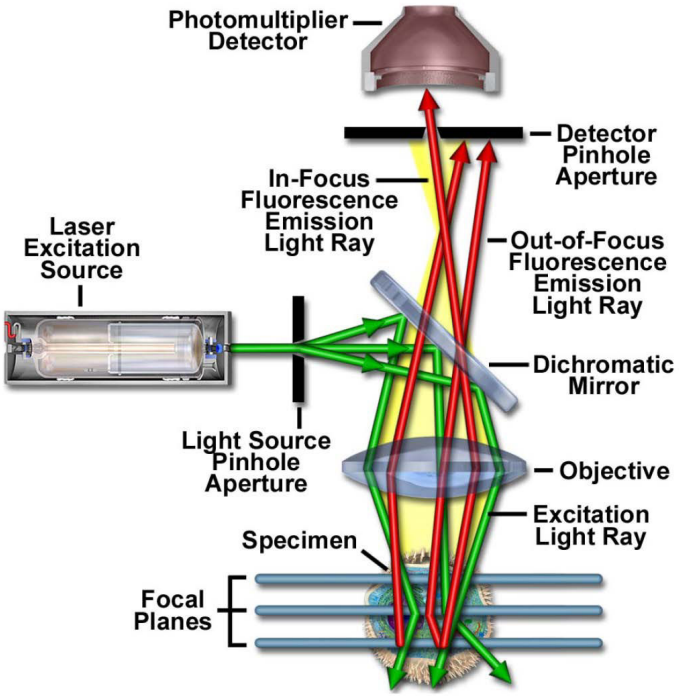

Figure 2.2: Schematic diagram of the optical pathway and principal components in a laser scanning confocal microscopy [76].

a pinhole aperture which is located in a conjugate plane respect to a scanning point on the specimen and a second pinhole aperture positioned in front of the detector. The laser is reflected by a dichromatic mirror and focused onto a point of the specimen by a microscopy objective. The fluorescence emitted from the focused spot on the specimen passes back through the dichromatic mirror and is focused at the confocal point where the second pinhole is set. The fluorescence is then projected into the detector. One of the most important components of the scanning

resolution is the pinhole aperture, which acts as a spatial filter. It serves to exclude fluorescence signals from out-of-focus points which are above or below the focal plane. The pinhole aperture also serves to eliminate stray light passing through the optical system. A 2D or 3D scanning can be accomplished by translating the sample stage along the x, y, and z directions, while the laser illumination spot being held at a fixed position.

The resolution of this microscope depends on the size of the diffraction-limited spot. Thus by using an appropriate objective, the diameter of the diffraction-limited spot is:

$$d = \frac{1.22\lambda}{2 \times (n \sin\theta)} = \frac{1.22\lambda}{2 \times \mathrm{NA}} \tag{2.1}$$

where λ is the wavelength of the laser source and $n \sin\theta$ or NA is called the numerical aperture of the microscopy objective. The size of the illumination point ranges from approximately 0.25 to 0.8 micrometers in diameter and 0.5 to 1.5 micrometers deep at the brightest intensity (focusing spot).

Confocal microscopy provides a non-invasive method to examine both living and fixed specimens under a variety of conditions with enhanced clarity.

2.2 Mach-Zehnder interferometer

The Mach-Zender interferometer is a simple device which is used to determine the relative phase shift variation between two collimated beams derived by splitting the light from a single source. This interferometer is named after the proposal of Zehnder in an 1891 article and the refinement of the physicists Ludwig Mach in a 1892 article [77].

In contrast to the well-known Michelson interferometer, in the Mach-Zehnder interferometer, two separated light paths are traversed only once. Fig. 2.3 is the schematic of the normal Mach-Zehnder interferometer. Its working principle is very simple [78, 79]. A collimated beam emitted from a light source is split into two parts by a beam splitter or half-silvered mirror. The two resulting beams are named “the

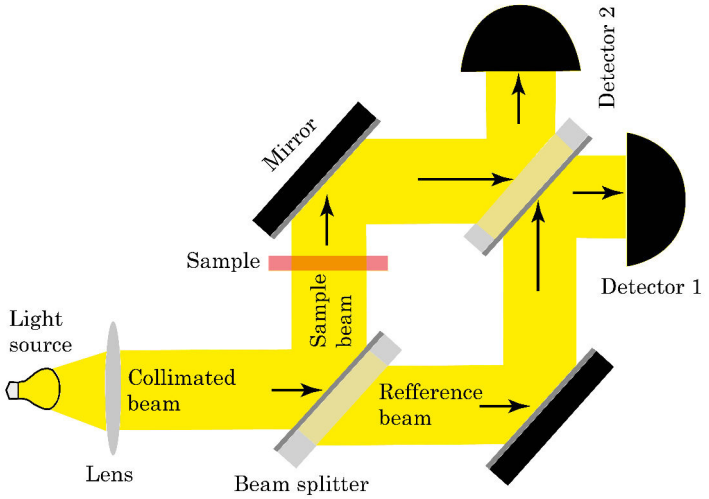

Figure 2.3: Schematic of a Mach-Zehnder interferometer.

reference beam (RB)" and "the sample beam (SB)". After reflected by the mirrors, they are recombined together by the second beam splitter (50:50) and enter two optical detectors. Depending on the relative phase acquired by two beams when travelling along their optical paths, the second beam splitter will reflect the beam with an efficiency between 0 and 100%.

Calling the intensities of the sample and reference beams I_1 and I_2 respectively, the phase shift between these upon propagation from the light source to detector 1 is $\Delta\varphi$, and $\pi+\Delta\varphi$ to detector 2. So the intensities of the light entering the detectors 1 and 2 respectively are:

$$I_{dectector1} = \frac{1}{2}[I_1 + I_2 + 2\sqrt{I_1 I_2}\cos(\Delta\varphi)] \tag{2.2}$$

$$I_{dectector2} = \frac{1}{2}[I_1 + I_2 - 2\sqrt{I_1 I_2}\cos(\Delta\varphi)] \tag{2.3}$$

If the first beam splitter is exactly balanced (50:50), $I_1 = I_2 = \frac{1}{2}I$ (I is the intensity of the light source) and now, the intensities of the light which enter the detector 1 and 2 respectively are:

$$I_{dectector1} = \frac{1}{2}I[1 + \cos(\Delta\varphi)] \tag{2.4}$$

$$I_{dectector2} = \frac{1}{2}I[1 - \cos(\Delta\varphi)] \tag{2.5}$$

Depending on the relative phase acquired by the two beams when travelling along their optical paths $\Delta\varphi$, the second beam splitter will reflect the beam with an efficiency at each of the two detectors ranging from 0 to 100% so that the total intensities of light at the two detectors are constant and equal to the intensity emitted initially by the light source.

If the phase shift between two beams on their ways to the detector 1 ($\Delta\varphi$) is 2π, the intensities of light enter the detector 1 and 2 are $I_{detector1} = I$ and $I_{detector2} = 0$. It means that there is a totally constructive interference on the path to the detector 1 and a totally destructive interference on the path to detector 2.

If the first beam splitter is not well balanced, only partial constructive and destructive interference are occurring. This property is used in some special cases in interferometry [79].

The Mach-Zehnder interferometer offers a relatively large and accessible working space, so that it is frequently used to measure pressure, density, and variation of the temperature in gases [79]. In smaller size various, they are applied to electrooptic modulation towards signal processing or in various applications in optics and optical communication [72]. Fig. 2.4a shows a simple optical modulator using a Mach-

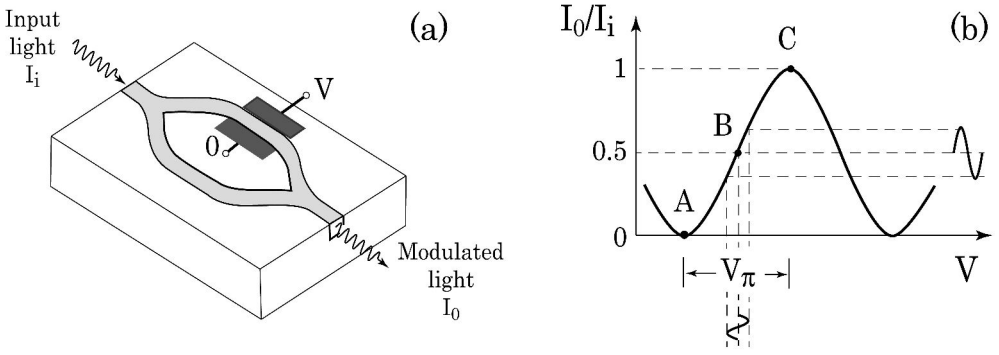

FIGURE 2.4: An optical modulator using Mach-Zehnder interferometer [72].

Zehnder interferometer [72]. An electric field (voltage V) is used to modulate the phase of the light in an arm by the linear electrooptic effect (the Pockels effect which will be described in detail in section 2.4). If the tension V is switched between points

A and C (Fig. 2.4b), the device serves as an optical switch. Towards linear intensity modulation, one needs to apply a sinusoidal voltage V varying at the modulated frequency around the inflexion point B as in Fig. 2.4b.

The Mach-Zehder interferometer is also used to study "quantum entanglement" in quantum mechanics [80, 81].

2.3 Balanced homodyne detection

Balanced homodyne detection is normally used in optical interferometry to detect the phase of electromagnetic waves. It derives from homodyne detection one by using two photodiodes instead of a single one after a beam splitter with a precisely balanced 50:50 ratio. Homodyne detection being a variant of heterodyne detection, I will first recall the working principle of heterodyne detection.

Heterodyne detection is a radio signal processing technique that was invented in 1901 by a Canadian inventor named Reginald Fressenden. There, a weak input signal is mixed with one strong wave generated from a local oscillator in a nonlinear signal-processing device such as rectifier. After the mixing process, the output signal includes two new signals at different frequencies, respectively at the sum and difference frequency of the signal and local oscillator. Typically only one of the new frequencies of the signal is desired while the other is filtered out.

Optical heterodyne detection is an extension of the heterodyning technique applied to higher frequency electro-magnetic waves, in our case visible light. The nonlinear signal-processing devices are photodetectors which are square-law detectors (the photodetector current is proportional to the square of the total electric field amplitude of the electro-magnetic waves), such as the photodiodes in Fig. 2.5.

If the weak signal is: $E_s \cos(\omega_s t + \varphi)$ and the reference beam (local-oscillator beam) is: $E_r \cos(\omega_r t)$, the photodetector current is given by:

$$I \sim [E_s \cos(\omega_s t + \varphi) + E_r \cos(\omega_r t)]^2 \tag{2.6}$$

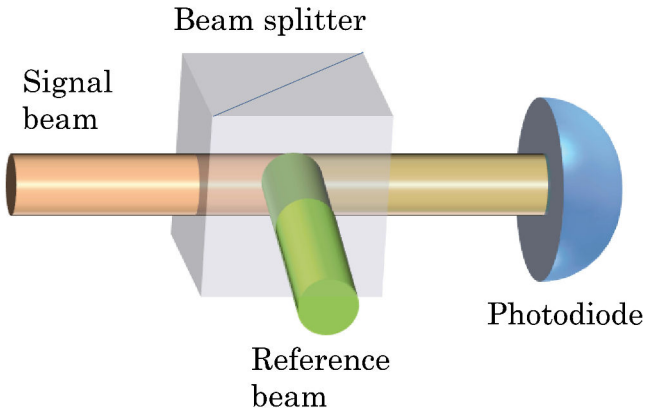

FIGURE 2.5: Setup for an optical heterodyne detection.

$$I \sim \frac{1}{2}E_s^2\left[1+\cos 2\left(\omega_s t+\varphi\right)\right]+\frac{1}{2}E_r^2\left[1+\cos 2\left(\omega_r t\right)\right] + E_s E_r\left\{\cos\left[\left(\omega_s-\omega_r\right)t+\varphi\right]+\cos\left[\left(\omega_s+\omega_r\right)t+\varphi\right]\right\} \quad (2.7)$$

From the expression 2.7 we see that the spectrum of photocurrent exhibits three different frequency domains:

- a constant (zero-frequency) part which is proportional to the sum of signal and local oscillator power.
- a low frequency component at $(\omega_s - \omega_r)$.
- a high frequency component at $(\omega_s + \omega_r)$, $2\omega_s$ and $2\omega_r$.

The low frequency part can be isolated by electronic filtering and further processed by adequate electronic, thus the electronic signal is then:

$$I \sim E_s E_r \cos\left[\left(\omega_s-\omega_r\right)t+\varphi\right] \quad (2.8)$$

Its electric power is proportional to the product of the electric field amplitudes of the signal and local oscillator. Due to mixing with a strong oscillator, the heterodyne signal resulting from a weak input can be made much more powerful than the directly detected signal. In this case, heterodyne detection provides a signal gain although there is no optical amplification involved.

Homodyne detection is a variant of heterodyne detection, where the frequency of the local oscillator is the same as the frequency of the signal. In optical homodyne measurements, both waves are derived from the same laser source after division through a beam splitter or a half-silvered mirror. In this case $\omega_s = \omega_r$ and replacing into the expression 2.7 we leads to the following expression for the photodetector current:

$$I \sim \frac{1}{2}E_s^2\left[1+\cos 2\left(\omega_s t+\varphi\right)\right]+E_sE_r\left[\cos\varphi+\cos\left(2\omega_s t+\varphi\right)\right]+\frac{1}{2}E_r^2\left[1+\cos 2\left(\omega_s t\right)\right] \tag{2.9}$$

The photodetector current has two components, namely a constant part (at zero frequency) and a high frequency parts oscillating at $2\omega_s$. The high frequency part is cut by a low pass electronic filter and only the constant part is detected:

$$I \sim \frac{1}{2}\left(E_s^2+E_r^2\right)+E_sE_r\cos\varphi \tag{2.10}$$

In the expression 2.10 we see that the intensity of the homodyne signal depends on the relative phase of the signal and reference waves. So that homodyne detection can be used to detect a phase shift between two coherent light beams derived from the same source but having passed through different ways before recombination.

The remaining problem of heterodyne as well as homodyne detection is that excess noise from the reference wave (the local oscillator wave) directly affects the output electronic signal due to the weakness of the input signal wave. In order to estimate the effect of such noise, a useful modification of the homodyne detection is the balanced homodyne detection which makes use of two detectors as in Fig. 2.6.

In this case, the input signal wave and the reference wave recombine together at a beam splitter with a precisely balanced 50:50 ratio. The mix wave is divided into two parts and each part is detected by a detector (photodiode). The sum or the difference of two photodectector currents is obtained by a simple electronic circuit. If the input signal is blocked, the difference of photocurrents exhibits the shot noise level of the reference wave. The optical balanced homodyne detection is perfectly compatible with the detection system of a Mach-Zehnder interferometer because of

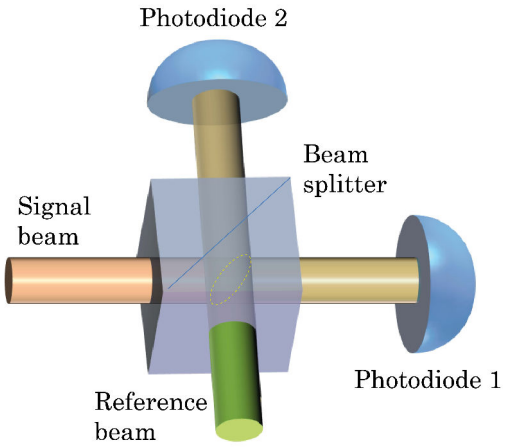

FIGURE 2.6: Setup for an optical balanced homodyne or heterodyne detection.

the same experimental configuration. In this case, the difference of photodectetor currents as in expressions. 2.4 and 2.5 contains the value of the phase shift $\Delta\varphi$. By using a optical balanced homodyne detection onto a Mach-Zehnder interferometer, a small phase shift $\Delta\varphi$ can be accurately detected. From that principle, the optical balanced homodyne detection is used for various optical applications in which the detected signal is very weak and can be considered as a perturbation.

2.4 Linear electro-optical effect (Pockels effect)

In general, optical media exhibit changes in their optical properties when subjected to an external electric field. This is due to electric forces that distort the positions, orientations, or shapes of the molecules constituting the material.

The Pockels effect or Pockels linear electrooptic effect was firstly studied by Friedrich Carl Alwin Pockels in 1893 [72] long before the advent of lakes and NLO, although it belongs to the clan of quadratic nonlinear effect. It expresses the variation of the refractive index of a nonlinear optical medium deprived of inversion symmetry such as $LiNbO_3$, KTP, KDP, KD*P... under the application of an external DC or low frequency AC electric field.

2.4.1 Refractive index of an optically isotropic medium

The refractive index is a dimensionless value that accounts for the lower light velocity in materials as compared to vacuum due to light-matter interactions. It is defined as:

$$n = \frac{c}{v} \tag{2.11}$$

where c is the speed of light in vacuum and v is the speed of light (electromagnetic wave) in that medium. The speed of light in the vacuum is given by: $c = 1/\sqrt{\epsilon_0 \mu_0}$ with ϵ_0 and μ_0 are the permittivity and permeability of free space respectively. The speed of light in a medium is smaller than the speed of light in the vacuum because of the interactions between the electric and magnetic fields with the molecules constituting that media and defined as: $v = 1/\sqrt{\epsilon\mu}$ with ϵ and μ are the permittivity and permeability of that medium respectively.

Normally, with an optical medium, the interaction between the magnetic fields with this medium can be neglected so that we can safely assume that $\mu \approx \mu_0$. The refractive index of this medium then only depends on the interaction between the electric field component of light and the electrons of the material which leads to:

$$n = \sqrt{\frac{\epsilon}{\epsilon_0}} = \sqrt{\epsilon_r} \tag{2.12}$$

where ϵ_r is the relative permittivity.

When light travels in the vacuum, the electric displacement $\overrightarrow{D}$ simply relates to the electric field component $\overrightarrow{E}$ of the light by the expression:

$$\overrightarrow{D} = \epsilon_0 \overrightarrow{E} \tag{2.13}$$

But when the light travels in an optical medium, the electric displacement $\overrightarrow{D}$ induced inside this media becomes:

$$\overrightarrow{D} = \epsilon_0 \overrightarrow{E} + \overrightarrow{P} \tag{2.14}$$

where $\overrightarrow{P}$ is the dielectric polarization density which is induced by the interaction between the electric field component of light and the molecules constituting the medium.

In an optically isotropic medium, the dielectric polarization density vector is proportional to the electric field vector as below:

$$\overrightarrow{P} = \epsilon_0 \chi \overrightarrow{E} \tag{2.15}$$

where χ, the susceptibility of this medium, is a scalar in the case of an isotropic medium.

Replacing the $\overrightarrow{P}$ from expression 2.15 into 2.14 leads to:

$$\overrightarrow{D} = \epsilon_0 (1 + \chi) \overrightarrow{E} = \epsilon \overrightarrow{E} \tag{2.16}$$

Comparing expressions 2.12 and 2.16 leads to the following relation between the refractive index and the susceptibility of the material:

$$n^2 = 1 + \chi \tag{2.17}$$

The value of the susceptibility χ of an optical media varies with the frequency of the electromagnetic wave, so that the refractive index of this medium depends also on the angular frequency (ω) of the light:

$$n^2(\omega) = 1 + \chi(\omega) \tag{2.18}$$

2.4.2 Refractive index of an optically anisotropic medium

In an optically anisotropic medium, the dielectric polarization density $\overrightarrow{P}$ is not simply proportional to the electric field $\overrightarrow{E}$, as the susceptibility of such a medium can not be a scalar. The relation between the dielectric polarization density and the electric field becomes tensorial [41]:

$$P_i = \sum_j \chi_{ij} E_j \tag{2.19}$$

or explicitly in Cartesian coordinates and matrix form:

$$\begin{bmatrix} P_x \\ P_y \\ P_z \end{bmatrix} = \epsilon_0 \begin{bmatrix} \chi_{xx} & \chi_{xy} & \chi_{xz} \\ \chi_{yx} & \chi_{yy} & \chi_{yz} \\ \chi_{zx} & \chi_{zy} & \chi_{zz} \end{bmatrix} \begin{bmatrix} E_x \\ E_y \\ E_z \end{bmatrix} \tag{2.20}$$

In a non-optically active medium, the susceptibility tensor χ_{ij} is represented by a real symmetric matrix. So that there are only six independent elements: χ_{xx}, χ_{yy}, χ_{zz}, $\chi_{xy} = \chi_{yx}$, $\chi_{xz} = \chi_{zx}$, and $\chi_{yz} = \chi_{zy}$. By using an orthogonal transformation, it is possible to transform a symmetric matrix into diagonal form, resulting in a simpler susceptibility tensor in the new coordinate system $(OXYZ)$ [41, 72, 82]. Expression 2.20 now becomes:

$$\begin{bmatrix} P_X \\ P_Y \\ P_Z \end{bmatrix} = \epsilon_0 \begin{bmatrix} \chi_{XX} & 0 & 0 \\ 0 & \chi_{YY} & 0 \\ 0 & 0 & \chi_{ZZ} \end{bmatrix} \begin{bmatrix} E_X \\ E_Y \\ E_Z \end{bmatrix} \tag{2.21}$$

The new coordinate system is known as the principal dielectric axis frame, and in this coordinate system, the dielectric tensor reduces to diagonal form.

Replacing the dielectric polarization density from expression 2.21 into 2.14 we have:

$$\begin{aligned} \begin{bmatrix} D_X \\ D_Y \\ D_Z \end{bmatrix} &= \epsilon_0 \begin{bmatrix} 1+\chi_{XX} & 0 & 0 \\ 0 & 1+\chi_{YY} & 0 \\ 0 & 0 & 1+\chi_{ZZ} \end{bmatrix} \begin{bmatrix} E_X \\ E_Y \\ E_Z \end{bmatrix} \\ &= \begin{bmatrix} \epsilon_{XX} & 0 & 0 \\ 0 & \epsilon_{YY} & 0 \\ 0 & 0 & \epsilon_{ZZ} \end{bmatrix} \begin{bmatrix} E_X \\ E_Y \\ E_Z \end{bmatrix} \end{aligned} \tag{2.22}$$

or:

$$\begin{bmatrix} D_X \\ D_Y \\ D_Z \end{bmatrix} = \epsilon_0 \begin{bmatrix} n_{XX}^2 & 0 & 0 \\ 0 & n_{YY}^2 & 0 \\ 0 & 0 & n_{ZZ}^2 \end{bmatrix} \begin{bmatrix} E_X \\ E_Y \\ E_Z \end{bmatrix} \tag{2.23}$$

Let us consider the energy density of the electric field per unit volume in the principal dielectric axis system:

$$U = \frac{1}{8\pi} \vec{D}\vec{E} = \frac{1}{8\pi} \sum_{ij} \epsilon_{ij} \vec{E_i} \vec{E_j} \tag{2.24}$$

From expressions 2.23 and 2.24, the energy density of electric field can be presented as:

$$U = \frac{1}{8\pi} \left(\frac{D_X^2}{\epsilon_{XX}} + \frac{D_Y^2}{\epsilon_{YY}} + \frac{D_Z^2}{\epsilon_{ZZ}} \right) \tag{2.25}$$

If we let:

$$X = \frac{D_X}{\sqrt{8\pi U}}; \qquad Y = \frac{D_Y}{\sqrt{8\pi U}}; \qquad \text{and} \quad Z = \frac{D_Z}{\sqrt{8\pi U}}$$

And now expression 2.25 becomes:

$$\frac{X^2}{\epsilon_{XX}} + \frac{Y^2}{\epsilon_{YY}} + \frac{Z^2}{\epsilon_{ZZ}} = 1 \tag{2.26}$$

or:

$$\frac{X^2}{n_{XX}^2} + \frac{Y^2}{n_{YY}^2} + \frac{Z^2}{n_{ZZ}^2} = 1 \tag{2.27}$$

The surface described by expression 2.27 is known as the optical indicatrix or the

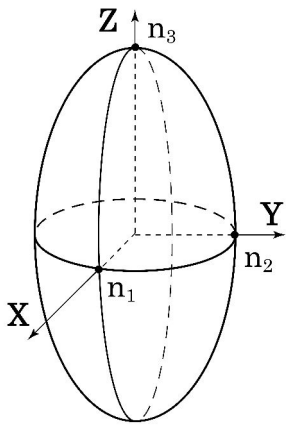

FIGURE 2.7: The index ellipsoid. The coordinate axes X, Y, and Z are the optically principal axes. n_1, n_2, and n_3 are the principal refractive indices of the anisotropic medium.

index ellipsoid which is shown in Fig 2.7. For isotropic media, the surface is a sphere with $n_1 = n_2 = n_3 = n$. For uniaxial crystals, it is an ellipsoid of revolution with $n_1 = n_2 = n_o$ and $n_3 = n_e$ [72]. For biaxial crystals, it is a general ellipsoid with $n_1 \neq n_2 \neq n_3$ [72].

In other coordinate systems $Oxyz$, the index ellipsoid can be written in the form:

$$\left(\frac{1}{n^2}\right)_{xx} x^2 + \left(\frac{1}{n^2}\right)_{yy} y^2 + \left(\frac{1}{n^2}\right)_{zz} z^2 + 2\left(\frac{1}{n^2}\right)_{yz} yz + 2\left(\frac{1}{n^2}\right)_{zx} zx + 2\left(\frac{1}{n^2}\right)_{xy} xy = 1 \tag{2.28}$$

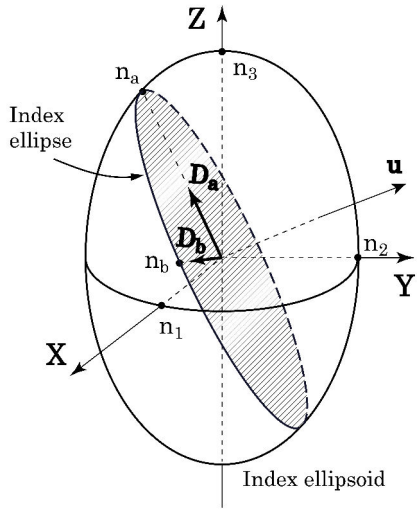

Figure 2.8: Normal mode determined from the index ellipsoid [72, 83].

In an anisotropic medium, the refractive index depends on the propagation and polarization of light. For example, when the light propagates along a principal axis such as Z axis, if it is linearly polarized along X axis, the refractive index is n_1. Likewise, if the polarization is along Y, its refractive index is then n_2. In the general case of light travelling along the direction of the vector $\overrightarrow{u}$ as in Fig. 2.8, one must then draw a plane passing through the origin of the index ellipsoid and perpendicular to the vector $\overrightarrow{u}$. The intersection of this plane with the ellipsoid is an ellipse, called the index ellipse. The half lengths of the major and minor axes of the index ellipse are then the refractive indices n_a and n_b of the two normal modes corresponding to the polarization of the light along those axes [72].

2.4.3 The Pockels effect

A linear dielectric medium (or linear optical medium) is characterized by a linear dependency of the polarization density with the electric field:

$$P = \epsilon_0 \chi E \tag{2.29}$$

where the constant of proportionality χ is known as the linear susceptibility of this medium (in this case of an isotropic medium).

A nonlinear optical medium, on the other hand, is characterized by a nonlinear relation between the polarization density and the electric field. As we know, the polarization density $P = Np$ is a product of the individual dipole moment p induced by the applied electric field E and the density of the N dipole moments. A nonlinear property may be from microscopic or macroscopic origin and the nonlinear behavior may reside either in p or in N. In any case, the polarization density can still be expressed by expression 2.29 but the susceptibility is now field-dependent as shown in the expression below [83]:

$$P = \epsilon_0 \chi(E) E \tag{2.30}$$

Expanding the field-dependent linear susceptibility $\chi(E)$ in Taylor series, leads to:

$$\chi(E) = \chi(0) + \left[\frac{\partial \chi(E)}{\partial E}\right]_{E=0} E + \frac{1}{2!}\left[\frac{\partial^2 \chi(E)}{\partial E^2}\right]_{E=0} E^2 + \dots \tag{2.31}$$

allowing to express the polarization density P is expressed as a power series in the electric field E, as:

$$\begin{aligned} P &= \epsilon_0 \chi^{(1)} E + \epsilon_0 \chi^{(2)} E^2 + \epsilon_0 \chi^{(3)} E^3 + \dots \\ &= P^{(1)} + P^{(2)} + P^{(3)} + \dots \end{aligned} \tag{2.32}$$

where

$$\chi^{(1)} = \chi(0) = \frac{1}{\epsilon_0}\left[\frac{\partial P(E)}{\partial E}\right]_{E=0} \tag{2.33}$$

$$\chi^{(2)} = \left[\frac{\partial \chi(E)}{\partial E}\right]_{E=0} = \frac{1}{2\epsilon_0}\left[\frac{\partial^2 P(E)}{\partial E^2}\right]_{E=0} \tag{2.34}$$

$$\chi^{(3)} = \frac{1}{2!}\left[\frac{\partial^2 \chi(E)}{\partial E^2}\right]_{E=0} = \frac{1}{3\epsilon_0}\left[\frac{\partial^3 P(E)}{\partial E^3}\right]_{E=0} \tag{2.35}$$

are known respectively as the linear (ordinary), second (or quadratic), and third-order (or cubic) nonlinear optical susceptibilities.

In an anisotropic medium, $\chi^{(1)}$ is a second-rank tensor and $\chi^{(2)}$ is a third-rank tensor, etc. Expression 2.32 can now be written:

$$P_i = \epsilon_0 \sum_j \chi^{(1)}_{ij} E_j + \epsilon_0 \sum_{jk} \chi^{(2)}_{ijk} E_j E_k + \epsilon_0 \sum_{jkl} \chi^{(3)}_{ijkl} E_j E_k E_l + \dots \tag{2.36}$$

When light represented by the electric field component $E_j(t) = Re\{E_j(\omega)\exp(i\omega t)\}$ travels through this medium, the polarization density contains a component at the same angular frequency ω given by:

$$P_i(\omega) = \epsilon_0 \sum_j \chi_{ij}^{(1)} E_j(\omega) \tag{2.37}$$

As from expression 2.37, the component of the polarization density at the angular frequency ω of the incoming light depends only on the linear susceptibility. The refractive index of the medium sensed by this beam is then given by expressions 2.27 or 2.28.

In the presence of an additional DC ($\Omega = 0$) or low-frequency electric field (external electric field) given by $E_j(t) = Re\{E_j(\Omega)\exp(i\Omega t)\}$, where the angular frequency Ω is much smaller than that of illumination light ω so that this electric field can be considered as quasi-static and $E_j(\Omega) \approx E_j(0)$, the electric field in the medium is:

$$E_i(t) = E_i(0) + Re\{E_i\exp(i\omega t)\} \tag{2.38}$$

To replace $E_i(t)$ from expression 2.38 into 2.36 and focusing on the component of polarization density at the angular frequency ω, we get:

$$\begin{aligned} P_i(\omega) = \epsilon_0 \sum_j \chi_{ij}^{(1)} E_j(\omega) + 2\epsilon_0 \sum_{jk} \chi_{ijk}^{(2)}(\omega+0;\omega,0)E_j(\omega)E_k(0) \\ + 3\epsilon_0 \sum_{jkl} \chi_{ijkl}^{(3)}(\omega+0+0;\omega,0,0)E_j(\omega)E_k(0)E_l(0) + \dots \end{aligned} \tag{2.39}$$

Apart from the contribution from the linear-order polarization density, additional contributions from the second and third-order of the polarization density are showing-up. These contributions can be considered as a perturbation because the value of $\chi^{(2)}$ and $\chi^{(3)}$ are much smaller (10^{-8} and 10^{-15} times respectively) than that of $\chi^{(1)}$. As a result, there is a small but essential variation of the refractive index of the medium with this light which will be detected as a dephasing term.

If the medium is centrosymmetric such as gases, liquids and certain crystals, the contribution of the third-order polarization density comes-up as the first non-vanishing nonlinear effect whereas the contribution of the second-order or higher-order ones is cancelled by symmetry. In this case, the variation of the refractive

index of the medium is proportional to the square of the external electric field. This effect was discovered by John Kerr in 1875 [72] and bears his name.

For the non-centrosymmetric media such as $NH_4H_2PO_4$ (ADP), KH_2PO_4 (KDP), $LiNbO_3$, $KTiOPO_4$ (KTP), etc which sustain an eventually significant second-order susceptibility $\chi^{(2)}$, components of the polarization density at the angular frequency ω are:

$$\begin{aligned} P_i(\omega) &= \epsilon_0 \sum_j \chi_{ij}^{(1)} E_j(\omega) + 2\epsilon_0 \sum_{jk} \chi_{ijk}^{(2)}(\omega + 0; \omega, 0) E_j(\omega) E_k(0) \\ &= P_i^{(1)}(\omega) + P_i^{\text{Pockels}}(\omega) \end{aligned} \tag{2.40}$$

where:

$$P_i^{\text{Pockels}}(\omega) = 2\epsilon_0 \sum_{jk} \chi_{ijk}^{(2)}(\omega + 0; \omega, 0) E_j(\omega) E_k(0) \tag{2.41}$$

is the Pockels polarization density which is proportional to the amplitude of the externally applied DC field.

One can factor-out in expression 2.40 in the other form:

$$\begin{aligned} P_i(\omega) &= \epsilon_0 \sum_j \left[\chi_{ij}^{(1)} + 2 \sum_k \chi_{ijk}^{(2)}(\omega + 0; \omega, 0) E_k(0) \right] E_j(\omega) \\ &= \epsilon_0 \sum_j \chi_{ij}^{'(1)} E_j(\omega) \end{aligned} \tag{2.42}$$

where the effective linear susceptibility is seen to depend on the externally applied DC field:

$$\chi_{ij}^{'(1)} = \chi_{ij}^{(1)} + 2 \sum_k \chi_{ijk}^{(2)}(\omega + 0; \omega, 0) E_k(0) \tag{2.43}$$

Under the action of the external static or quasi-static electric field, the linear susceptibility tensor is distorted leading to a variation of the refractive index of the medium sensed by light. This effect is named the Pokels effect and is accounted for by the Pockels polarization density $P_i^{\text{Pockels}}(\omega)$ as in expression 2.41. The expression of the index ellipsoid becomes (where the prime symbol refers to the new coefficients):

$$\left(\frac{1}{n^2}\right)_{xx}^{'} x^2 + \left(\frac{1}{n^2}\right)_{yy}^{'} y^2 + \left(\frac{1}{n^2}\right)_{zz}^{'} z^2 + 2\left(\frac{1}{n^2}\right)_{yz}^{'} yz + 2\left(\frac{1}{n^2}\right)_{zx}^{'} zx + 2\left(\frac{1}{n^2}\right)_{xy}^{'} xy = 1 \tag{2.44}$$

The modification of the optical constants $(1/n^2)_{ij}$ by the presence of an external electric field is:

$$\begin{aligned}\Delta\left(\frac{1}{n^2}\right)_{ij} &= \left(\frac{1}{n^2}\right)'_{ij} - \left(\frac{1}{n^2}\right)_{ij} \\ &= \frac{1}{1+\chi^{(1)}_{ij}+2\sum_k \chi^{(2)}_{ijk}(\omega+0;\omega,0)E_k(0)} - \frac{1}{1+\chi^{(1)}_{ij}} \\ &\approx -\frac{2\epsilon_0^2\sum_k \chi^{(2)}_{ijk}(\omega+0;\omega,0)}{\epsilon_{ii}\epsilon_{jj}}E_k(0) \\ &= \sum_k r_{ijk}E_k(0)\end{aligned} \tag{2.45}$$

where:

$$r_{ijk} = -\frac{2\epsilon_0^2}{\epsilon_{ii}\epsilon_{jj}}\chi^{(2)}_{ijk}(\omega+0;\omega,0) \tag{2.46}$$

is the general form for coefficients of the electrooptic tensor. Since the dielectric permeability tensor ϵ_{ij} and second-order susceptibility tensor $\chi^{(2)}_{ijk}$ are real and symmetric, consequently the electrooptic tensor r_{ijk} must be symmetric with respect to permutation of its first two indices. For this reason, it is convenient to represent the third-rank tensor r_{ijk} as a two-dimensional table r_{hk} with 6×3 elements by use of a contracted notation according to the prescription in Table 2.1.

Index	ij	11	22	33	23 or 32	13 or 31	12 or 21
Replacing index	h	1	2	3	4	5	6

Table 2.1: Table of the replacing index.

Expression 2.45 can now be rewritten as:

$$\Delta\left(\frac{1}{n^2}\right)_i = \sum_j r_{ij}E_j(0) \tag{2.47}$$

or explicitly as:

$$\begin{bmatrix} \Delta\left(1/n^2\right)_1 \\ \Delta\left(1/n^2\right)_2 \\ \Delta\left(1/n^2\right)_3 \\ \Delta\left(1/n^2\right)_4 \\ \Delta\left(1/n^2\right)_5 \\ \Delta\left(1/n^2\right)_6 \end{bmatrix} = \begin{bmatrix} r_{11} & r_{12} & r_{13} \\ r_{21} & r_{22} & r_{23} \\ r_{31} & r_{32} & r_{33} \\ r_{41} & r_{42} & r_{43} \\ r_{51} & r_{52} & r_{53} \\ r_{61} & r_{62} & r_{63} \end{bmatrix} \begin{bmatrix} E_1(0) \\ E_2(0) \\ E_3(0) \end{bmatrix} \tag{2.48}$$

Because of the presence of an external electric field, the refractive index of the medium varies an amount of:

$$\Delta n_i = -n_i^3 \sum_j r_{ij} E_j(0) \tag{2.49}$$

With the Pockels effect, the variation of the refractive index of the medium is proportional to the external electric field as from expression 2.49. Which lead to the equivalent terminology of the linear electrooptic effect.

2.4.4 Applications of the Pockels effect

Media with a refractive index that can be modified by the application of an external electric field are useful to produce electrically controllable optical devices such as:

- A lens made of an electrooptic material allowing to control its focal length.
- A prism with controllable beam bending ability by an external voltage to be used as a deflector as in Fig. 2.9.
- Light travelling through a transparent electrooptic plate, the phase shift between the output and the incoming light being:

$$\begin{aligned} \varphi = \varphi_0 + \Delta\varphi_{\mathrm{EO}} &= \frac{2\pi}{\lambda} n_i e + \frac{2\pi}{\lambda} \Delta n_i e \\ &= \frac{2\pi}{\lambda} n_i e \left(1 + n_i^2 \sum_j r_{ij} E_j(0)\right) \end{aligned} \tag{2.50}$$

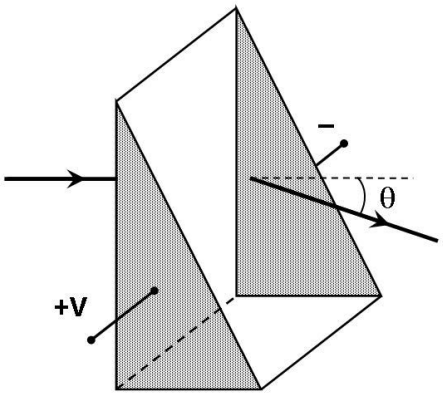

Figure 2.9: An electrooptic prism which the deflection angle θ is controlled by an applied voltage.

where e is the thickness of this plate. The phase of output light can be controlled by an external electric field, so that the plate can be used as an optical phase modulator.

- The Pockels effect is widely applied in optical communications and optical signal-processing applications such as optical modulation as in the Fig. 2.4. The device can be used as an optical switch or a linear intensity modulator by controlling the applied voltage.

- One of the most useful devices based on the Pockels effect is the Pockels cell. S polarized light travelling through Pockels cell experiences an effect similar to that obtained by optical retarders such as quarter or half-wave plates, with the additional benefit here of a control voltage.

  Crystallize materials used to make a Pockels cell are normally uniaxial crystals with an index ellipsoid of revolution about the optic axis (Z) displaying along their principal asix $n_1 = n_2 = n_o$ and $n_3 = n_e$. The crystal is not birefringent for light travelling along the optic axis (Z) because the index ellipse on the XY optical plane for this case is a circle. When an electric field is applied to the crystal with the direction of the electric field along the optic axis, the isotropic circle is deformed into an ellipse and the refractive indices are not equal any

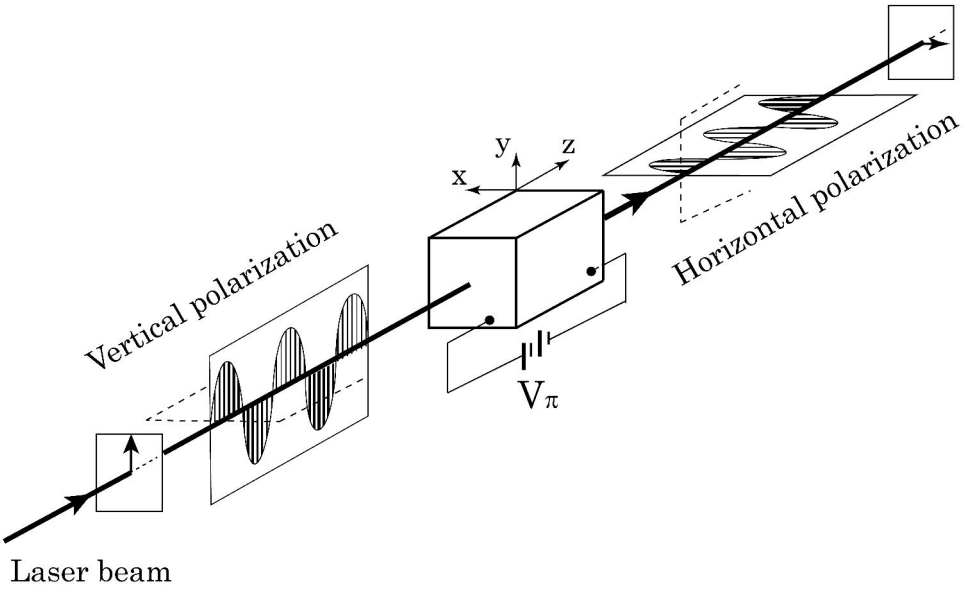

FIGURE 2.10: Example of application of a Pockels cell for the Q-switching. 90° rotation of plane of a linearly polarized light due to an applied voltage V_π which induces a 180° phase shift between the ordinary and extraodinary rays.

more. The crystal appears to be biaxially birefringent in the direction of the optical axis as in the case of a quarter or half-wave plates. The ellipticity of the index ellipse depends on the electric field strength and the linear electrooptic coefficients of the material. Thus the phase shift between the ordinary and extraordinary rays can be controlled by increasing or decreasing the voltage applied to the crystal. Phase shift values between 0°, 90° (corresponding to a quarter-wave plate), and 180° (half-wave plate) are the most useful in practice.

Based on the working principle of the Pockels cell, various applications in optic systems such as Q-switching, ultra fast optical shutters, optical modulator, etc have been developed and are widely used.

2.5 Pockels Linear Electro-Optical Microscopy

The Pockels Linear Electro-Optical Microscopy (PLEOM) was conceived and developed in two previous doctoral thesis [66, 67] in order to study the linear electrooptic

properties of samples (nonlinear optical materials) under the application of an external electric field. While the basic working principles of PLEOM have remained the same, it has been improved to reduce the noise, increase the sensitivity, and be compatible with more and more studied objects of physical or biological nature.

2.5.1 Configuration and working principle of PLEOM

We recall briefly the configuration of the Pockels Linear Electro-Optical Microscopy as shown in Fig. 2.11. Its working principle is based on the Pockels effect in samples submitted to an external electric field. The phase shift experienced by light travelling through the sample reflects the variation of the refractive index which is measured via a Mach-Zehnder interferometer. The Mach-Zehnder interferometer is injected by a stabilized He-Ne laser source with a linearly polarized output. The laser beam is split into two parts by the first polarization beam splitter (PBS1). The transmission part of the laser beam with horizontal polarization is directed onto the sample and is referred to as the sample beam, whereas the reflected beam with vertical polarization serves as a reference beam. The ratio between the transmission and reflection beams is controlled by a half-wave plate which is placed before the first polarization beam splitter. By turning the optical polarization axis of the half-wave plate, the polarization axis of the laser beam is appropriately rotated in such a way that the intensity of the sample beam is below 10% of the total laser power. After traveling through the Pockels cell (PS) which is described in part A.1, the sample beam is focused onto the sample by the first microscope objective and collimated by the second one as in Figs. 2.11 and 2.12.

Two half-wave plates which are mounted on electric motors and computer controlled are placed before and after the two microscope objectives as in Fig. 2.12. When measuring the polarization response, the two half-wave plates are rotated so that their optical axis are maintained parallel to each other at the same $\alpha/2$ angle with respect to the horizontal axis (x) as in Fig 2.12 at each measurement point.

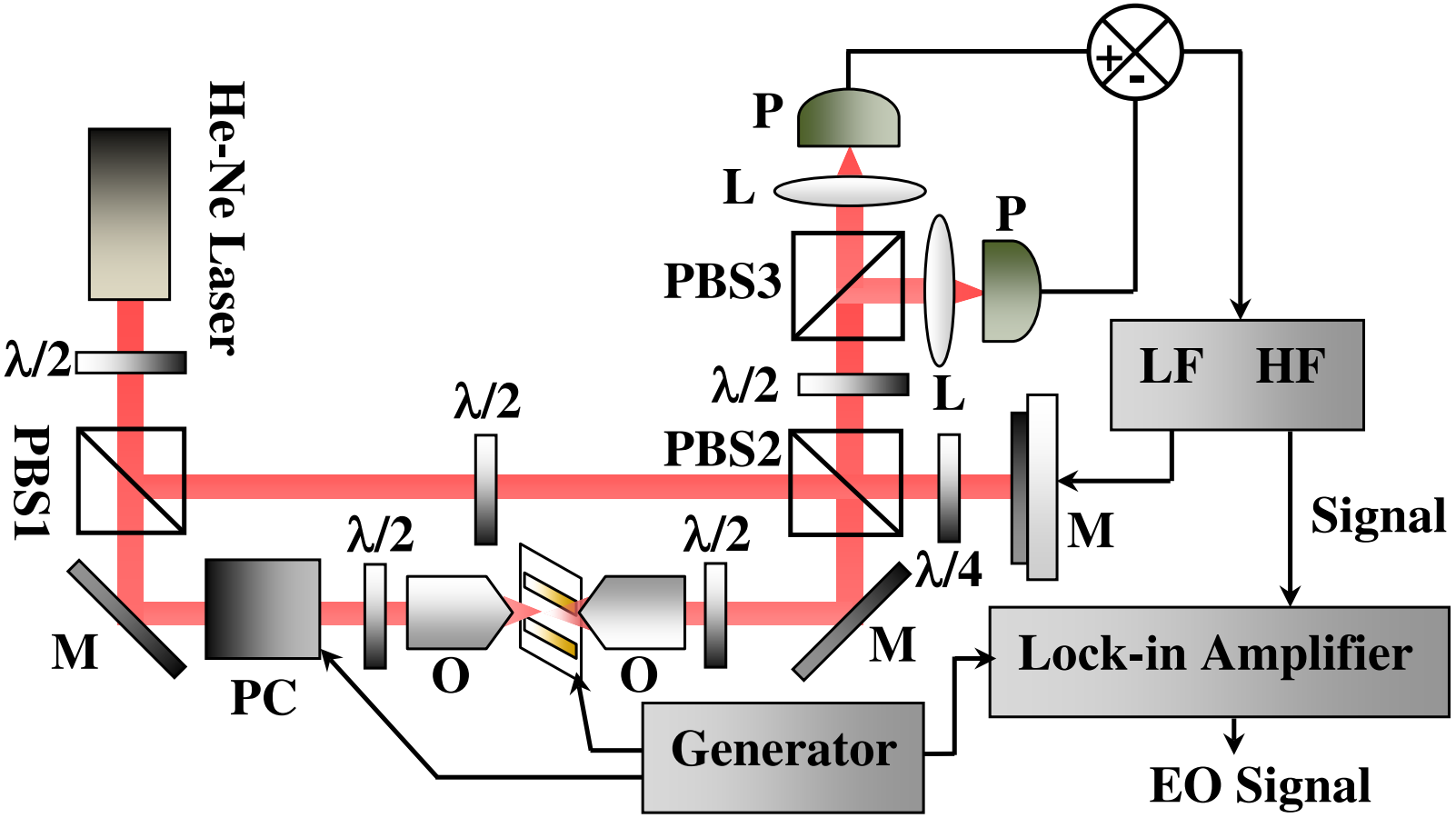

Figure 2.11: General scheme of the PLEOM setup. He-Ne Laser source; PBS, polarization beam splitter; M, mirror; PC, Pockels cell; O, objective; $\lambda/2$, half-wave plate; $\lambda/4$, quater-wave plate; L, lens; P, photodiode; LF, low frequency signal and HF, high frequency signal.

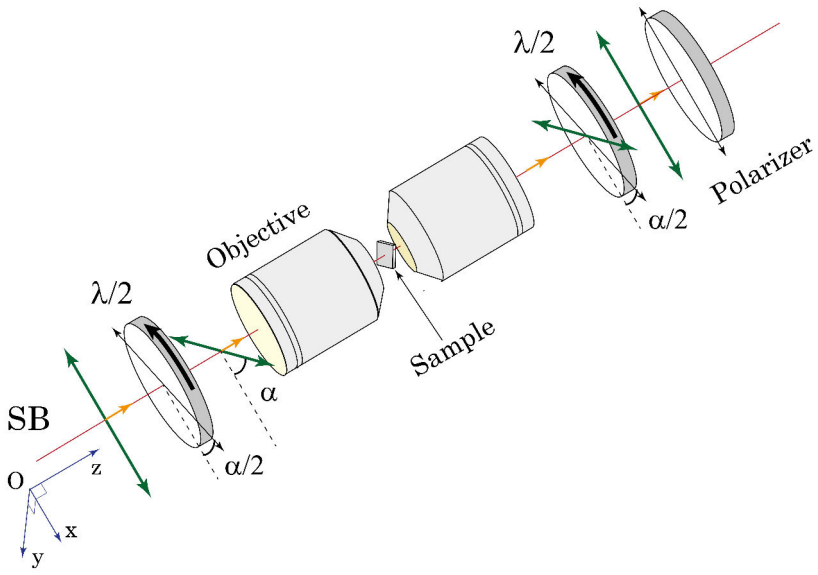

Figure 2.12: Schematic diagram of the part of PLEOM allowing to measure the polarization response from the sample by using two half-wave plates placed before and after two microscope objectives. $Oxyz$, laboratory coordinate system; SB, sample beam; and $\lambda/2$, half-wave plate. The dark green lines with double arrows are the polarization axes of the sample beam along its path.

The polarization axis of the sample beam along its optical path are presented by the dark green lines with double arrows in Fig. 2.12. When traveling through the first half-wave plate, the polarization axis of the sample beam (SB) with respect to the horizontal polarization is rotated by an angle α. After passing through the microscope objectives and sample, the sample beam still maintains the polarization axis at α angle. The second half-wave plate with the polarization axis oriented at $\alpha/2$ angle is used to turn the polarization axis of the sample beam back to the x horizontal polarization. When performing measurements at variable angles α from $0°$ to $360°$, we obtain the intensity polarization response. After passing through some specific samples, the beam can include some additionally generated electro-magnetic wave components at different polarization axis. A polarizer is thus placed behind the second half-wave plate in order to cut such electro-magnetic components that are not polarized along the horizontal direction.

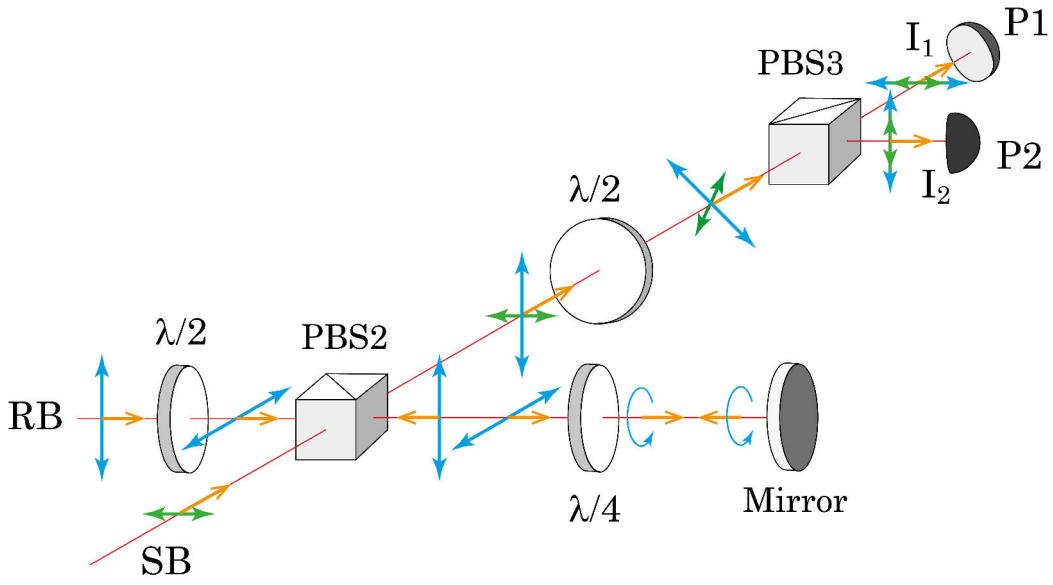

FIGURE 2.13: Schematic diagram of the balanced homodyne detection system used to detect the phase shift between the sample and reference beams of a Mach-Zehnder interferometer. SB, sample beam; RB, reference beam; PBS, polarization beam splitter; $\lambda/2$, half-wave plate; $\lambda/4$, quarter-wave plate; P1, P2, photodiodes; I_1 and I_2, intensities of the beams before the two photodiodes. The blue and dark green lines with double arrows are the polarization axis of the reference and sample beams respectively.

After traveling through the sample, the sample beam including the linear electrooptic signal from the sample is recombined with the reference beam before entering the balanced homodyne detection system as in Fig. 2.13.

In the reference path, a half-wave plate oriented at 45° is used to turn the polarization of the reference beam from vertical to horizontal. The reference beam then passes through the second polarization beam splitter without any reflection, then through a quarter-wave plate oriented at 22.5° so as to become circularly polarized. A mirror which is placed on a piezoelectric stage is used to back-reflect the reference beam and to control its optical path length. After traveling back through the quarter-wave plate, the polarization of the reference beam is transformed from circular to vertically polarized. It is therefore totally reflected at the second polarization beam splitter and recombined with the sample beam. It is then totally transmitted through this splitter as a result of its horizontal polarization as in Fig. 2.13.

After the recombination, they pass through a half-wave plate oriented at 22.5° so that their polarization axis are rotated by 45° as in Fig. 2.13. Each beam is split into two equal parts by the third polarization beam splitter before entering the two photodiodes.

Let us recall the theoretical derivation of the signal detected by the balance homodyne detection system used in PLEOM when there is a variation of the refractive index of the sample under the application of a quasi-static external electric field (Pockels effect). Let us assume that in the absence of external electric field, the

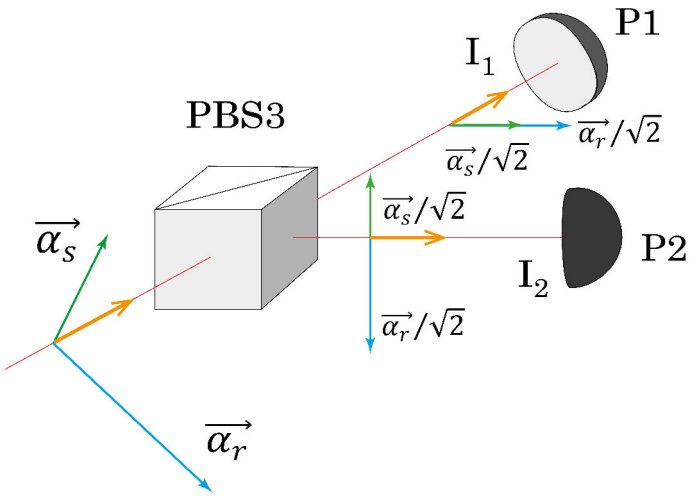

Figure 2.14: Schematic diagram of the balanced homodyne detection system used in PLEOM. $\vec{\alpha_r}$ and $\vec{\alpha_s}$ are the electric field components of the reference and signal beams respectively.

electric field components of the electromagnetic waves of the reference and sample beam ($\xi_r(t)$ and $\xi_s(t)$) at the photodiodes take the following expressions:

$$\xi_r(t) = \frac{1}{\sqrt{2}}\overline{\alpha}_r e^{i(\omega t+\phi)} \tag{2.51}$$

$$\xi_s(t) = \frac{1}{\sqrt{2}}\overline{\alpha}_s e^{i\omega t} \tag{2.52}$$

where $\overline{\alpha}_r$ and $\overline{\alpha}_s$ are the amplitudes of the electric field components of the reference and sample beams respectively as in Fig. 2.14 and ϕ is the different phase between

the reference and sample beams after travelling through their respective optical paths, and is controlled by the mirror as in Fig. 2.13.

When applying an external electric field $E_{ext}(t)$ on the sample expressed as:

$$E_{ext}(t) = \overline{E}_{ext}\cos(\Omega t + \phi_E) \tag{2.53}$$

where Ω is the angular frequency of the external electric field which is much smaller than that of the laser beam ω, and ϕ_E its initial phase. Thus the external electric field can be considered as a quasi-static electric field. It induces a refractive index variation of the sample that can be calculated from expression 2.49. By varying the refractive index of the sample, the phase of the sample beam also varies by an amount $\Delta\varphi(t)$:

$$\Delta\varphi(t) = \overline{\Delta\varphi}\cos(\Omega t + \phi_E) \tag{2.54}$$

with $\overline{\Delta\varphi}$ is the amplitude.

The electric field components of the reference and sample beam at the photodiodes are:

$$\xi_r(t) = \frac{1}{\sqrt{2}}\overline{\alpha}_r e^{i(\omega t+\phi)} \tag{2.55}$$

$$\xi_s(t) = \frac{1}{\sqrt{2}}\overline{\alpha}_s e^{i(\omega t+\Delta\varphi(t))} \tag{2.56}$$

By recombining the reference and sample beams, the electric field of the beams entering the two photodiodes as in Fig. 2.14 are:

$$\xi_1(t) = \xi_r(t) + \xi_s(t) \tag{2.57}$$

$$\xi_2(t) = \xi_r(t) - \xi_s(t) \tag{2.58}$$

which corresponds to light intensities entering the two photodiodes:

$$I_1 = |\xi_r(t) + \xi_s(t)|^2 \tag{2.59}$$

$$I_2 = |\xi_r(t) - \xi_s(t)|^2 \tag{2.60}$$

The photocurrents at the two detectors are respectively:

$$i_1 = \rho_1 I_1 \tag{2.61}$$

$$i_2 = \rho_2 I_2 \tag{2.62}$$

where ρ_1 and ρ_2 are the quantum efficiency of two photodiodes. In the PLEOM setup, the photodiodes are well balaced and have the same quantum efficiency $\rho_1 = \rho_2 = \rho$.

The electronic signal is the difference between the two photocurrents achieved by an electronic circuit as in Fig. 2.11 taking the form:

$$\begin{aligned}\Delta i &= \rho(I_1 - I_2) = i_1 - i_2 \\ &= 4\rho \mathrm{Re}[\xi_r(t)\xi_s(t)^*] = 2\rho \mathrm{Re}[\overline{\alpha}_r e^{i(\omega t+\phi)}\overline{\alpha}_s e^{-i(\omega t+\Delta\varphi(t))}] \\ &= 2\rho \mathrm{Re}[\overline{\alpha}_r\overline{\alpha}_s e^{i(\phi-\Delta\varphi(t))}] = 2\rho\overline{\alpha}_r\overline{\alpha}_s \cos[\phi - \Delta\varphi(t)]\end{aligned} \tag{2.63}$$

The initial phase difference between the reference and sample beams is maintained at the fixed value $\phi = \pi/2$ by moving a feedback mirror on a piezoelectric stage as described in Figs. 2.11 and 2.13. Consequently, the electronic signal in expression 2.63 becomes:

$$\Delta i = 2\rho\overline{\alpha}_r\overline{\alpha}_s \sin(\Delta\varphi(t)) \approx 2\rho\overline{\alpha}_r\overline{\alpha}_s\Delta\varphi(t) \tag{2.64}$$

considering a very small phase shift induced by the Pockels effect in this case (from 10^{-6} to 10^{-2} radian). Replacing $\Delta\varphi(t)$ from the expression 2.54 into 2.64, the expression for the electronic signal becomes:

$$\Delta i = 2\rho\overline{\alpha}_r\overline{\alpha}_s\overline{\Delta\varphi}\cos(\Omega t + \phi_E) = \overline{\Delta i}\cos(\Omega t + \phi_E) \tag{2.65}$$

From expression 2.65 we see that the electronic signal is a sinusoidal function with angular frequency Ω(the modulated frequency). The amplitude $\overline{\Delta i}$ of the electronic signal is proportional to the amplitude $\overline{\Delta\varphi}$ of the electrooptic phase shift and the phase of the signal is the same as (or opposite to) that of the external electric field ϕ_E. The electronic signal is converted into a voltage and detected by a synchronous detector using a lock-in amplifier which will be described in next part.

A Pockel cell (PC in Fig. 2.11) with a known phase shift for light passing through it under the application of an external electric field is used as a reference for the phase shift value. Thus the electronic signal can be converted back to the electrooptic signal $\overline{\Delta\varphi}$.

2.5.2 Detailed structural components of PLEOM

Laser source

The Pockels effect is driven by the same second-order susceptibility $\chi^{(2)}$ as that for Second-Harmonic Generation Microscopy (SHGM) but the advantage of the PLEOM compared with SHGM lies in the simplicity of the laser source. In SHG Microscope, by using a light beam with a very high intensity demanded by a multi-photon process, one needs to use a pulsed laser source with high power output. One may need to use different laser sources or an Optical Parametric Oscillator (OPO) to tune the wavelength of the excited beam, leading to a bulky and expensive systems. The fundamental beam is generally in the IR making difficult in experimental manipulation.

In contrast, PLEOM requires only a simple and low power laser source to detect the variation of the refractive index of the sample by measuring the phase shift sensed by the laser beam when travelling through the sample. We only use a stable CW HeNe laser source with an output power of the order of 1.5 mW at 632.8 nm. The output beam is linearly polarized in the fundamental TEM_{00} mode (Gaussian beam). An optical isolator is used to prevent back reflections which may lead to the instabilities of the output beam. The stability of the intensity is of the order $\pm 0.2\%$. A spatial filter made of an objective lens (magnification $20\times$ and 0.35 NA) and a pinhole of 30 μm diameter permit to clean up the output laser beam.

Optical and mechanical devices

- **Mirrors**: All mirrors were bought from J.Fichou with flatness $\lambda/10$ at 550 nm wavelength. The reflection coefficient of mirrors with s- and p-polarized lights are equal so that of linearly polarized light after the reflection.

- **Polarization beam splitters**: which allow the horizontally polarized part of light to be transmitted while reflecting the vertically polarized part, were bought from Thorlabs.

- **Half-wave plates, quarter-wave plates and polarizer**: are high quality bought from company Thorlabs.

- **Objective lens**: PLEOM has been built to investigate nonlinear materials from nano to larger scale by using two objective lenses in which the first one is used to focus the sample beam onto the sample and the second to collimate the outgoing beam as in Figs. 2.11 and 2.12. In particular, two Nikon microscope objective lenses with magnification 40× and NA 0.6 in air with an extra large working distance of 2.7-3.7 mm are used. The spatial resolution of PLEOM is then given by the size of the focusing spot, with its radius is given by:

$$R = 1.22\frac{\lambda}{2 \times \mathrm{NA}} = 643 \text{ nm} \tag{2.66}$$

  where the $\lambda = 632.8$ nm is the wavelength of the sample beam.

- **Mechanical devices**: were bought from Newport or made in the mechanical shop at ENS Cachan at high precision engineering level.

Photodiodes and Current-Voltage converters

The photodiodes are silicon photodiodes manufactured by Hammamatsu (S5972) with 500 MHz bandwidth. The effective photosensitive area of 0.5 mm^2 allows to ease the alignment constraints.

Each photodiode is connected to a Current-Voltage converter which is used to convert the photocurrent signal to a voltage signal. The converter with a special electronic circuit also helps to split the signal into two parts, one at low frequency and the other at high frequency (with a cut-off frequency at about 9 kHz).

The low frequency part of the signal corresponds to the phase shift between the sample and reference beams due to vibrations or thermal expansion of optical components or holders. The signal part at low frequency is used as a feedback signal to control the motion of the mirror as in Figs. 2.11 and 2.13 which is used to compensate spurious phase shift and maintain the phase difference ϕ between the sample and reference beams at a $\pi/2$ value as described in section 2.5.1. The high

frequency part of the signal originates from the electrooptic signal at the modulated frequency by setting its value above the cut-off frequency. This signal part is then detected by a synchronous detection system at the modulated frequency.

Synchronous detection

In PLEOM, a lock-in Amplifier (EG&G Princeton Applied research model 5302) is employed to detect the electrooptic signal.

After converting, the current signal is expressed in expression 2.65 into a voltage signal, the signal now exhibits the form:

$$V_{sig}(t) = V_{sig}\cos(\Omega t + \phi_{sig}) \tag{2.67}$$

The lock-in amplifier generates its own internal reference signals at the same angular frequency as that of the electrooptic signal:

$$V_{L1}(t) = V_L\cos(\Omega t + \phi_L) \tag{2.68}$$

$$V_{L2}(t) = V_L\sin(\Omega t + \phi_L) \tag{2.69}$$

where the V_L and ϕ_L are the amplitude and phase of the reference signal respectively.

After that, the measured signal is multiplied by each reference signal which gives two output electronic signals V_1 and V_2 respectively:

$$\begin{aligned} V_1 &= V_{sig}V_L\cos(\Omega t + \phi_{sig})\cos(\Omega t + \phi_L) \\ &= \frac{1}{2}V_{sig}V_L\cos(\phi_L - \phi_{sig}) + \frac{1}{2}V_{sig}V_L\cos(2\Omega t + \phi_L + \phi_{sig}) \end{aligned} \tag{2.70}$$

$$\begin{aligned} V_2 &= V_{sig}V_L\cos(\Omega t + \phi_{sig})\sin(\Omega t + \phi_L) \\ &= \frac{1}{2}V_{sig}V_L\sin(\phi_L - \phi_{sig}) + \frac{1}{2}V_{sig}V_L\sin(2\Omega t + \phi_L + \phi_{sig}) \end{aligned} \tag{2.71}$$

From expressions 2.70 and 2.71 we see that each output electronic signal includes two signals in which one is a DC signal and the other one is a AC signal at the doubled frequency 2Ω. The output electronic signals are passed through a low pass filter in which the AC signals are removed. The filtered output electronic signals

now become:

$$V_1 = \frac{1}{2} V_{sig} V_L \cos(\phi_L - \phi_{sig}) \sim V_{sig} \cos\phi \tag{2.72}$$

$$V_2 = \frac{1}{2} V_{sig} V_L \sin(\phi_L - \phi_{sig}) \sim V_{sig} \sin\phi \tag{2.73}$$

where $\phi = \phi_L - \phi_{sig}$ is the difference between the phases of the electrooptic signal and that of the reference signal from the lock-in amplifier.

The amplitude of the output electronic signal and the phase difference can be inferred therefrom:

$$V = \sqrt{V_1^2 + V_2^2} = V_{sig} V_L \tag{2.74}$$

$$\tan\phi = \frac{V_2}{V_1} \tag{2.75}$$

The weak intensity V_{sig} of the input signal, is amplified by the lock-in amplifier by a V_L gain coefficient so as to reach a strong intensity V. By using a synchronous detection system, we can reach both the intensity and phase of the signal.

Piezoelectric stage

As in standard confocal microscopy, PLEOM has been using a piezoelectric stage to scan the position of the focusing spot of the sample beam over the chosen area on the sample which is mounted on a plate. The 2D or 3D mapping can then be performed. We use piezoelectric stages from PiezoJena (Tritor 102) with a maximum displacement along x, y and z axes of about 80 micrometer.

Generator

A Tektronix AFG (3922B) commercial generator with two output channels is used to generate a voltage applied to electrodes, then leading to the external electric field on the studied sample. During the experiment, the parameters of the output voltage from the generator such as the amplitude, the offset, and the frequency (modulated frequency) are controlled by the software through the connection between the computer with the generator by a GPIB interface.

By using a synchronous detection to detect the signal, the lock-in amplifier needs to be fed by a reference frequency with the same value as that of the signal. As described in section 2.5.1, the frequency of the signal is that of the external electric field from the generator. The input reference channel of the lock-in amplifier is connected to the generator as in Fig. 2.11.

Pockels cell

The Pockels cell bought from LEYSOP LTD is used as a reference to convert the electronic signal of the measurements to a phase shift signal. Normally, this Pockels cell is used as a laser Q-switch or as an intensity or a phase modulator under the application of a high DC Voltage. In this case, it is working under application of an AC voltage. The phase shift of light which travels through the Pockels cell can be derived from either the electrooptic effect and the elasto-optic effect which is induced by the piezoelectric effect under the application of that electric field. All parameters pertaining to those effects for KD*P are reported for a DC voltage. In our case when it is to be used as a reference for phase shift under application of an AC voltage, more investigations are needed. It will be described in Appendix A.1.

2.5.3 Alternative configuration for PLEOM

In the previous PLEOM configuration as in Fig. 2.11, we use two objective lenses, one to focus the beam onto the sample and the second one to collimate the outgoing beam (including the transmission and scattering beam), so that PLEOM can only be used in this configuration to study transparent samples.

Towards further aims such as the determination of the linear electrooptic surface scattering of samples from nano to bulk scale or non-transparent samples, another configuration that is based on the previous the PLEOM setup has been built as in Fig. 2.15. The working principle of the new PLEOM setup is basically the same as that of the previous one but in this case, only one microscope objective is used to focus the beam onto the sample so as to collect the scattering and back-reflected

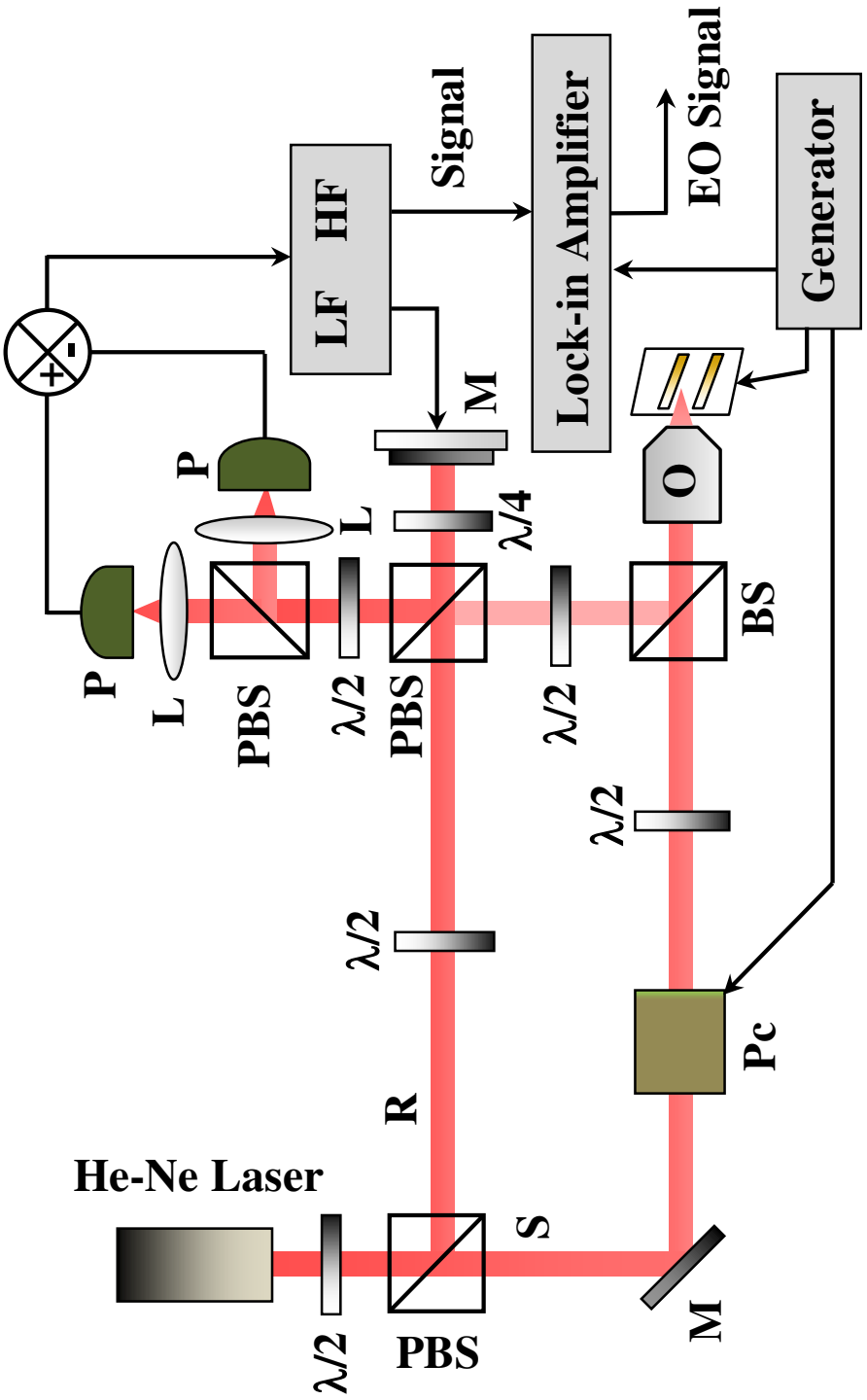

Figure 2.15: General scheme for the alternative configuration of PLEOM in reflection. He-Ne Laser source; PBS, polarization beam splitter; R, reference beam; S, sample beam; M, mirror; Pc, Pockels cell; O, objective; $\lambda/2$, half-wave plate; $\lambda/4$, quater-wave plate; L, lens; P, photodiode; LF, low frequency signal and HF, high frequency signal.

emission. After that the scattered and reflected beams are recombined with the reference beam in the balanced homodyne detection system. Another advantage of PLEOM is the facility to switch between these two configurations without the need for any complicated alignment procedure.

2.5.4 Experimental data acquisition by PLEOM

By using a balanced homodyne detection system and synchronous detection for signal processing, we monitor the amplitude and phase of signal as in expressions 2.74 and 2.75. The piezoelectric stage with mounted sample allows us perform 2D or 3D scanning over the chosen zone, leading to amplitude and phase image as in Figs. 2.16a and 2.16b respectively.

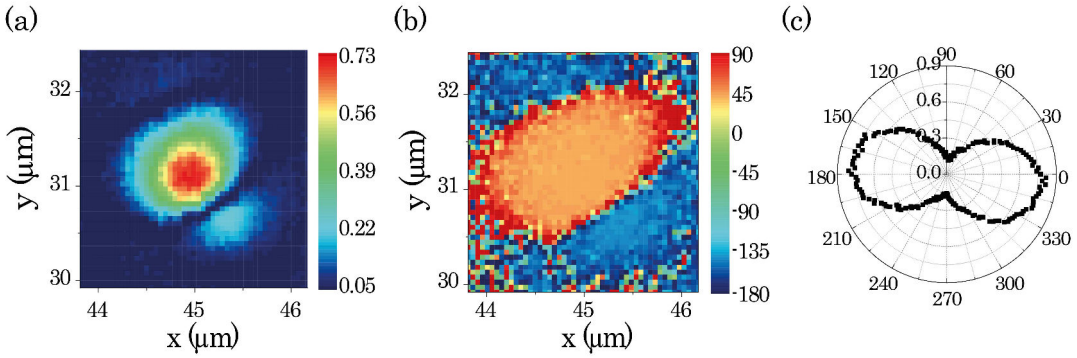

FIGURE 2.16: Example of images acquired by PLEOM. (a) 2D amplitude image; (b) 2D phase image and (c) intensity polarization plot.

By using two half-wave plates as described in section 2.5.1, the angle between the polarization axis of the sample beam with respect to the x axis (laboratory frame) is rotated from 0° to 360° which yields the intensity polarization plot as in Fig. 2.16c.

The computer (PC) controlled generator allows to manage the amplitude, the modulated frequency, and the DC offset value of the external electric field. Thus the linear dependence between the signal and the external electric field from the Pockels effect can be checked and other operations like comparing the signal at the modulated frequency with the DC offset value can be performed.

3

A full vector determination for the spontaneous polarization of randomly orientated ferroelectric nano-crystals

In this chapter, we present a new method for accurately extracting the orientation of the dielectric dipole moment of ferroelectric crystals at the nano-scale. The linear electrooptic scattering response from ferroelectric $KTiOPO_4$ (KTP) nano-crystals is reported in this chapter. Using different polarization states for the incident light to measure the intensity polarization response and combining with the phase signal of the response to extract the random orientation of a ferroelectric nano-crystal leads to full polar information on ferroelectric domains. The linear electro-optical response from ferroelectric nano-crystal under illumination by a low intensity laser beam bears

a low-cost non-invasive sub-wavelength probe of major interest for nano-sciences and biological applications. It also promises a new sub-wavelength microscopy for checking the quality of the 1D, 2D and 3D quasi phase matched crystalline NLO devices from nano to macroscopic scale.

3.1 Introduction

Over the last decades, one could witness the fast development of a broad range of probe techniques using different approaches and materials towards physical and biological applications. Towards biological applications, optical methods are particularly useful in view of their non-invasiveness. Fluorescence microscopy, dye molecules or genetically engineered fluorescent proteins, are becoming broadly used tools to investigate cells, tissues and living organs [84]. The limitation of dyes lies in their tendency to photobleaching and phototoxicity, which set limits in the recording time. In order to overcome these limitations, quantum dots [85, 86] and other systems such as nanodiamonds with emission properties arising from color centers [87] are potential candidates to substitute dye molecules. Nevertheless, their luminescence is limited by the saturation in connection with their excited-state lifetime and blinking [86, 88]. Because of the large ratio between surface and volume at the nano-scale, surface effects become significant and may affect the photoluminescence properties. Adequate surface treatment may prevent blinking but remains an additional complication [89].

Second harmonic generation (SHG) is a nonlinear optical process in which two photons at the same frequency of the incoming photons are combined to generate a new photon at twice the energy (doubled frequency). It results from the interaction between light and a nonlinear material deprived of inversion symmetry [4]. In the case of inorganic single crystals widely used for laser frequency doubling, the frequency of the excited light and of the generated harmonic are far from resonance, ensuring photostability and the absence of blinking. Furthermore the intensity of

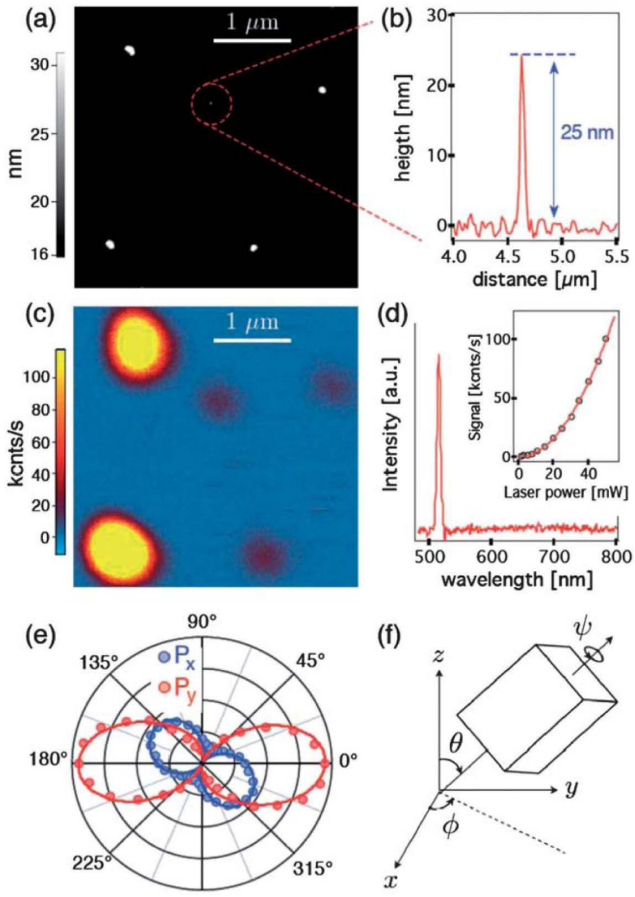

Figure 3.1: SHG from single KTP nanocrystals. (a) AFM image of dispersed KTP nanocrystals. (b) Typical nanocrystal height around 25 nm, measured by AFM in contact mode. (c) Associated SHG 2D image measured for 30 mW mean incident power. (d) Emission spectrumrecorded for 1064nm excitation wavelength. The inset shows the quadratic evolution of the intensity with the excitation power, as characteristic of SHG. (e) Experimental polar response measured along the x and y transverse axis for the nanocrystal selected in (a) and (b). (f) Definition of Euler angles associated with the nanocrystal orientation. The lines in (e) correspond to a nonlinear dipole emission with ($\Theta = 118°$, $\Phi = 148°$, $\Psi = 76°$) [58].

the harmonic beam is quadratically dependent with the intensity of the fundamental beam so that the saturation effect of the emission beam can be avoided contrary to the case of fluorescent dye molecules. With those advantages, SHG have a great potential as labels for nanoprobe materials at the nano-scale techniques. The recent development of nonlinear second harmonic generation microscopy has produced many nanoscale objects such as quantum dots [62, 90, 91], nonlinear molecular crystals

[92, 93], metallic nanospheres [94, 95] or noncentrosymmetric nanocrystals [53, 55–57, 60, 96, 97] which contribute to imaging applications in biology [49, 58, 98–102].

In the case of well behaved ferroelectric nanocrystals as probes for the second-harmonic generation microscopy, each nano-crystal can be considered as a single ferroelectric domain with specific non-zero spontaneous polarization $\overrightarrow{P}$ (dielectric dipole moment per unit volume). Beside quadratically depending on the intensity of the fundamental beam, the intensity of the harmonic beam depends on the relation between the polarization state of the incoming fundamental beam and on the vectorial orientation of the dipole moment of individual nano-crystals [4]. Therefore when using nanocrystals as the probes for second-harmonic generation microscopy, a prerequisite requirement is to fully determine their orientation. Different methods have been demonstrated to determine the random orientation of each nonlinear nanocrystal such as from the intensity polarization responses [53, 55, 58, 62, 92, 93, 97] as in Fig. 3.1, defocused imaging [56] or balanced homodyne detection of the second-harmonic [57]. However using a photodetector to collect the intensity of the gener-

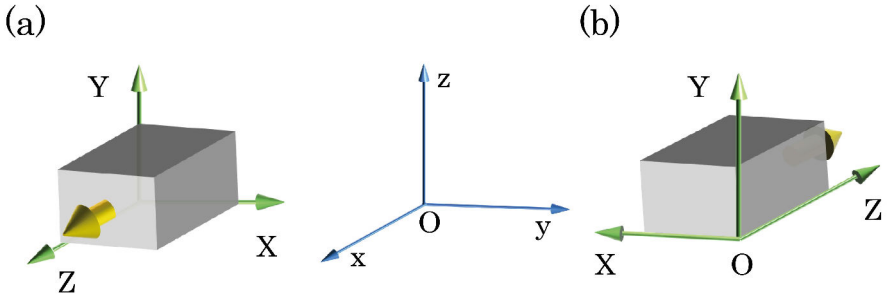

FIGURE 3.2: Two opposite ferroelectric nano-crystals have the same second-harmonic response. $OXYZ$ is the crystal frame and the yellow arrows stand for the dielectric dipole moment vector $\vec{P}$. $Oxyz$ is the laboratory frame.

ated beam does not allow to discriminate between opposed values $+\chi^{(2)}$ and $-\chi^{(2)}$ as shown in Fig. 3.2. Intensity dependent methods can only determine the absolute direction of the dielectric dipole moment vector $\overrightarrow{P}$ of each ferroelectric domain but does not allow to access its sign. When using balanced homodyne detection of

the second-harmonic signal to study ferroelectric crystals, Le Xuan et al [57] could distinguish two opposite bulky crystals by using both the intensity and phase of the generated beam. However their approach had not been applied to ferroelectric nano-crystals with random orientation. Second-harmonic generation as such can only provide the axial, but not the vectorial orientation of a random ferroelectric nano-crystal.

The working principle of PLEOM is based on the Pockels effect which is associated to the second-order susceptibility $\chi^{(2)}$ of nonlinear materials. PLEOM can be used in second-harmonic generation microscopy to map the second-order susceptibility $\chi^{(2)}$ of nonlinear materials [1, 2] and study ferroelectric nanocystals as reported by Hajj et all [3]. From the polarization electrooptic response of single nanocrystals, Hajj et all could extract the absolute direction of each nano-particle. PLEOM has the potential to further provide additional polar information as will be presented in this chapter.

Among the clan of ferroelectric materials, Potassium Titanyl Phossphate (KTP or $KTiOPO_4$) stands-out as a broadly used nonlinear material that has been shown to have superior properties for several nonlinear optical applications such as for frequency doubling of high power lasers because of its high nonlinear optical coefficients d_{ij}, high optical damage threshold and thermal stability [103]. Due to its large linear electrooptic r_{ij} coefficients and low dielectric constants [104, 105], KTP is a good candidate for various electrooptic applications such as Q-switches [106] and modulators [107]. We have therefore selected KTP nano-crystals as nano-probes to be used in PLEOM.

3.2 Potassium Titanyl Phossphate: structure and optical properties

3.2.1 Structure of Potassium Titanyl Phossphate

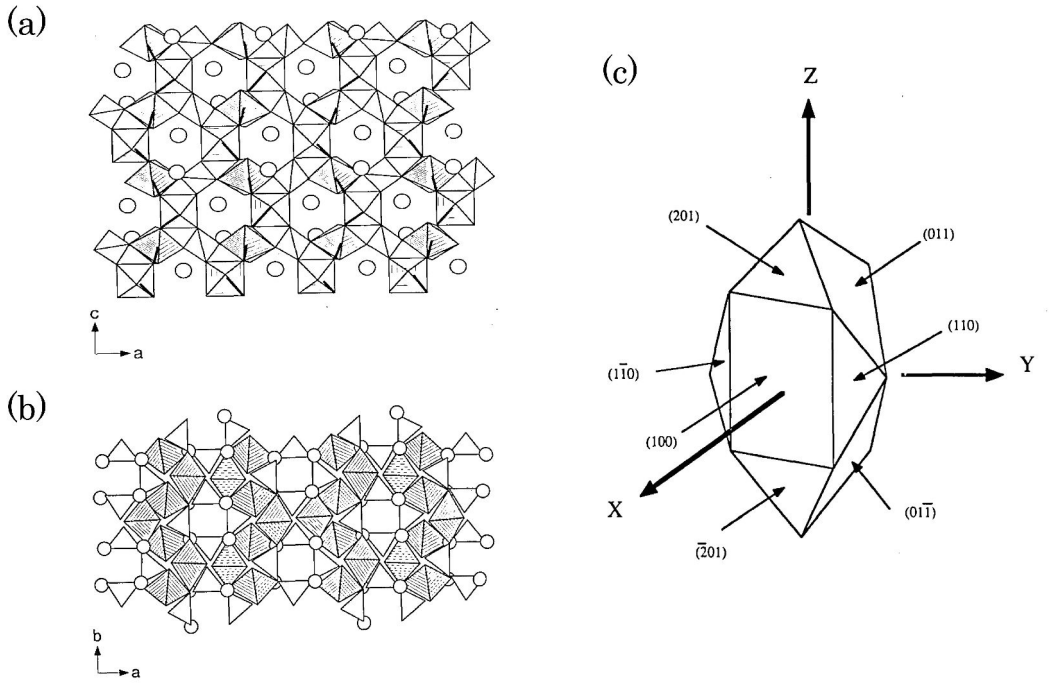

FIGURE 3.3: KTP crystal structure: (a) $a-c$ projection, (b) $a-b$ projection. Shaded elements are the Ti octahedra, open elements are the P tetrahedra and open circles are the K. The bold lines express the short Ti-O bonds. (c) Natural KTP crystal morphology [104].

KTP belongs to a family of inorganic crystal with chemical formula $A\mathrm{TiO}B\mathrm{O}_4$, where A can be K, Rb, Tl, NH_4 or Cs and B can be P or As. This family is orthorhombic and belongs to the acentric point group $mm2$. Each unit cell of KTP crystal contains eight units and exhibits lattice constants $a = 12.814$ Å, $b = 6.404$ Å and $c = 10.616$ Å. The structure is characterized by chains of TiO_6 octahedra which are linked at two corners and are separated by PO_4 tetrahedra as in Fig. 3.3. There are two chains per unit cell and the chain direction alternates between

[011] and $[0\bar{1}1]$. The result of the non-zero spontaneous polarization is from the alternating long and short Ti-O bonds which occur along the chains. Consequently the dielectric dipole moment vector of KTP crystal is along the Z direction. The K ion occupies a high coordination number site and is weakly bonded to both the Ti and P tetrahedra [104].

3.2.2 Nonlinear optical properties of Potassium Titanyl Phosphate

KTP is a negative biaxial crystal ($n_X < n_Y < n_Z$) with optically principal axis X, Y and Z parallel to the crystallographic axis a, b and c respectively as in Fig. 3.3. The relation between the refractive index of KTP crystal and the wavelength of the light is empirically described by the well known Sellmeier equation [103]:

$$n^2 = A + \frac{B}{\lambda^2 - C} + \frac{D}{\lambda^2 - E} \tag{3.1}$$

where λ is the vacuum wavelength in micrometers and A, B, C, D, and E are given in Table 3.1.

Index	A	B	C	D	E
n_X	3.29100	0.04140	0.03978	9.35522	31.45571
n_Y	3.45018	0.04341	0.04597	16.98825	39.43799
n_Z	4.59423	0.06206	0.04763	110.80672	86.12171

Table 3.1: Table of Sellmeier equation coefficients [103].

KTP belongs to the $mm2$ point group so that the second-order nonlinear optical matrix has the form [41]:

$$[d] = \begin{bmatrix} 0 & 0 & 0 & 0 & d_{15} & 0 \\ 0 & 0 & 0 & d_{24} & 0 & 0 \\ d_{31} & d_{32} & d_{33} & 0 & 0 & 0 \end{bmatrix} \tag{3.2}$$

with the following values for the nonlinear optical coefficients: $d_{15} = 6.1$ pm/V; $d_{24} = 7.6$ pm/V; $d_{31} = 6.5$ pm/V; $d_{32} = 5.0$ pm/V and $d_{33} = 13.7$ pm/V.

The electrooptic tensor can be simplified into:

$$[r] = \begin{bmatrix} 0 & 0 & r_{13} \\ 0 & 0 & r_{23} \\ 0 & 0 & r_{33} \\ 0 & r_{42} & 0 \\ r_{51} & 0 & 0 \\ 0 & 0 & 0 \end{bmatrix} \tag{3.3}$$

where the values of the non-zero coefficients at 632.8 nm are given in Table 3.2.

Coefficient	r_{13} (pm/V)	r_{23} (pm/V)	r_{33} (pm/V)	r_{42} (pm/V)	r_{51} (pm/V)
Low Frequency	9.5	15.7	36.3	9.3	7.3
High Frequency	8.8	13.8	35.0	8.8	6.9

TABLE 3.2: Table of linear electrooptic coefficients of KTP [41, 104, 105].

3.3 Theoretical calculation of Pockels linear electrooptic scattering of KTP nano-crystal

In this study, we used the $z-x-z$ convention for the description of rotations using Euler angles in order to relate between two coordinate frames by performing three rotations as shown in Fig. 3.4.

The transformation matrix for each rotation step are respectively

$$V = \begin{bmatrix} \cos\psi & -\sin\psi & 0 \\ \sin\psi & \cos\psi & 0 \\ 0 & 0 & 1 \end{bmatrix} \quad U = \begin{bmatrix} 1 & 0 & 0 \\ 0 & \cos\theta & -\sin\theta \\ 0 & \sin\theta & \cos\theta \end{bmatrix} \quad Q = \begin{bmatrix} \cos\sigma & -\sin\sigma & 0 \\ \sin\sigma & \cos\sigma & 0 \\ 0 & 0 & 1 \end{bmatrix} \tag{3.4}$$

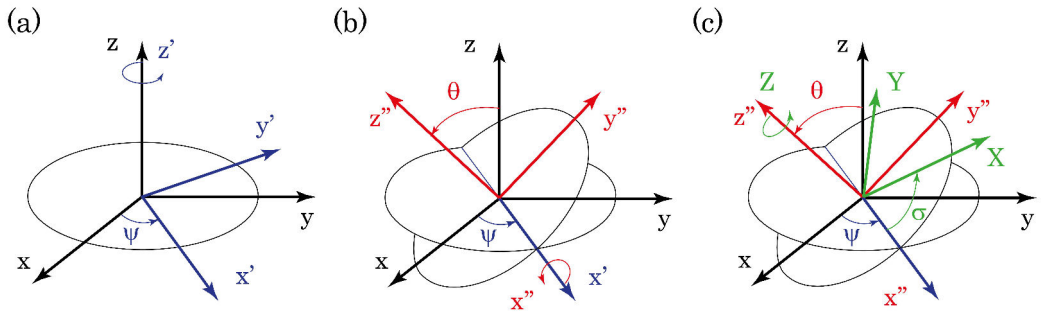

Figure 3.4: The relation between the $Oxyz$ and $OXYZ$ coordinates through the Euler angles (ψ, θ, σ) by performing three rotations around $z-x-z$ axis respectively. (a) The first rotation step is around the z-axis by the angle ψ, (b) the second step is to rotate around the new $x^{'}$ axis by the angle θ and (c) the last step is to rotate around the new $z^{''}$ axis by the angle σ.

where U, Q, and U are the rotation matrix of three rotations.

The transformation matrix T is the product of three matrices:

$$T = VUQ$$
$$= \begin{bmatrix} \cos\psi\cos\sigma - \sin\psi\cos\theta\sin\sigma & -\cos\psi\sin\sigma - \sin\psi\cos\theta\cos\sigma & \sin\psi\sin\theta \\ \sin\psi\cos\sigma + \cos\psi\cos\theta\cos\sigma & -\sin\psi\sin\sigma + \cos\psi\cos\theta\cos\sigma & -\cos\psi\sin\theta \\ \sin\theta\sin\sigma & \sin\theta\cos\sigma & \cos\theta \end{bmatrix} \tag{3.5}$$

T is used to convert a vector in the $OXYZ$ coordinate to the one in the $Oxyx$ coordinate and conversely the inverse transformation will be done by using the inverse matrix $T^{'}$ with:

$$T' = T^{-1} \tag{3.6}$$

These transformation operators will be applied in the case of random orientation of a single KTP nano-crystal in which the $Oxyz$ is the laboratory frame and $OXYZ$ is the crystal frame as in Fig. 3.5.

In the case of a single nonlinear nano-crystal under optical illumination (the sample beam of PLEOM) in the presence of an externally applied quasi-static field (with angular frequency Ω much smaller than that of the optical beam ω), the components of the linear electrooptic polarization of the nano-crystal can be expressed

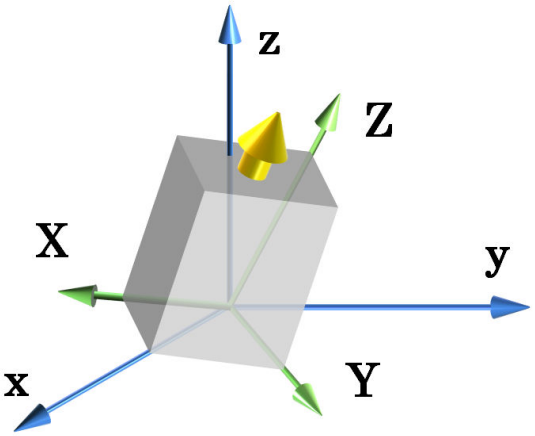

FIGURE 3.5: The random orientation of a single KTP nano-crystal can be defined by three Euler angles (ψ, θ, σ). $OXYZ$ is the crystal frame and $Oxyz$ is the laboratory frame. The yellow arrow is the dielectric dipole moment vector $\vec{P}$.

as:

$$P_i^{\text{Pockels}} \propto \epsilon_0 \sum_j \sum_k r_{ijk} E_j^{\omega} E_k^{\Omega} \tag{3.7}$$

where i, j, and k are Cartesian indices in the principal dielectric frame; E_j^{ω} is the optical field component along the j axis; E_k^{Ω} is the k component of the external quasi-static electric field, and r_{ijk} are the components of the electrooptic Pockels tensor $[r_{ijk}]$. $[r_{ijk}]$ is a third-rank tensor which is reduced to a two-dimensional matrix $[r_{hk}]$ by using conventional contracted notation as already recalled in the Table 2.1. The condensed electrooptic tensor for KTP was already depicted in expression 3.3 while its coefficients take the values as listed in Table 3.2.

The electric field of the scattered electromagnetic wave generated by the nano-crystal is proportional to the second derivative in time of the Pockels dielectric polarization:

$$\overrightarrow{E}_{scat}^{\omega+\Omega} \propto \frac{\partial^2 \overrightarrow{P}^{\text{Pockels}}}{\partial t^2} = -(\omega+\Omega)^2 \overrightarrow{P}^{\text{Pockels}} \tag{3.8}$$

Replacing the P_i^{Pokels} from expression 3.7 into 3.8 we have:

$$(E_{scat}^{\omega+\Omega})_i \propto -\epsilon_0 (\omega+\Omega)^2 \sum_j \sum_k r_{ijk} E_j^{\omega} E_k^{\Omega} \tag{3.9}$$

Assuming that the external electric field polar is directed along the x axis (in the

laboratory frame) and can be expressed as:

$$\overrightarrow{E}^{\Omega} = \begin{pmatrix} 1 \\ 0 \\ 0 \end{pmatrix} E_0^{\Omega} e^{i(\Omega t + \varphi_E)} \tag{3.10}$$

where E_0^{Ω} is the amplitude and φ_E the initial phase.

In this experimental configuration, the sample beam propagates along z direction. The angle α between the polarization axis of the sample beam and the x axis is controlled by the first half-wave plate as in Fig. 2.12. Thus the electric field of the sample beam takes the following expression:

$$\overrightarrow{E}^{\omega} = \begin{pmatrix} \cos\alpha \\ \sin\alpha \\ 0 \end{pmatrix} E_0^{\omega} e^{i(\omega t + \varphi_0)} \tag{3.11}$$

where E_0^{ω} is the amplitude.

By using the inverse transformation matrix $T^{'}$ (inverse of T) connecting the laboratory and crystal frames, the external and optical electric field can be rewritten in the $OXYZ$ crystal frame as:

$$E_i^{'\Omega} = \sum_j T'_{ij} E_j^{\Omega} = T'_{i1} E_0^{\Omega} e^{i(\Omega t + \varphi_E)} \tag{3.12}$$

$$E_i^{'\omega} = \sum_j T'_{ij} E_j^{\omega} = (T'_{i1}\cos\alpha + T'_{i2}\sin\alpha) E_0^{\omega} e^{i(\omega t + \varphi_0)} \tag{3.13}$$

Introducing expressions 3.12 and 3.13 into expression 3.9, electric field components of the scattered electromagnetic wave are now expressed in the crystal frame $OXYZ$ as:

$$(E_{scat}^{'\omega+\Omega})_i \propto -\epsilon_0(\omega+\Omega)^2 \sum_j \sum_k r_{ijk} T'_{j1}(T'_{k1}\cos\alpha + T'_{k2}\sin\alpha) \times E_0^{\Omega} E_0^{\omega} e^{i[(\omega+\Omega)t+\varphi_0+\varphi_E]} \tag{3.14}$$

The electric field components of the scattered electromagnetic wave can now be back transformed in the laboratory frame $Oxyz$ by using the transformation matrix T

(inverse of $T^{'}$):

$$(E_{scat}^{\omega+\Omega})_i = \sum_j T_{ij}(E_{scat}^{'\omega+\Omega})_j \tag{3.15}$$

After passing through the second half-wave plate as in Fig. 2.12, the scattered light will be rotated around the z axis by an angle $-\alpha$. So the electric field components of the scattered light $\overrightarrow{E}_{scat}^{\omega+\Omega}$ will become $\overrightarrow{E}_{scat}^{''\omega+\Omega}$ by using the transformation matrix V as in expression 3.4 with the rotation angle $-\alpha$:

$$\begin{bmatrix} (E_{scat}^{''\omega+\Omega})_1 \\ (E_{scat}^{''\omega+\Omega})_2 \\ (E_{scat}^{''\omega+\Omega})_3 \end{bmatrix} = \begin{bmatrix} \cos\alpha & \sin\alpha & 0 \\ -\sin\alpha & \cos\alpha & 0 \\ 0 & 0 & 1 \end{bmatrix} \begin{bmatrix} (E_{scat}^{\omega+\Omega})_1 \\ (E_{scat}^{\omega+\Omega})_2 \\ (E_{scat}^{\omega+\Omega})_3 \end{bmatrix} \tag{3.16}$$

After the half-wave plate, we insert a polarizer with horizontal polarization axis(along x axis) which projects the scattered $(E_{scat}^{''\omega+\Omega})_1$ electric field along x, leading to:

$$\begin{aligned}(E_{scat}^{''\omega+\Omega})_1 &= (E_{scat}^{\omega+\Omega})_1\cos\alpha + (E_{scat}^{\omega+\Omega})_2\sin\alpha \\ &= \sum_i T_{1i}(E_{scat}^{'\omega+\Omega})_i\cos\alpha + \sum_i T_{2i}(E_{scat}^{'\omega+\Omega})_i\sin\alpha\end{aligned} \tag{3.17}$$

Replacing $(E_{scat}^{'\omega+\Omega})_i$ in 3.17 by its expression in 3.14:

$$\begin{aligned}(E_{scat}^{''\omega+\Omega})_1 \propto &-(A\cos^2\alpha + B\sin\alpha\cos\alpha + C\sin^2\alpha) \\ &\times \epsilon_0(\omega+\Omega)^2 E_0^{\Omega} E_0^{\omega} e^{i[(\omega+\Omega)t+\varphi_0+\varphi_E]}\end{aligned} \tag{3.18}$$

where

$$A = T_{11}T_{11}^{'}T_{31}^{'}(r_{13}+r_{51}) + T_{12}T_{21}^{'}T_{31}^{'}(r_{23}+r_{42}) + T_{13}(T_{11}^{'2}r_{51} + T_{21}^{'2}r_{42} + T_{31}^{'2}r_{33}) \tag{3.19}$$

$$\begin{aligned}B = &T_{11}(T_{12}^{'}T_{31}^{'}r_{13} + T_{11}^{'}T_{32}^{'}r_{51}) + T_{12}(T_{31}^{'}T_{22}^{'}r_{23} + T_{32}^{'}T_{21}^{'}r_{42}) \\ &+ T_{13}(T_{11}^{'}T_{12}^{'}r_{51} + T_{21}^{'}T_{22}^{'}r_{42} + T_{31}^{'}T_{32}^{'}r_{33}) + T_{21}T_{11}^{'}T_{31}^{'}(r_{13}+r_{51}) \\ &+ T_{22}T_{21}^{'}T_{31}^{'}(r_{23}+r_{42}) + T_{23}(T_{11}^{'2}r_{51} + T_{21}^{'2}r_{42} + T_{31}^{'2}r_{33})\end{aligned} \tag{3.20}$$

$$\begin{aligned}C = &T_{21}(T_{12}^{'}T_{31}^{'}r_{13} + T_{11}^{'}T_{32}^{'}r_{51}) + T_{22}(T_{31}^{'}T_{22}^{'}r_{23} + T_{32}^{'}T_{21}^{'}r_{42}) \\ &+ T_{23}(T_{11}^{'}T_{12}^{'}r_{51} + T_{21}^{'}T_{22}^{'}r_{42} + T_{31}^{'}T_{32}^{'}r_{33})\end{aligned} \tag{3.21}$$

these terms depend on the Euler angles via T and $T^{'}$, and the linear electrooptic coefficients.

The sample beam which includes the scattered light $(E_{scat}^{''\omega+\Omega})_1$ and non-scattered one E_S^{ω}, are recombined with the reference beam E_{ref}^{ω} at the photodiodes. The intensity of the interfering light (the detected signal) which is detected by the photodiodes is then:

$$\begin{aligned} I &= |E_{ref}^{\omega} + E_S^{\omega} + (E_{scat}^{''\omega+\Omega})_1|^2 \\ &= I_{ref} + I_S + I_{scat} + 2\mathrm{Re}\left[(E_{ref}^{\omega} + E_S^{\omega})^*.(E_{scat}^{''\omega+\Omega})_1\right] \end{aligned} \tag{3.22}$$

where I_{ref}, I_S, and I_{scat} are the intensity of the reference, sample, and linear electrooptic scattered beams respectively.

By the way of synchronous detection, we single-out the time modulated part at the Ω modulated frequency. Leading to:

$$I_{\text{signal}} = 2\mathrm{Re}\left[(E_{ref}^{\omega} + E_S^{\omega})^*.(E_{scat}^{''\omega+\Omega})_1\right] \tag{3.23}$$

As the phase difference between the sample and reference beam is locked at $\pi/2$ and using $(E_{scat}^{''\omega+\Omega})_1$ from expression 3.18 into 3.23 we get:

$$I_{\text{signal}} \propto -(A\cos^2\alpha + B\sin\alpha\cos\alpha + C\sin^2\alpha)E_0^{\Omega}\cos(\Omega t + \varphi_E) \tag{3.24}$$

A lock-in amplifier allows to detect the electrooptic signal including its amplitude and phase as in expression 3.24.

Since the size of the nano-crystal is smaller than that of the focusing spot of the sample beam, the intensity of the electrooptic scattered light will be proportional to the volume of the nano-crystal. From expression 3.24 we can see that the intensity of the electrooptic signal depends on the orientation of the nano-crystal and is also proportional to the amplitude of the external electric field which should correspond to a linear dependence of the signal with respect to the applied voltage. The polarization response can be obtained by following the amplitude of the response $I_0(\alpha)$ with respect to the angle α when it turns from 0° to 360°, according to.

$$I_0(\alpha) \propto |(A\cos^2\alpha + B\sin\alpha\cos\alpha + C\sin^2\alpha)E_0| \tag{3.25}$$

In expression 3.25, the factor $A\cos^2\alpha + B\sin\alpha\cos\alpha + C\sin^2\alpha$ meets two maxima and two minima when α varies from 0° to 360°. Since the amplitude of the signal $I_0(\alpha)$ is the absolute value of that expression, consequently the intensity polarization response exhibits two lobes as in Fig. 3.6a if that expression does not change sign when α varies, or four lobes as in Fig. 3.6b if there is a sign change in this interval.

Expression 3.24 can be rewritten as:

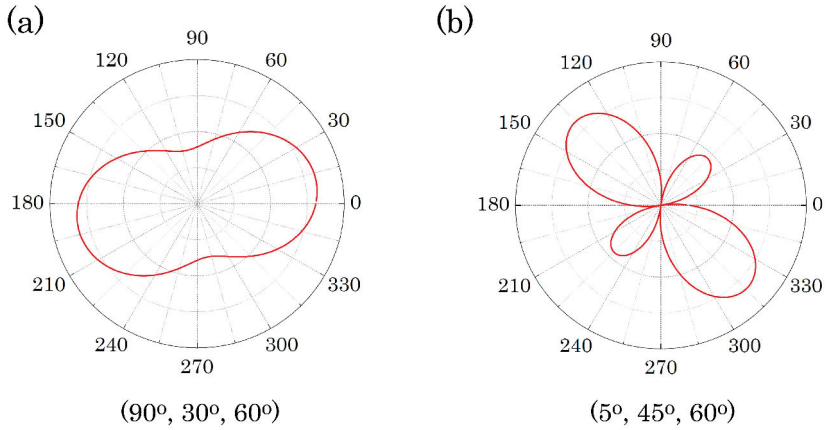

FIGURE 3.6: The calculated polarization plots (red lines) of the linear electrooptic response for two KTP nano-crystals with their orientations defined by Euler angles (90°, 30°, 60°) (a) and (5°, 45°, 60°) (b).

$$I_{\text{signal}} = I_0(\alpha)\cos(\Omega t + \varphi_{signal}) \tag{3.26}$$

where φ_{signal} can be taken as φ_E when the sign of the expression $A\cos^2\alpha + B\sin\alpha\cos\alpha + C\sin^2\alpha$ is negative or $(\varphi_E - \pi)$ when the sign of this expression is positive. The origin of the sign of this expression must be traced to the specific orientation of nano-crystal via the sign of A, B and C constants, and the polarization of the sample beam via the α value.

Considering that the external quasi-static electric field is generated by electrodes connected to a voltage generator, the external electric field as in expression 3.8 derives from the voltage

$$U = U_0\cos(\Omega t + \varphi_E) \tag{3.27}$$

The modulated frequency Ω can be controlled and the initial phase φ_E can be defined. Therefore, the phase of signal also provides information of the orientation of a single nano-crystal.

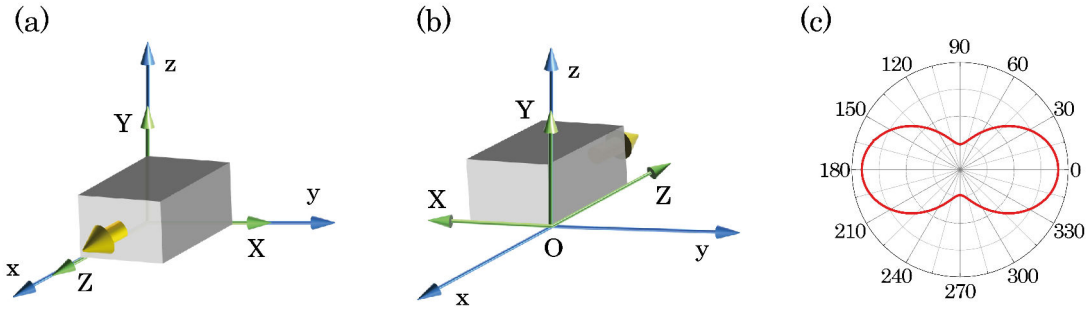

Figure 3.7: Two opposite KTP nano-crystals with Euler angles are (90°, 90°, 0) (a) and (90°, −90°, 0). (c) The intensity polarization of the linear electrooptic response for two cases in Figs. a and b.

Application this theoretical calculation for two single KTP nano-crystals with their orientations shown in Figs. 3.7a and 3.7b which could not be distinguished by using second-harmonic generation microscopy, we have:

$$I_{\text{signal}}^{(a)} \propto (r_{33}\cos^2\alpha + r_{13}\sin^2\alpha)\cos(\Omega t + \varphi_E - \pi) \tag{3.28}$$

$$I_{\text{signal}}^{(b)} \propto (r_{33}\cos^2\alpha + r_{13}\sin^2\alpha)\cos(\Omega t + \varphi_E) \tag{3.29}$$

From Expressions 3.28 and 3.29, we observe that two KTP nano-crystals with opposite orientations exhibit the same polarization amplitude as shown in Fig. 3.7c. This means that the linear electrooptic polarization response does not provide sufficient information fully the orientation of a single nano-crystal. A similar drawback can be noted with other methods [3, 55–57, 62]. However, the phase responses are opposite which can be determined by a lock-in amplifier. In general case, two KTP nano-crystals with opposite orientations exhibit the same electrooptic polarization responses but opposite phases. Therefore, we need to use both the intensity polarization and the phase of the electrooptic response of each nano-crystal to determine its full orientation.

3.4 Sample preparation

3.4.1 Electrode preparation

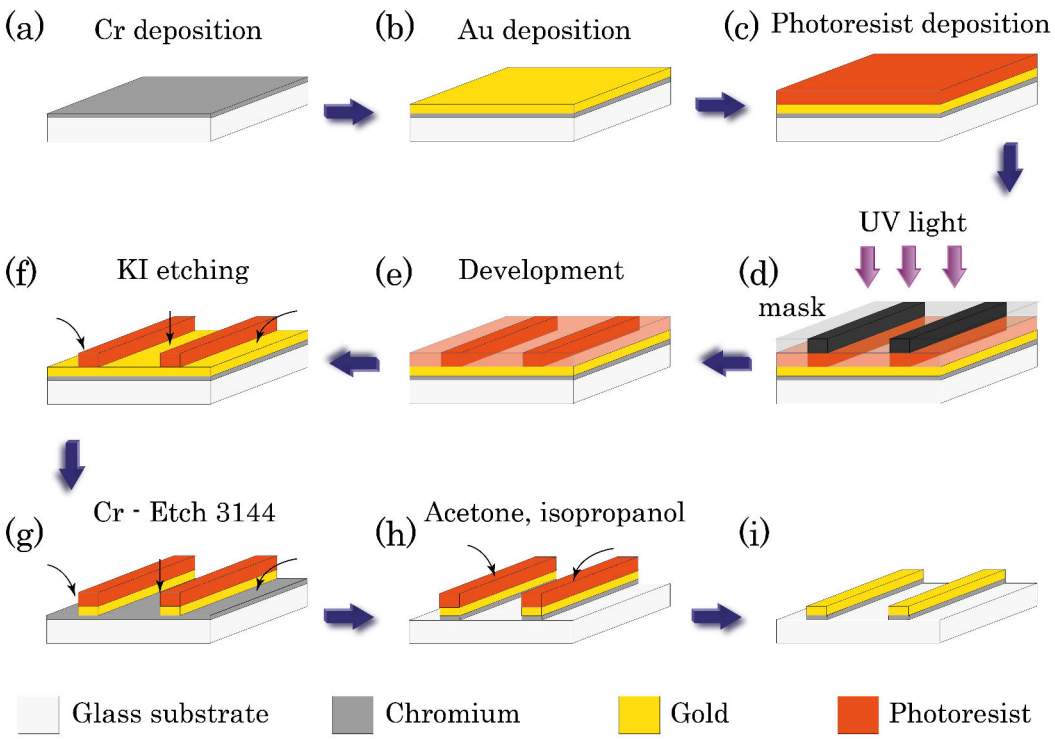

FIGURE 3.8: Different photo-lithography steps towards the fabrication of flat gold ribbon electrodes.

In our experiments, we used flat gold ribbon electrodes deposited on a 170 µm thick glass substrate as shown in Fig. 3.8i so as to generate the external electric field by connecting to a generator. The electrodes were fabricated by vacuum evaporation and soft photo-lithography techniques. The fabrication process comprises eight steps as detailed in Fig. 3.8. In the first step, a vacuum chamber is used to deposit a 10 nm thick chromium layer as the adhesion layer on a glass substrate for a 50 nm thick gold layer deposited in the second step. In the next step, a thin photoresist layer is spin coated on top of the gold layer at a the speed of 2000 rpm and acceleration of 500 rpm/s during 40 seconds. The system was put on the oven plate at 115 °C

for 1 minute in order to dry the photoresist layer. A chromium mask featuring the shape of the electrode system is exposed to UV light during 5 seconds. The part of the photoresist layer which is exposed to the UV light is developed during 1 minute by using a proper solvent, which finally unveils the part of the gold layer deprived of the protection of the photoresist. After that, the system was put inside a potassium iodine (KI) solution during 30 seconds to remove the non-protected part of the gold layer. The opened chromium layer was developed by using a Chrom-Etch 3144 solution for 1 minute. The remaining photoresist was totally removed by a 5 minute rinsing by acetone and isopropanol as the last step. The process leads to an electrode system with 70 µm wide and 50 nm thick flat gold ribbon electrodes. The length of each gold electrode is much larger than its width and the distance between two electrodes various from 10 µm to 100 µm according to application requirements.

3.4.2 Sample preparation

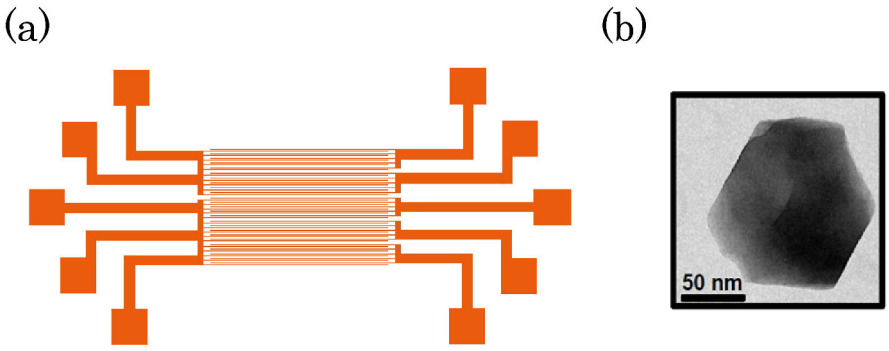

Figure 3.9: (a) Flat gold ribbon electrodes on a glass substrate and (b) TEM image of a typical KTP nano-crystal.

The flat gold ribbon electrodes were connected to an external electric power generator by conductive wires by using a conductive glue as in Fig. 3.9a. A quasi-static electric field is generated in-between two gold electrodes by application of a sinusoidal voltage from the generator.

A solution containing KTP nano-crystals (with an average size of 150 nm) as

synthesized by Mayer et all [58] and shown in Fig. 3.9b was spread and evaporated on top of the glass substrate on the side of the gold ribbon electrodes. Due to the small size of nano-particles, all KTP nano-crystals sense a spatially uniform electric field. Using a three axis piezo electric stage, a two dimensional scan of the amplitude and phase of the electrooptic signal has been performed.

3.5 Results and discussion

We applied PLEOM to the detection of KTP nano-crystals as nano-scale probes. The amplitude and the phase of the electrooptic response from single random KTP nano-crystals were measured as discussed above. The quasi-static electric field was generated in-between the two flat gold ribbon electrodes as described in section 3.4.1 at a modulated frequency of 20 kHz. By converting the optical signal into a voltage signal and using a lock-in amplifier to detect the latter, the amplitude of the signal is measured in Volt units whereas the phase of signal is the difference between the phase of signal and that of the lock-in internal reference as described in expression 2.75.

3.5.1 Simulated external electric field

In this study, we have scanned the zone in-between two gold electrode separated by a distance of 20 µm as in Fig. 3.10a. Since the length of the electrodes is much longer than their width, the y component of the external electric field is zero by symmetry. These two non-zero components of external electric field are then along x and z. The distribution of the external electric field is simulated by using COMSOL software (version 4.2). In this case, the software was used to simulate the static electric field distribution generated by the electrodes under the application of a 150 V DC voltage. Fig. 3.10b shows the 2D map of the electric field distribution around two gold electrodes in the xz plane. The direction of electric field vector is shown by dark red arrows and its amplitude by a colour code. As expected, the

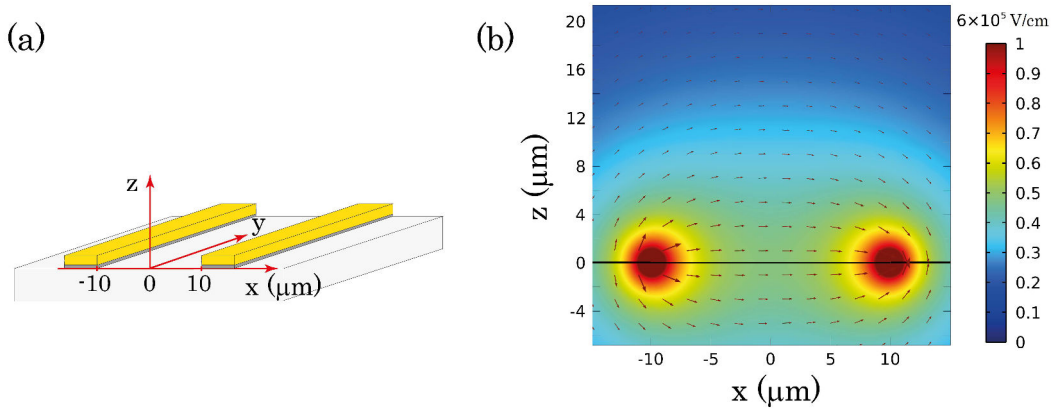

Figure 3.10: (a) Configuration of the pair of flat gold ribbon electrodes on a glass substrate (in the laboratory frame $Oxyz$). (b) 2D map of the electric field distribution in the presence of two gold electrodes in xz plane. The direction of the electric field vector is shown by dark red arrows and its amplitude follows a colour code. The electrodes themselves are not visible due to their small thickness but their edges can be recognized due to the stronger electric field at these positions (dark red colour).

electric field peaks strongly near the electrode edges (shown by the dark red color) where the free electron density is accumulated.

Fig. 3.11 shows the distribution of the x and z components of the external electric field in-between two electrodes at the same level as the KTP nano-crystals (100 nm above the top glass surface). The results confirm the strong value of the electric field components in the vicinity of the gold electrodes and the rapid decay of the electric field when going further away from the electrode edges. In the portion far from the edges of electrode edges, the z electric field component can be neglected. So that the electric field is mainly along the x axis with a value around 5.10^4 V/cm. Due to their small size, all KTP nano-crystals sense a spatially uniform electric field, which is consistent with our assumptions when performing the theoretical calculation on section 3.3.

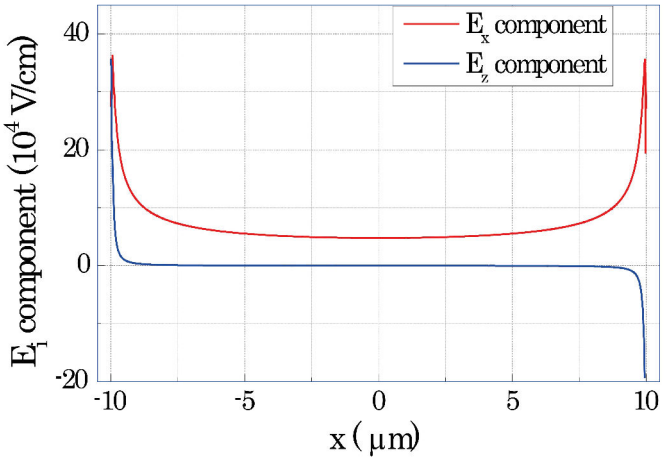

FIGURE 3.11: Profile of the E_x and E_z components as functions of x position at 100 nm above the top glass surface which is at the same height as the middle of the KTP nano-crystals.

3.5.2 Experimental results

Fig. 3.12 shows the result of a typical scan in a tiny area of 3.2×3.2 μm^2 in-between two flat gold electrodes. The linear electro-optical response appears as a bright spot in this area. The size of this spot is diffraction limit for a microscope objective at 632.8 nm wavelength as given by expression 2.1.

The cross sectional lines along x at $y = 29.81$ μm and along y at $x = 36.76$ μm yield the profiles of the observed signal spot for a single KTP nano-crystal along two orthogonal projections. These profiles shown as red lines in Fig. 3.12 were fitted by using Gaussian functions, giving values 720 nm and 650 nm for the full width at half maximum (FWHM) in the x and y directions respectively. These results are consistent with that from other microscopes when working on single nanoparticles with dimensions smaller than the wavelength of light [55, 58, 62]. The main reason of the different size of the signal spot along the two directions originates from the irregular geometry of the KTP nano-crystals as shown in Fig. 3.9b. The colloidal synthesis of our KTP nano-crystals give a size distribution of 150±50 nm. Therefore the size of the nano-crystals, is comparable with the wavelength of the excitation

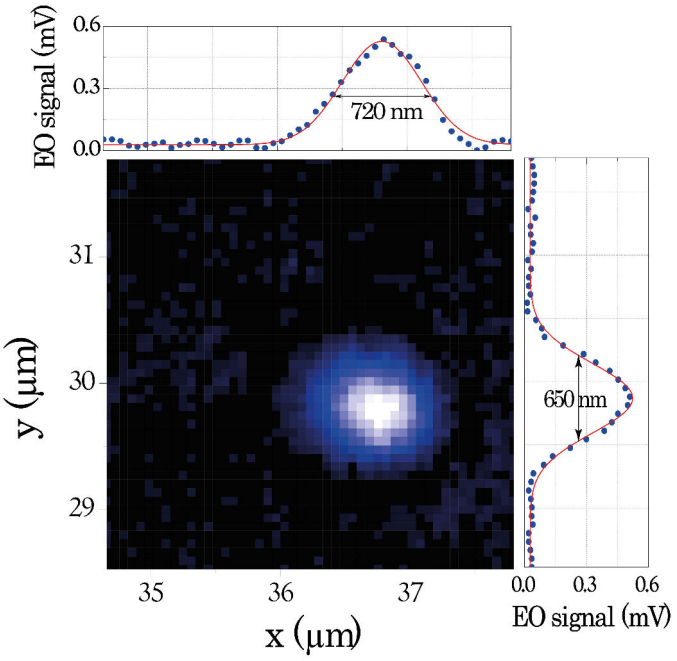

Figure 3.12: Spatial electrooptic amplitude response from a single KTP nano-crystal and profile lines along x and y going through the center of the signal spot; the red lines are the fitted Gaussians.

light. Thus, the FWHM of the signal spots for the KTP nano-crystals is expected to fall in the range from 600 nm to 800 nm. Taking into account the high sensitivity and high dynamic range of our microscope, PLEOM is able to perform measurements of KTP nano-crystals of smaller sizes. In that case, each nano-crystal can be considered as a point and the response profile can then be fitted with an isotropic Gaussian function.

The background noise calculated from the entire area without the signal spot as in Fig. 3.12 was 0.022 mV. The main sources of the background noise are from the detectors (dark noise) and the electronics noise. This value for the background noise can thus be taken as the standard deviation of our PLEOM measurement performed. If we define the amplitude of the linear electrooptic signal for each detected nano-crystal as the maximum value of the corresponding fitted Gaussian function, the amplitude of the signal of the KTP nano-crystal in Fig. 3.12 is 0.498 mV. Therefore, the signal to noise ratio for this measurement is of the order of 24 which allows for

high contrast measurement. The high signal-to-noise ratio and dynamic range in detection of PLEOM allows to detect ferroelectric nano-crystals at smaller sizes, in particular other ferroelectric nano-crystals with high linear electrooptic coefficients such as Barium titanate ($BaTiO_3$) or Strontium barium niobate ($Sr_{0.6}Ba_{0.4}NbO_6$) [41].

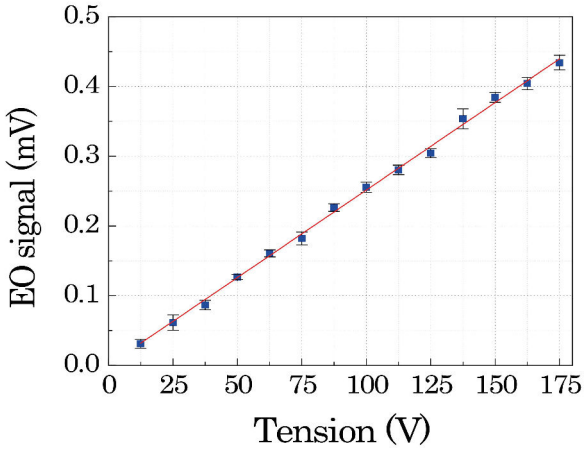

FIGURE 3.13: Linear dependence of the signal with respect to the applied voltage amplitude.

A characteristic signature of the Pockels effect is the linear dependence of the linear electrooptic response versus the amplitude of the external electric field, which provides strong evidence that the measured signal from a KTP nano-crystal originates from the Pockels effect as in Fig. 3.13.

Performing the other scan throughout a larger area, six KTP nano-crystals were identified and labelled as in Fig. 3.14a. The orientation and volume of each nano-crystal are different as discussed which leads to different amplitudes and phase responses according to expression 3.25. Indeed, the intensities of the linear electrooptic response of the six nanoparticle are different as in Fig. 3.14a. From the phase image (Fig 3.14b), it is clear that in the area without the expected signal spots, the phase has a random value which is that of the background noise. At the positions of signal spots, the phases have the same value as shown by dark and bright spots because

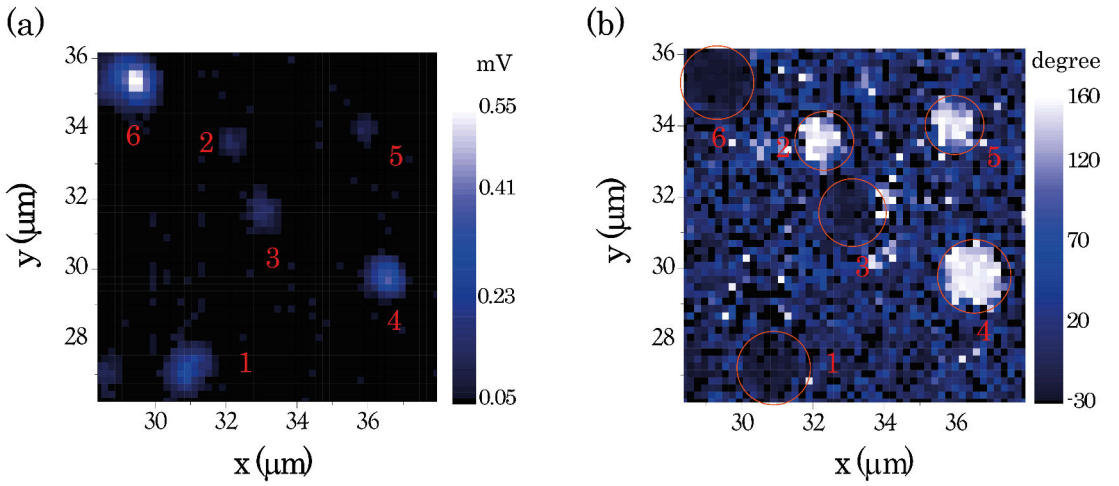

Figure 3.14: Spatial electrooptic response over a large area. (a) Amplitude and (b) phase image of the detected signal.

of the phase of electrooptic signal for each nano-crystal.

For more detail, the cross-sectional lines along y that pass through the signal spots on the signal phase image were plotted in Fig. 3.15. It is clear that the phases of the signal for nano-crystals 1, 3 and 6 are quasi identical with a value around -30° and opposite to that of nano-crystals 2 and 4 (and the same for nano-crystal 5 as in Fig. 3.14b) with the values around 150°. As in expression 3.26 from the theoretical part, the phase of the signal is the same or opposite to that of the applied voltage. It also depends on both the orientation of the nano-crystal and the polarization of the incident light. Comparing with the phase value of the applied voltage from the generator, we can infer the sign of the expression inside the absolute value symbol in expression 3.25 for each KTP nano-crystal. For this measurement, the phase of applied voltage is -30° which was measured by the lock-in amplifier in the same experimental conditions (this phase value is exactly the difference between the phase of applied voltage and that of the lock-in interference signal. But the phase of the lock-in interference signal did not change during the experiment process allowing us to give a zero value). The sign of the expression inside the absolute value symbol in expression 3.25 applied to the particles 1, 3 and 6 is therefore negative and positive

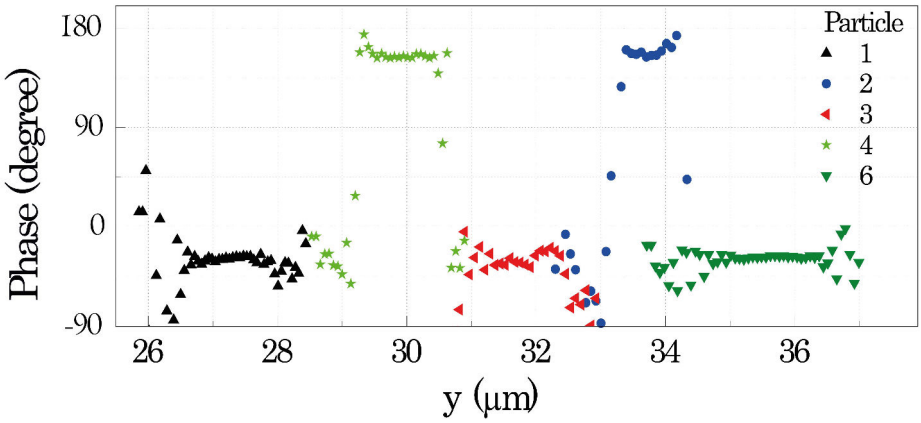

FIGURE 3.15: Phase of the electrooptic signal of five KTP nanocrystals measured by the lock-in amplifier, drawn along the vertical lines and passing through signal spots in Fig. 3.14b. With different particles, the phases have two values respectively around: -30° and 150°.

for particles 2, 4 and 5.

Very much like in other nonlinear microscopies where the nonlinear optical response depends strongly on the polarization of the excited beam and the orientation of the nonlinear material, the intensity of the electrooptic scattering response from a ferroelectric nano-crystal strongly depends on the polarization of the sample beam (the α value) and the orientation of crystal (A, B, and C constants which relate to the orientation of the nano-crystals through Euler angles) as in expression 3.25. By rotating the polarization angle α from 0° to 360°, we obtain the intensity polarization responses for nano-particles 1, 4, and 6 as shown in Fig. 3.16. While providing the best configuration for the incident beam polarization that leads to the highest nonlinear optical response, it also leads to the orientation of nonlinear nano-crystals. However, PLEOM differs from other methods [53, 55–58, 62, 92, 93, 97] which make use of the detectors to count the emitted nonlinear photons by the samples, and therefore measure the absolute value of the nonlinear response with respect to α value as in expression 3.25. In such condition, the intensity polarization response can only lead to the axial orientation of a nano-crystal, and not to its full vectorial orientation. From intensity polarization responses of the three nano-crystals as in

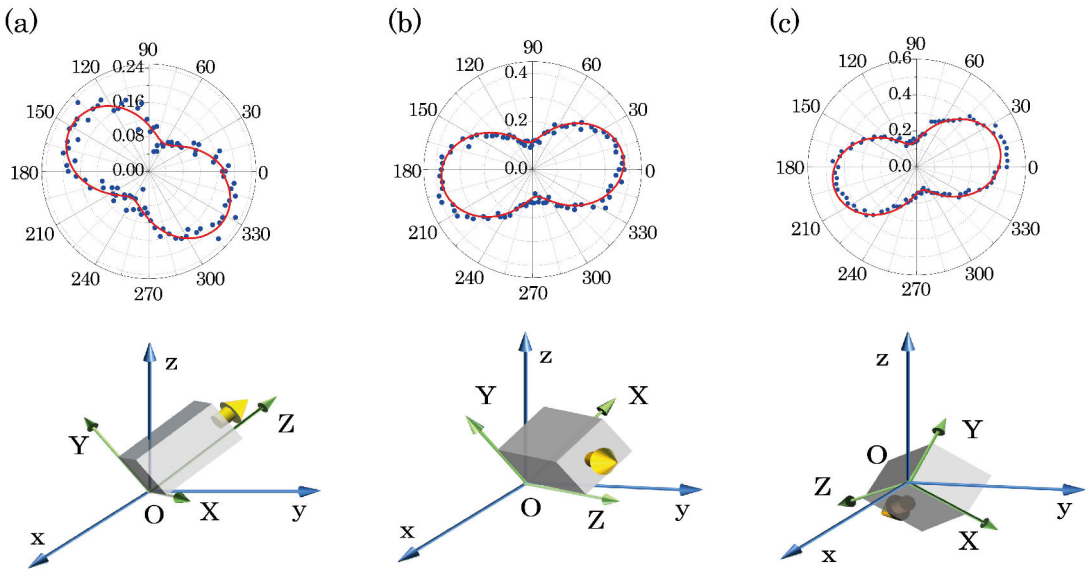

Figure 3.16: Linear electrooptic polarization responses of three KTP nano-crystals with different orientations. (a) particle 1; (b) particle 4; and (c) particle 6 as labelled in Fig. 3.14. The blue dots are the experiment data and the red lines are the fitted curves. The corresponding crystal 3D orientation is presented below each polar graph.

Fig. 3.16 and by performing a fit of expression 3.25, the respective orientations described by the Euler angles for particles 1, 4, and 6 are (43°, 138°, 49°) or (43°, -42°, -49°), (95°, 75°, 28°) or (95°, -105°, -28°), and (107°, 72°, 19°) or (107°, -108°, -19°) respectively in which two options for the orientation of each nano-crystal are found opposite to each other. Unlike other methods, PLEOM measures the phase of the electrooptic response which provides the missing needed information to fully determine the orientation of each nano-crystal. The intensity polarization responses of nano-particle 1, 4, and 6, exhibit only two lobes. Implying that the expression inside the absolute value symbol in the expression 3.25 applied for those particle does not change sign with variation of α. Therefore the Euler angles describing the orientations of these nano-crystals are (43°, -42°, -49°), (95°, 75°, 28°), and (107°, -108°, -19°) corresponding respectively to crystal 3D orientations which are presented below each polar graph in Fig. 3.16.

In cases where the sign of the linear electrooptic intensity of scattered by a KTP nano-crystal changes with the orientation of the polarization axis of the sample

beam, the response will exhibit four lobes as in Figs. 3.6b and 3.17a. Such change

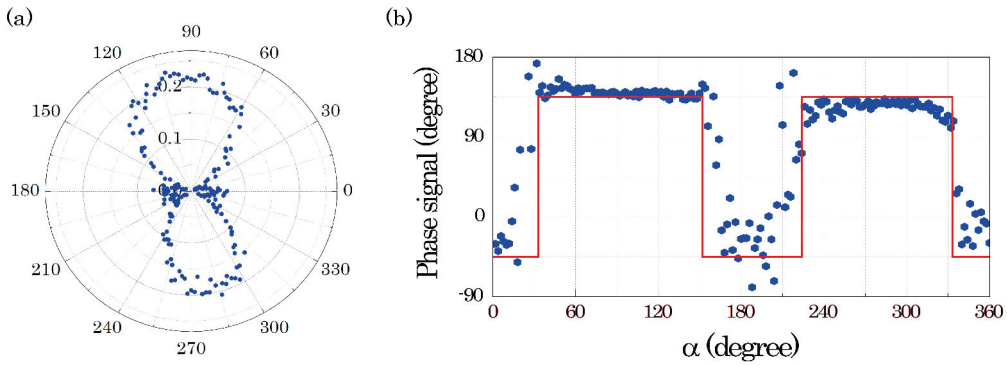

FIGURE 3.17: (a) Intensity polarization response with four lobes for a KTP nano-crystal and (b) phase value of the linear electrooptic signal of this particle with respect to the polarization angle α of the sample beam.

of sign can be observed through a π shift of the phase signal as in Fig. 3.17b. In this case, KTP nano-crystals are oriented so that the intensity of their electrooptic response expression 3.25 is smaller than for other cases. For example, as in Fig. 3.17a, the highest intensity of the electrooptic signal is around 0.22 mV. The intensity of the signal associated to the two small lobes is very weak of the order of the background noise. This leads to a phase signal with a the random value as in Fig. 3.17b. The result in Fig. 3.17 is consistent with our model and the full orientation of this KTP nano-crystal can be extracted as for the other cases by using the polarization response and phase image.

3.5.3 Study of randomly oriented KTP nano-crystals by using the reflection configuration of PLEOM

As described in the section 2.5.3, another configuration for PLEOM was set-up in order to investigate the linear electrooptic surface scattering of samples or non-transparent samples.

In order to validate the new configuration of PLEOM work, it was tested with 150 nm KTP nano-crystals. In this case, our theoretical model of the linear electrooptic

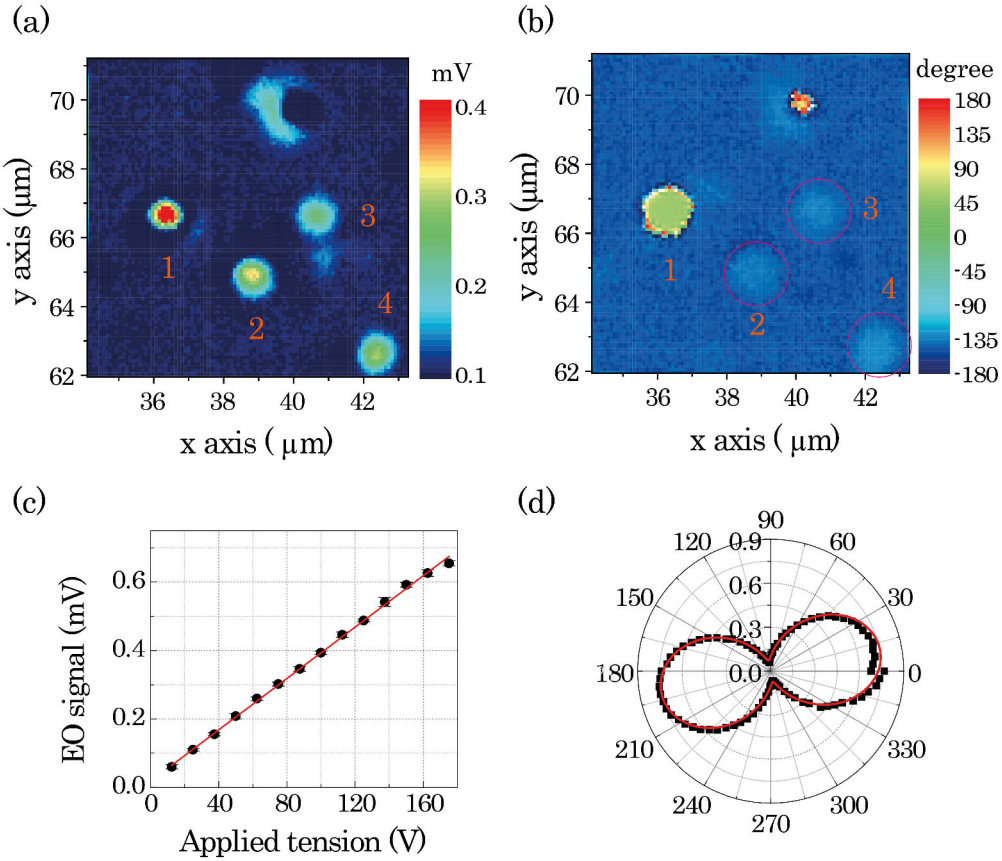

Figure 3.18: Spatial linear electrooptic response from KTP nano-crystals over a large area; (a) amplitude image and (b) phase image. (c) Linear dependence of the signal with respect to an applied electric field amplitude and (d) polarization response corresponding to orientation defined by Euler angles (ψ = 143°, θ = -15°, σ = -40°). The continuous lines in red are fitted from experimental points

scattering from them was fully satisfied by experimental results obtained when using the previous configuration of PLEOM.

Fig 3.18a shows the spatial electrooptic response from KTP nano-crystals when using the new PLEOM and performing a scan over large areas. The linear electrooptic signal spots exhibit Gaussian profiles with similar size to that of the focused spot of the sample beam. The phases of the signal have only two values which are the same or opposite to that of the applied voltage as in Fig. 3.18b. The linear dependence of the signal with respect to the applied electric field amplitude and the polarization response were measured and displayed in Figs. 3.18c and 3.18d. All

properties inferred therefore are in agreement with their counterpart as from the previous PLEOM configuration. The new PLEOM configuration can therefore expand the range of investigation of the linear electrooptic properties of nonlinear materials.

3.6 Conclusion

From the previous raw theoretical calculation about the linear electro-optical scattering from a single random KTP nano-crystal initiated by Hajj et all [3, 67], we developed a full theoretical analysis which was fully confirmed by the experimental results and can be applied to any ferroelectric nano-crystal.

The electrooptic Pockels scattering from a single ferroelectric KTP nano-crystal was measured by PLEOM. We demonstrated for the first time that the orientation and especially the vectorial features of the electric polar moment of a single random ferroelectric nano-crystal could be precisely extracted from the polarization state and the phase of its Pockels response. These results validate the capacity of PLEOM to be applied for 3D imaging by way of using ferroelectric nanoparticles as nano-scale probes. Such nanoparticles are nanoprobes to find an application in electric field probing within different domains such as electronics or biology.

The high signal to noise ratio and high dynamic range in detection allowed by PLEOM suggest the possibility to detect nonlinear nanoparticles with even smaller size, and consequently to propose more convenient (less invasive) probes for biological applications especially when using nonlinear materials with high linear electrooptic coefficients such as Barium titanate ($BaTiO_3$) or Strontium barium niobate ($Sr_{0.6}Ba_{0.4}NbO_6$) [41]. PLEOM also leads itself to studies of one or two dimensional periodically or randomly poled structures for quasi phase matched devices.

4

Electro-optical interferometric microscopy of periodic ferroelectric structures

Alongside the full determination of the spontaneous polarization of a single random ferroelectric nano-crystal as presented in the previous chapter, PLEOM can be developed into a new sub-wavelength microscopy for imaging patterns and checking the quality of one-, two- and three-dimensional quasi-phase matched crystalline structures from micro to macroscopic scale. Following this direction, we present in this chapter a non-invasive method towards the characterization of the ferroelectric domain structure of a 1D periodically poled $KTiOPO_4$ crystal by interferometric measurements of the electrooptically induced phase retardation. A characteristic π phase shift of the linear electrooptic response is observed in relation with the sign reversal of the electrooptic coefficients the domain inversion. PLEOM provides a

diffraction limited spatial resolution allowing to reveal the nonlinear and electrooptic modulation patterns in ferroelectric crystals in a non-destructive manner, to determine the poling period and duty cycle, and to detect local defects in the domain structure. The related domain characterization can only be achieved by an interferometric technique and is not within the reach of intensity defendant microscopic techniques such as second-harmonic generation which is not sensitive to domain reversal.

4.1 Introduction

In recent years, ferroelectric materials have become popular objects in physical research in view of their applications in nonlinear optics and data storage. For a long time, since 1921 when the first ferroelectric material (Rochelle salt, $NaKC_4H_4O_6.4H_2O$) was reported by J. Valasek [108], the group of ferroelectric material has been extended to $\sim$ 250 pure materials and many more mixed crystal compounds [109]. Although they carry a long history of fundamental investigations all the way to applications, ferroelectric materials are intensively investigated to this day. Indeed, this ongoing interest is driven by a lack of basic understanding of ferroelectricity while their applications still require optimization of such features as shape, quality, tailoring and control of their domain structure, etc.

Besides the application of ferroelectric materials in high density data storage devices [110, 111] or electrically controlled Fresnel zone plate [112], among the most interesting application of these materials is optical frequency conversion in which the second order susceptibility $\chi^{(2)}$ is spatially modulated while the linear susceptibility remains constant, as exemplified in periodically poled crystals. Nonlinear processes in the periodically poled crystals are governed by phase matching conditions, which has lead to call them quasi-phase matched crystals. Although the theoretical prediction for such structures had been proposed as early as in 1962 by Armstrong et al [10], it took nearly thirty years to implement this concept when the periodic poling of $LiNbO_3$ became possible [11, 113, 114] and hence enabled

the broad development of periodically poled crystals [115–127] even in the shape of nonlinear photonic crystals with 2D spatial modulation of $\chi^{(2)}$ [40, 128, 129]. One also refers frequently in this context, by analogy with X-ray diffraction, to one- and two-dimensional optical Bragg structures. Modulation of the nonlinear coefficient in ferroelectric crystals can be achieved by using the electric field poling method [40, 114, 130] and can be grown to be a larger size from a periodically poled seed by the flux method [131, 132]. The principle of the electric field poling method is derived by the properties of the spontaneous polarization $\overrightarrow{P}$ of a ferroelectric crystal which can be reversed under the application of an external electric field with opposite direction along the axis of polarization , with the additional condition that its value exceeds that of the coercive field E_c of this material. Domain inversion reverses the sign of all non-zero elements of odd rank tensors attached to this material, including the second-order nonlinear tensor and the Pockels electrooptic tensor [122], but has no effect on even order tensors such as the refractive index of the crystal. The conversion efficiency of the nonlinear process strongly depends on the features and quality of the quasi-phase matched crystals such as precisely defined poling period and duty cycle or the presence of local defects in its domain structure.

For a better understanding of ferroelectric materials and control of the encoded or poled domain structures, a visualization of the ferroelectric domains allowing for sensitive detection of defects in each domain is in high demand. Various methods have thus been proposed in order to characterize domains structures and detect defective domains in ferroelectric crystals. Firstly, methods which rely on the different surface properties between normal and inverted domains were developed. As a consequence of ferroelectricity, the surfaces of crystals which are perpendicular to the spontaneous polarization vector are charged. Normally, those surface are expected to be compensated. However, the remaining electrostatic field at those surfaces is still strong enough due to incomplete charge compensation. It allows for detection methods based on the interaction between the charged crystal surface and charged particles or spontaneous polar particles and molecules. In this perspective,

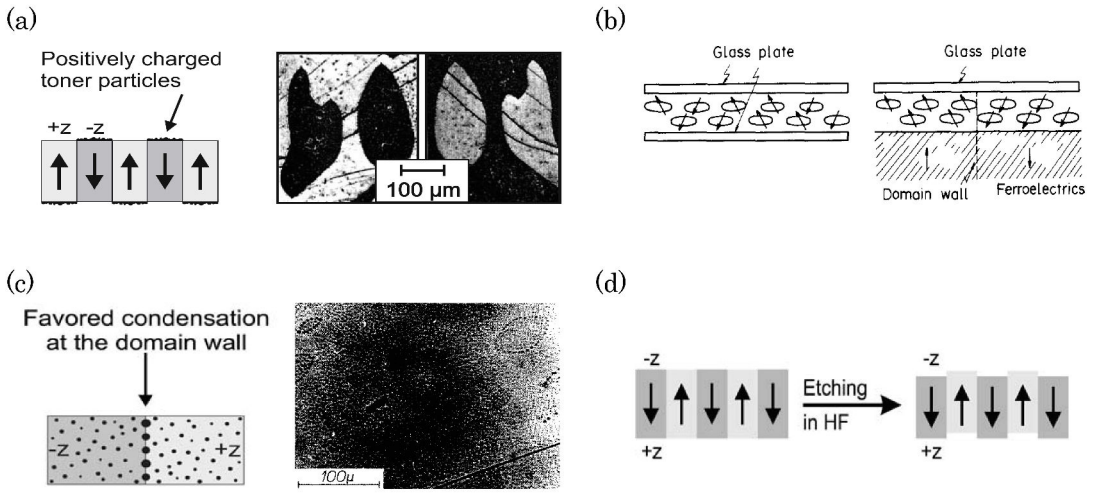

FIGURE 4.1: (a) Schematic of toner decoration at the surface of ferroelectric crystals [109]; (b) Molecular orientation of nematic liguid crystal layered in-between a glass plate and a ferroelectric crystal allowing to image its domain structure [133]; (c) Lenticular domains in a TGS crystal made visible by the dew method using isobutyl alcohol vapor condensation [109, 134]; and (d) selective etching for the visualization of antiparallel ferroelectric domains in z-cut, where the -z face etches much faster in hydrofluoric acid than the $+z$ face [109].

several surface decoration methods have been developed such as the powder/toner pattern techniques [135, 136] shown in Fig. 4.1a, the liquid crystal imaging method [133, 137] in Fig. 4.1b, and the dew method [134] as in Fig. 4.1c. The most common method for the visualization of ferroelectric domains is selective etching based on the different etching speed at the upper and lower surfaces of a single domain as shown in Fig. 4.1d [138–140]. However, surface etching is a destructive method. Moreover , all those surface-modifying techniques can only yield two-dimensional images of the domain structure at the surface whereas internal information inside the bulk of each domain can not be reached.

In order to improve the resolution of the ferroelectric domains images, other electron diffraction or transmission based methods are available such as scanning electron microscopy (SEM) which is base on the different electrostatic interactions of an electron beam with positively versus negatively charged surfaces at the boundaries of a domain sustaining a net polarization dipole [141–143], scanning electron

acoustic microscopy (SEAM) [144, 145], transmission electron microscopy (TEM) [146–148] which can only be applied to ultra thin ferroelectric films, scanning force microscopy (SFM) (or piezoelectric force microscopy mode (PFM)) [149–153], and scanning-tip microwave near-field microscope [154]. However, all these methods provide only a surface topography of ferroelectric materials without direct internal informations.

In order to provide information on the internal ferroelectric domain in a non-destructive manner, optical methods are appealing candidates due to the penetration ability of light. Optical methods also promise the advantage of being non-contact and non-invasive, and may also enable the real time monitoring of the domain-formation process by in-situ measurements. Bhide and Bapat used a multiple beam interferometric technique to study the surface microtopography arising from the 90° domain walls in $BaTiO_3$ single crystals in the ferroelectric tetragonal phase [155]. Alternative techniques that have also been demonstrated are X-ray imaging [156–158], photorefractive beam coupling method [159], and the second harmonic generation method [160–163] as in Fig. 4.2, or phase-sensitive second-harmonic microscopy method performed by Hulliger's group [164]. The most useful property of ferroelectric materials in order to optically visualize ferroelectric domains is their brief-in linear response of the refractive index to an externally applied voltage (Pockels effect) with the first demonstration in 1944 by Zwicker and Scherrer [165]. Following the same principle, numerous methods based on the Pockels effect were proposed and demonstrated such as polarization microscopy [109, 166], light deflection [167–169], photorefractive grating/beam-coupling [170, 171], electro-optic interferometry [172, 173]. However, all those demonstrations are plagued by their poor resolution.

More recently, use of attempts above 10 μm were achieved to overcome the limitation of those optical methods by use of a scanning confocal microscopy and scanning near-field microscopy. Among these, Čerenkov second-harmonic generation method [68–71] were stands-out: it is based on Čerenkov-type second-harmonic generation along the domain wall of ferroelectric materials [174]. This method provides high 3D

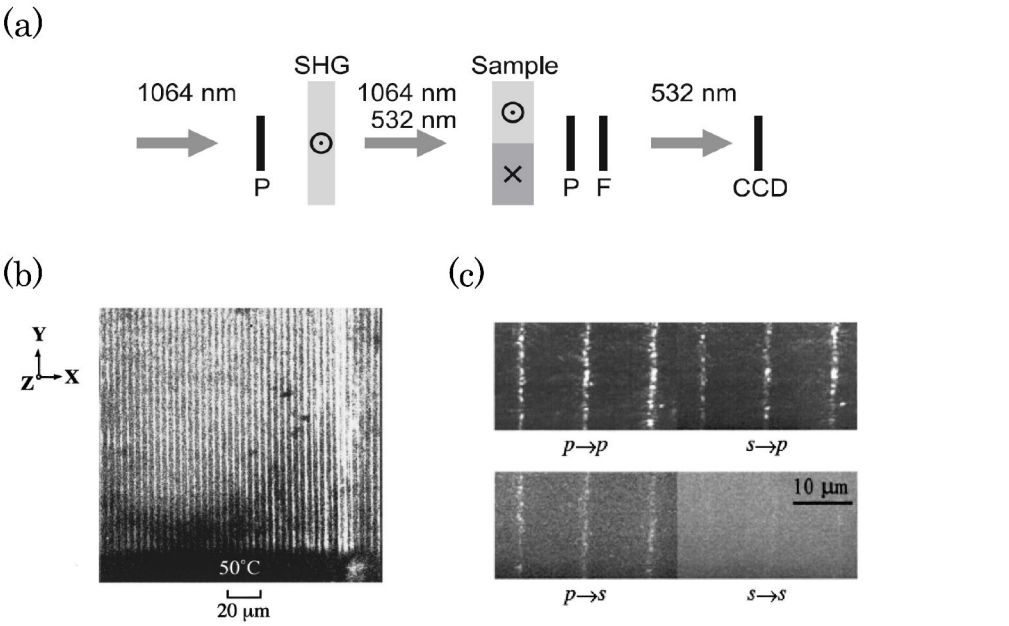

FIGURE 4.2: (a) Otical setup for a second harmonic generation microscopy. SHG: uniform second harmonic plate, P: polarizer, F: infrared absorption filter, and CCD: camera [109]. (b) SH image by d_{22} on the Z face of the Z-cut quasi-phase matching device [161]. (c) high-resolution second-harmonic images of periodically poled $LiNbO_3$ crystal showing the domain walls [160].

optical resolution of domain walls but require an intense laser beam to generate a measurable second-harmonic signal and fails to determine the full vector properties of ferroelectric domains as well as their internal structure.

Due to the working principle of the PLEOM which is based on one of the most usefull properties of ferroelectric materials namely the linear electrooptic effect (Pockels effect), and from our earlier use of PLEOM to study single ferroelectric nano-crystals (see previous chapter), we propose hereafter an alternative technique based on the linear electro-optic interference method to study the domain structure of a periodically poled ferroelectric crystal. We experimentally demonstrate the ability of this approach to characterize ferroelectric crystals containing inverted domains down to diffraction limited spatial resolution. This method allowed us to determine the poling period, duty cycle, and evidence domain defects in 1D periodically poled crystals by using a simple low power CW laser (He-Ne laser source 1.5

mW CW power).

4.2 Sample preparation

In this study, we have investigated a typical 10×2×0.5 mm^3 KTP crystal sample periodically poled by the electric field poling [40, 114] with a period of 36 μm from Tel Aviv University (under a cooperation with the research group of Prof. Ady Arie).

4.2.1 The electric field poling method to prepare a quasi-phase matched crystal

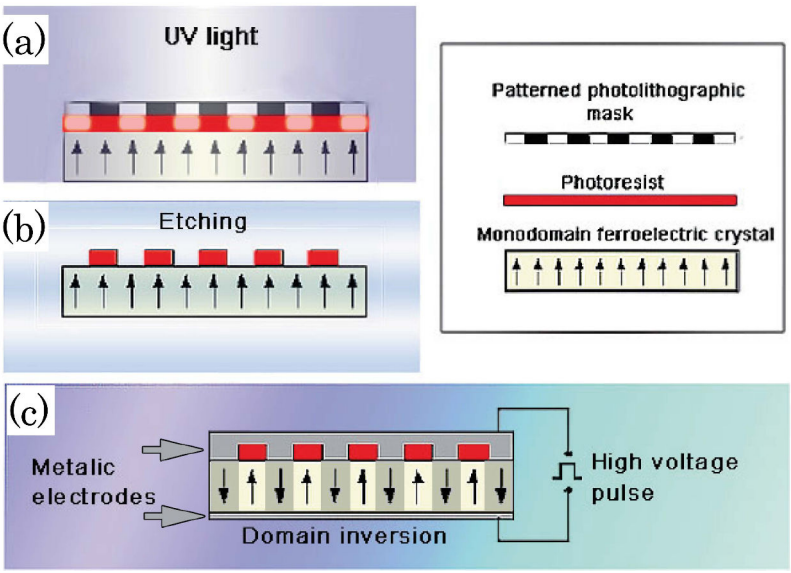

Figure 4.3: Fabrication of a periodically poled crystal by the electric field poling technique: (a) Photolithography of a photoresist-coated single domain ferroelectric crystal. (b) Etching of exposed areas in the photoresist. The top and bottom surfaces of the crystal are then coated with electrodes. (c) A high voltage pulse reverses the sign of the dielectric dipoles in areas under the top metallic ribbon electrode [40].

The periodically poled KTP crystal was prepared through a three step process as depicted in Fig. 4.3. In the first step, photolithography is used to pattern the photoresist-coated crystal. Firstly, a single KTP crystal is cleaned by using a series

of successive solvents in an ultra-sonic bath. Its top surface is then completely covered by a homogeneous thin layer of photoresist by a spin-coater. The final preparation stage is the patterning of the sample by exposing the photoresist to UV light through a well-defined mask and developing the sample in which the uncovered photoresist parts are removed as in Fig. 4.3b. The top and bottom surfaces of the crystal are then coated with metallic electrodes.

In a second step, a high voltage pulse was applied on the metallic electrodes. The poling process is thought to start at the edges of the top electrode in contact with the crystal surface where the electric field is the strongest. The inverted domain regions then grow within areas in contact with the top electrode, whereas the region under the remaining photoresist would demand a much higher voltage to be poled. The high voltage pulse thus only reversed the sign of the dielectric dipoles in areas where the top metallic electrode is in contact with the crystal. After completion of the poling process, the last step is to remove the metallic electrodes on both surfaces of the sample which are then polished before use.

4.2.2 The configuration of sample in the external electric field

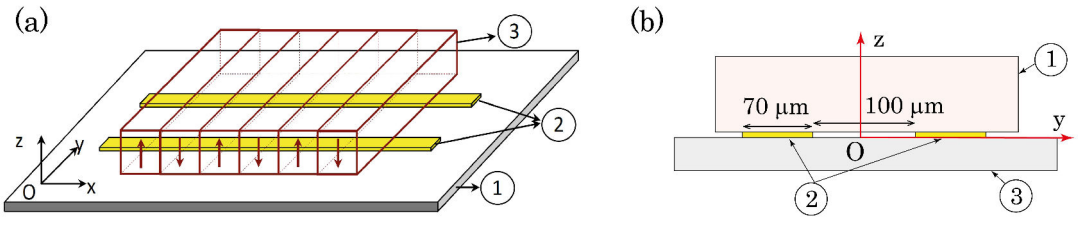

FIGURE 4.4: (a) Configuration of the periodically poled KTP crystal (1) on two flat gold ribbon electrodes (2) deposited on the glass substrate (3). (b) cross-section of the electrode system in the yz plane. The thickness of the flat gold ribbon electrodes is 50 nm and can be neglected in the electric field distribution calculation. The width of the electrodes and the gap in-between are 70 µm and 100 µm, respectively, which is very small compared to the electrode length.

In this study, the flat gold ribbon electrode system already described in Section

3.4.1 was still used to generate a quasi-static external electric field by connecting a generator as in the experiment with KTP nano-crystals. The scanned zone for PLEOM in the current experiment extends in-between the two flat gold ribbon electrodes. With this electrode system, the distance between the two ribbons varies from 10 to 100 µm. We chose here the latter interelectrode gap (100 µm) whereas the periodically poled KTP crystal was oriented so that the polarization dipole of the poled zones are along z, with domains along y as in Fig. 4.4a. In this configuration, the crystal coordinate frame coincides with that of the laboratory. The laser beam propagates perpendicular to the crystal slab along the z direction with linear polarization along the y axis.

4.3 Theoretical calculation

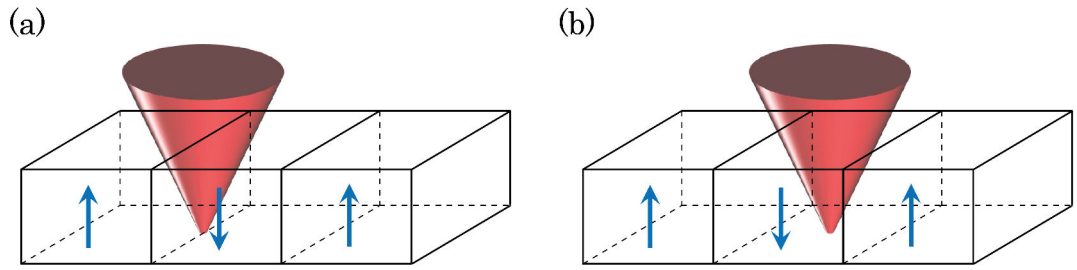

Figure 4.5: Configuration of the laser beam traveling through a periodically poled crystal along the z direction with the focused spot always on the bottom crystal surface. (a) When the focused spot is at the ferroelectric domain wall and (b) at the center of a ferroelectric domain.

In this study, the sample beam of PLEOM travels through the z direction with its linear polarization along the y axis. Due to focusing by the objective, the sample beam fills a conical volume when passing through the sample with its beam waist located on the bottom crystal surface as shown in Fig. 4.5. Each ray of the sample beam travels through an individual optical path which belongs either to a normal or inverted domain or to both of them, whereas its polarization is not maintained along the y axis. Consequently, the phase shift experienced by each ray will vary

due to the linear electrooptic dephasing under the application of an external electric field is different with each other.

Let us assume that the sample beam comprises N individual rays. The theoretical calculation steps in this case are the same as for the calculation in part 2.5.1, subject however to the introduction of variable Pockels phase shifts for different light rays. Expressions 2.51 and 2.52 defining the electric field components of the electromagnetic waves of the reference and sample beam ($\xi_r(t)$ and $\xi_s(t)$) at the photodiodes in the absence of an external electric field (which induces the Pockels effect on the sample), now take the following forms:

$$\xi_r(t) = \frac{1}{\sqrt{2}}\overline{\alpha}_r e^{i(\omega t+\phi)} \tag{4.1}$$

$$\xi_s(t) \propto \frac{1}{\sqrt{2}}\int_{\text{all rays}} \mathrm{d}\overline{\alpha}_s e^{i\omega t} \tag{4.2}$$

where $\mathrm{d}\overline{\alpha}_s$ is the amplitudes of the electric field component of a light ray. Under application on the sample of an external electric field $E_{ext}(t)$ given by:

$$E_{ext}(t) = \overline{E}_{ext}\cos(\Omega t + \phi_E) \tag{4.3}$$

the phase of the j^{th} ray going through the sample varies by an amount $\Delta\varphi_j(t)$ due to the Pockels effect:

$$\Delta\varphi_j(t) = \overline{\Delta\varphi}_j\cos(\Omega t + \phi_E) \tag{4.4}$$

where $\overline{\Delta\varphi}_j$ is the amplitude which can take a positive or negative value depending on the optical path taken by the corresponding ray through the different ferroelectric domains.

The electric field component of the sample beam at the photodiode is:

$$\xi_s(t) \propto \frac{1}{\sqrt{2}}\int_{\text{all rays}} \mathrm{d}\overline{\alpha}_s e^{i\omega t} e^{i\Delta\varphi_j(t)} \tag{4.5}$$

Whereas the expression of the electric field components for the reference beam remain the same as in expression 4.1.

The electronic signal generated by the difference of the two photocurrents achieved

by an electronic circuit as in expression 2.63 now has the form:

$$\begin{aligned}\Delta i &= 4\rho \mathrm{Re}[\xi_r(t)\xi_s(t)^*] \propto 2\rho \mathrm{Re}\left[\overline{\alpha}_r \int_{\text{all rays}} \mathrm{d}\overline{\alpha}_s e^{i(\phi-\Delta\varphi_j(t))}\right] \\ &\propto 2\rho\overline{\alpha}_r \int_{\text{all rays}} \mathrm{d}\overline{\alpha}_s \cos\left[\phi - \Delta\varphi_j(t)\right]\end{aligned} \tag{4.6}$$

As the initial phase difference between the reference and sample beams is set at the fixed value $\phi = \pi/2$ by moving the mirror placed on the piezoelectric stage. As a result, the electronic signal in expression 4.6 now becomes:

$$\Delta i \propto 2\rho\overline{\alpha}_r \int_{\text{all rays}} \mathrm{d}\overline{\alpha}_s \sin\left[\Delta\varphi_j(t)\right] \approx 2\rho\overline{\alpha}_r \int_{\text{all rays}} \mathrm{d}\overline{\alpha}_s \Delta\varphi_j(t) \tag{4.7}$$

As the phase shift induced by the Pockels effect in this case is very small (around 10^{-6} to 10^{-2} radian). Replacing the $\Delta\varphi_j(t)$ from expression 4.4 into 4.7, the expression for the electronic signal becomes:

$$\Delta i \propto 2\rho\overline{\alpha}_r \int_{\text{all rays}} \mathrm{d}\overline{\alpha}_s \overline{\Delta\varphi_j} \cos(\Omega t + \phi_E) = \overline{\Delta i}\cos(\Omega t + \phi_E) \tag{4.8}$$

Expression 4.8 has the same form as 2.65 but in this case, the amplitude of the signal originates from all rays in the illuminating cone with different phase shifts:

$$\overline{\Delta i} = 2\rho\overline{\alpha}_r \int_{\text{all rays}} \mathrm{d}\overline{\alpha}_s \overline{\Delta\varphi_j} \tag{4.9}$$

Because of the linear dependency of the Pockels phase shift $\overline{\Delta\varphi_j}$ of the j^{th} light ray with respect to the external electric field, the Pockels phase shift of the sample beam used to sense the linear electrooptic effect for this crystal depends on the distribution of the external electric field. Furthermore, due to the conical shape of the sample beam as in Fig. 4.5, when traveling through the periodically poled crystal, some rays propagate through a normal ferroelectric domain while other are going through the adjacent inverted domains and others go through two different domains. As a result, the amplitude $\overline{\Delta\varphi_j}$ of the phase shift of the j^{th} ray can be positive or negative. When the focused spot of the sample beam is shining domain wall in a symmetrical configuration as in Fig. 4.5a, one half of the sample beam travels through a domain while the other half travels through a neighbouring domain with opposite dielectric dipole. The total phase shift for each part have

equal absolute values but opposite sign, so that the phase shift for the two parts compensate each other leading to cancellation of the total phase shift. Consequently, the linear electrooptic signal goes through a minimum when the beam waist of the sample beam is located at the domain wall. For other configurations, when the beam waist of the sample beam is located at the center of a domain as in Fig. 4.5b. The main part of the sample beam travels through this domain whereas a much weaker part travels through the neighbouring domains with opposite dielectric dipole. As a result, the total phase shift of the sample beam in this case is maximum leading to a maximal linear electrooptic response. When the sample beam eventually hits a defective domain where, for example, poling is incomplete, leading to partial inversion, the linear electrooptic response at this domain will be weaker than for regular domains.

4.4 Results and discussion

In this study, we applied the PLEOM to study a 1D periodically poled KTP crystal with a 36 μm period. Quantitatively meaningful amplitude and phase images of the linear electrooptic response from this crystal were acquired within the experimental configuration described in the previous section. The sample beam propagated through the crystal along the z direction with the linear polarization along the y axis. The voltage modulation frequency was 20 kHz. Complementing to experimental measurements, simulations were performed to predict and account for the experimental results.

4.4.1 Simulated results

Due to the bulky shape of the crystal and strong focusing condition of the sample beam illuminates the sample through a conical volume as in Fig. 4.5. Under these conditions, the initially linearly polarized state of light rays is not maintained. The polarization state of rays which are angularly far from the center of the beam are much more disrupted than that of other rays. Due to the Gaussian distribution of

the sample beam, the main part of the optical energy is along the central beam. We can then safely assume that the sample beam still maintains its linearly polarized state along y.

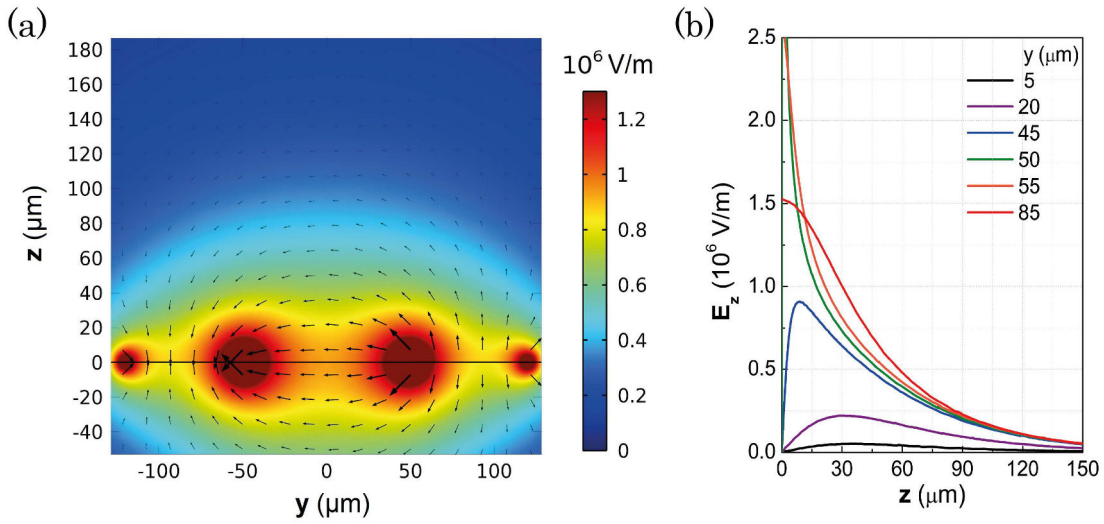

Figure 4.6: (a) 2D map in the yz plane of the distribution of the electric field around the two gold electrodes. The direction of the electric field vector follows dark red arrows with its amplitude is colour coded. The electrodes themselves are not visible due to their negligible thicknesses but their edges can be recognized due to the stronger electric field at their vicinity (in dark red). (b) Profiles of the E_z component as a function of z axis at different y positions. The origin of the z axis corresponds to the gold electrode surface or the crystal bottom surface, while zero of y corresponds to the middle point between the two gold electrodes.

As already discussed in section 3.5.1, in the case of flat gold ribbon electrodes, the generated electric field features only two non-zero components along y and z as shown in Fig. 4.6a whereas the x component is zero because of symmetry property.

From the linear electrooptic tensor of KTP in expression 3.3 with coefficients given in the Table 3.2, variation of the inverse dielectric constant $(1/n^2)_y$ of the KTP crystal for y polarized light traveling along z under the application of an external electric field is given by:

$$\Delta\left(\frac{1}{n^2}\right)_y = \sum_j r_{2j}E_j(\Omega) = r_{23}E_z(\Omega) \tag{4.10}$$

So that variation of the refractive index of this crystal for y-linearly polarized beam

is:

$$\Delta n_y = -\frac{1}{2} n_y^3 r_{23} E_z(\Omega) \tag{4.11}$$

where n_y is the refractive index of crystal. The value of n_y is given from the well known Sellmeier expression 3.1 with coefficients from Table 3.1.

The Pockels phase shift of the j^{th} ray which travels through the sample along z direction is:

$$(\Delta\varphi_j)_y = -\frac{\pi n_y^3}{\lambda} \int r_{23} E_z(\Omega) \mathrm{d}z \tag{4.12}$$

From expression 4.3 we see that the phase shift of light rays depend only on the $E_z(\Omega)$ component of the external electric field in this case. This phase shift scales with the integral of the $E_z(\Omega)$ component along the optical path of this ray. By using the COMSOL software (4.2 version) to simulate the $E_z(\Omega)$ component of the external electric field, the profile of this component as a function of z at different y positions is shown in Fig. 4.6b under application of an 150 V DC voltage on the two ribbon electrodes. With this gold electrode system, the magnitude of E_z becomes negligible at distances above 150 μm along z as from Fig. 4.6b.

Simulated result for a scan along y

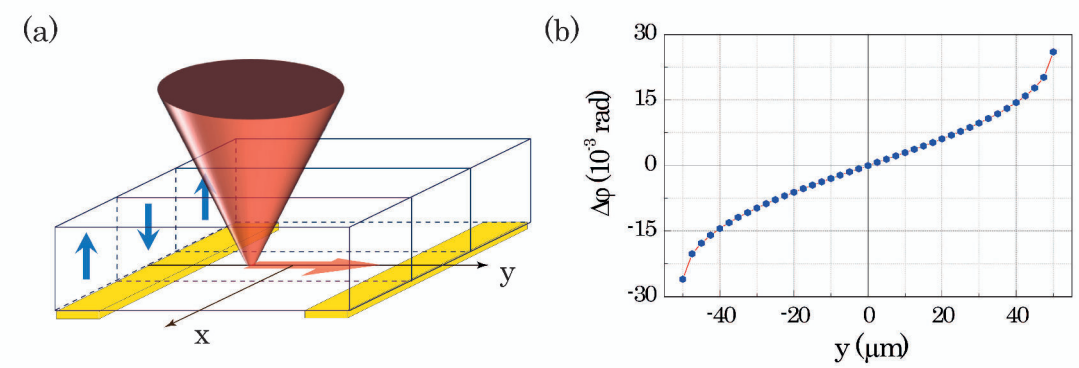

FIGURE 4.7: (a) Scheme of experimental scanning along y when the focused spot of the sample beam intersects the symmetry axis of a ferroelectric domain. (b) Simulated Pockels phase shift of the sample beam corresponding to the scan in Fig a.

When scanning along y with the focused spot maintained at the center of a ferroelectric domain as in Fig. 4.7a, the relative position of the sample beam with respect to the crystal does not change during the scan. Consequently, the linear electrooptic response for this case is given by the pathway integral of the E_z component:

$$\Delta\varphi_y \propto \int E_z^{\Omega}(z)\mathrm{d}z \tag{4.13}$$

Using the COMSOL software to perform this integration at different y position, the simulated phase shift of the sample beam for this scan is shown in Fig. 4.7b. From the distribution of the external electric field in the yz plane in Fig. 4.6a, the E_z component always cancels at $y = 0$ and reverses its orientation through this position. As a result, the Pockels phase shift of the sample beam used to sense the linear electrooptic effect in this crystal always cancels when the light beam focused at $y = 0$ and changes its sign when passing through this point as in Fig. 4.7b. The phase shift is linearly dependent on y at the vicinity of $y = 0$ while the dependence at the proximity of the electrode edges where the E_z^{Ω} component are strongest is a nonlinear and odd function of y. In agreement with this simulated Pockels phase shift, measurements are acquired by PLEOM, including the amplitude and phase signal as shown in Fig. 4.8. The sign change of the electrooptic phase shift of the

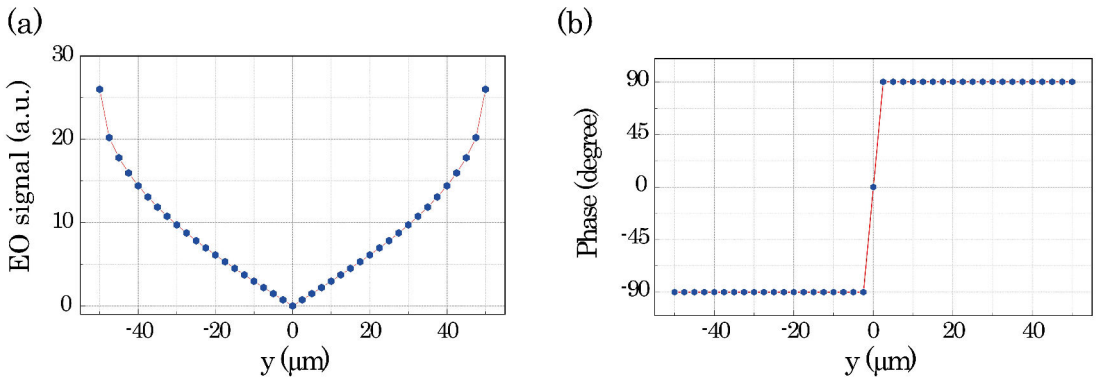

Figure 4.8: (a) Amplitude and (b) phase signal can be obtained from the experimental scan along y corresponding to Fig.4.7a can be acquired by PLEOM.

sample beam corresponds to a π shift of the phase signal as from Fig. 4.8b. In this

scan, the experimental phase measured by PLEOM corresponds to the vectorial orientation of the external electric field. Consequently, the direction of the external electric field can be fully inferred from the phase signal.

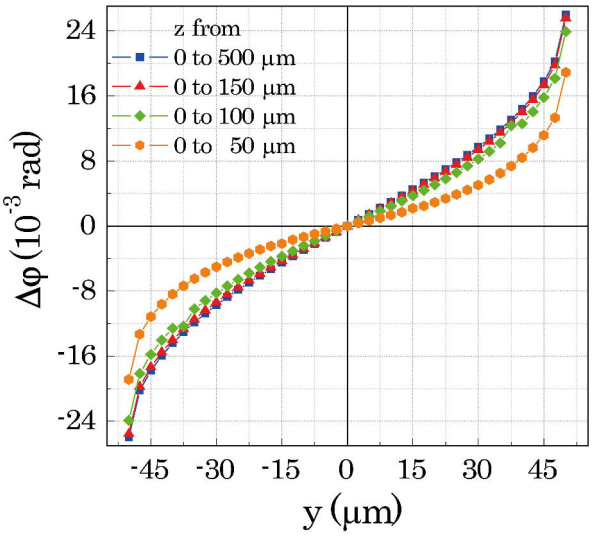

FIGURE 4.9: Simulated Pockels phase shift of the He-Ne laser beam passing through KTP crystal for different crystal depth defined from the bottom surface of the crystal at $z = 0$, as functions of y, corresponding to the scan in Fig. 4.7a.

The Pockels phase shift of the sample beam depends on its optical path when traveling through the crystal. In order to estimate the contribution of the intensity signal for different crystal thicknesses, the phase shift of the sample beam comprising the integrated length along z was simulated and is shown in Fig. 4.9. It shows that the contribution of the Pockels phase shift from the initial 50 µm layer of the KTP crystal is around a half of the overall contributions. Above 150 µm, there is no significant change in the value of the phase shift (less than 1%) up to the overall thickness of the KTP crystal (500 µm). As a result of the limited penetration of the external electric field into the crystal as shown in Fig. 4.6b. With the flat gold ribbon electrodes used in this study, PLEOM can reach the bulk of periodically poled KTP crystals up to a 150 µm depth from the electrode surface. When more in-depth information is sought,another electrode design allowing for deeper penetration of the

electric field inside the crystal is needed.

From our simulation result, PLEOM can be applied to map the external electric field including its amplitude and direction based on the linear electrooptic effect.

Simulated result for a scan along x

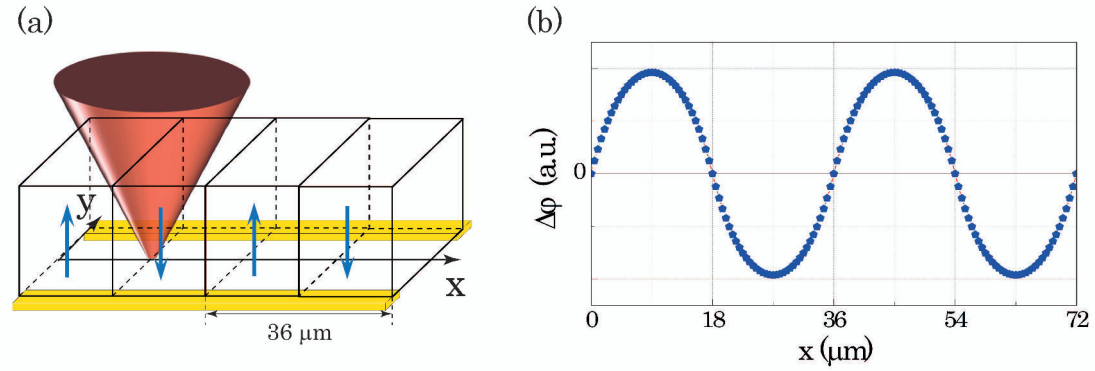

Figure 4.10: (a) Scheme of a scan along x. (b) Simulated Pockels phase shift of the sample beam corresponding to this scan in a periodically poled KTP crystal is used with 36 µm periodical length.

Another scan along x at a fixed y position as in Fig. 4.10a was simulated. Due to the mirror symmetry of the two gold electrodes, the $E_z^{\Omega}(z)$ component of the external electric field inside the beam volume is remained during this scan. Consequently, in this case, the Pockels phase shift of the sample beam (the amplitude of the total phase shift as in Exp. 4.9) is a function of x due to the variation of the morphology of the crystal volume intersecting with the sample beam during the scan as previously discussed in Section 4.3. One can then simply predict the outcome when the beam waist of the sample beam is at specific positions of higher local symmetry such as the domain wall or the center of a domain. At those special locations, the Pockels phase shift of the sample beam will be respectively minimal or maximal in the former case because of the compensation of different portions of the sample beam which travel through domains of opposite polarization.

In this simulation, we used a very simple model with the aim of retrieving the morphology from the dependence of the sample beam phase shift with respect to

x. Our first assumption is that the E_z^Ω component of the external electric field is homogeneous in the xy plane so that it is only a function of z ($E_z^\Omega(z)$) as shown in Fig. 4.6b at $y = 20$ μm. The function $E_z^\Omega(z)$ is inferred from fitting the simulated data. The second assumption to slice the conical volume of the sample beam up to 150 μm in height (e.g. in an interval from $z = 0$ to $z = 150$ μm where the $E_z^\Omega(z)$ component is significant) into thin layers of dz thicknesses. The distribution of light rays is a Gaussian function because the output laser mode is TEM_{00} Gaussian. So thus the total phase shift of all rays in expression 4.9 will becomes a volume integration. Our last assumption is that the parts of the sample beam which travel through domains with "up" dielectric polarization will experience a "positive" Pockels phase shift and a "negative" one for that traveling through the opposite domain.

We used MATLAB software to calculate the total phase shift of the sample beam corresponding to a scan along x, which is displayed as a function of x in Fig. 4.10b. When the beam waist is positioned across the domain wall, the phase shift cancels due to totally destructive compensation of the two precisely balanced parts of the sample beam which propagates through two opposite domains. It rapidly increases with the displacement of the beam along x away from the domain wall because of the beam's Gaussian distribution. The absolute value of the Pockels phase shift reaches a maximum when the beam waist is located at the center of a domain. The sign of this quantity changes when the scanning point moves from a regular to an inverted domain. Sign along x is of a different origin from that along y in the y case, the domain structure is maintained while the orientation of the E_z^Ω component is changed whereas in the x scan the domain structure is inverted while the E_z^Ω component is maintained. Those two scans can thus be considered as opposite cases.

From our simulated results, amplitude and phase signals can be obtained from the experimental scan along x by PLEOM as shown in Fig. 4.11. We see that the amplitude signal is a periodic function with the period precisely matching the domain size as in Fig. 4.11a, while inverted domains can be distinguished from

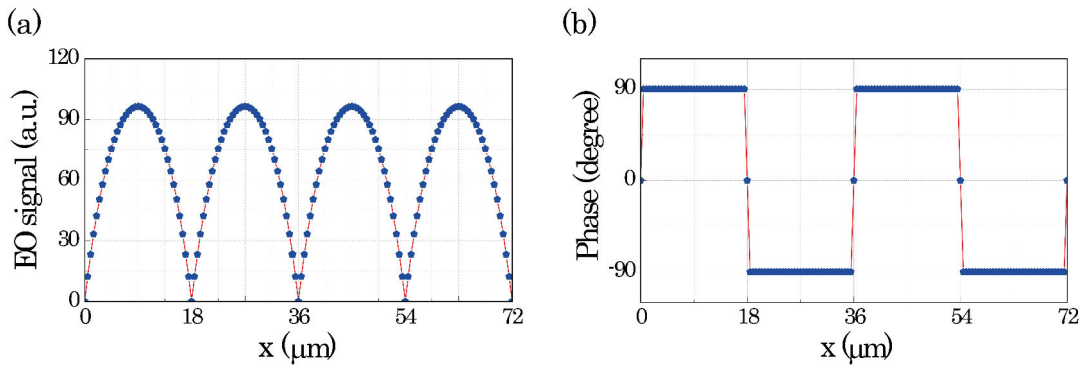

Figure 4.11: (a) Amplitude and (b) phase signals can be obtained from a scan along x corresponding to Fig.4.10a by using PLEOM on the periodically poled KTP crystal with 36 μm period.

regular domains by the π discontinuities in the phase image as in Fig. 4.11b.

Let now discus imperfect one in the ppKTP (periodically poled KTP) crystal. Such defects can relate to the size or the incomplete poling of an inverted domain. Such defects can be clearly detected from anomalies in the amplitude and phase of the Pockels signal as compared to defect-free neighboring domains.

From our simulated results of scans along y and x, a two-dimensional scan in the xy plane can be reconstructed from both of them with cross-sectional profiles along y and x axis exhibiting shapes as in Figs. 4.8a and 4.11a for amplitude and Figs. 4.8b and 4.11b for phase image respectively.

4.4.2 Experimental results

As a systematic test of the experimental signal obtained by PLEOM, its linear dependence versus the amplitude of the external electric field is tested to ensure that this response truly originates from the linear electrooptic effect. The linear dependence of the response from ppKTP crystal obtained by PLEOM is displayed in Fig. 4.12. From this result, it is clear that this response from the sample achieved by PLEOM is the linear electroptic signal.

Due to the small standard deviation of the experimental data points compared to fitted values, it could not be displayed in the graph. The value of the standard

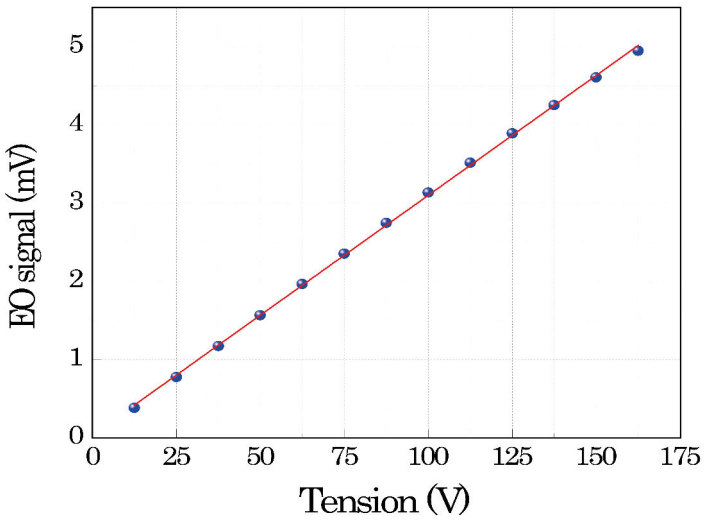

FIGURE 4.12: Linear dependence of the linear electrooptic response on the amplitude of applied voltage. The blue spheres are the experimental data from PLEOM, and standard deviation of each data point is too small to the extent that it can not be displayed. The red line is a leat mean square fit of experimental data.

deviation can be considered to be buried in the background noise. Considering its very high signal-to-noise ratio, PLEOM can be used to investigate ppKTP crystalline samples even under application of a low voltage so as to avoid any additional undesired poling or depoling process within the few ferroelectric crystal. By comparing with the linear electrooptic phase shift of the Pockels cell (reference source), the Pockels phase shift from the ppKTP crystal is in order of 10^{-4} – 10^{-3} radian corresponding to an applied voltage on the gold electrodes system from 12.5 to 165 V. This is from one to two orders of magnitude above the 10^{-5} radian sensitivity threshold of our current set-up.

Fig. 4.13 show two-dimensional amplitude and phase images of the Pockels signal from the ppKTP crystal obtained by PLEOM when performing a two-dimensional scan in the xy plane over a 60×60 μm^2 area with a 1.2 μm step, 100 ms acquisition time and synchronous detection. The resulting images cover 3.5 ferroelectric domains along the x axis and 60 μm wide interval in-between the inter-electrode space along y. The colour code in these images follow the magnitude of the signal for both amplitude and phase. These images are separated into two parts along the

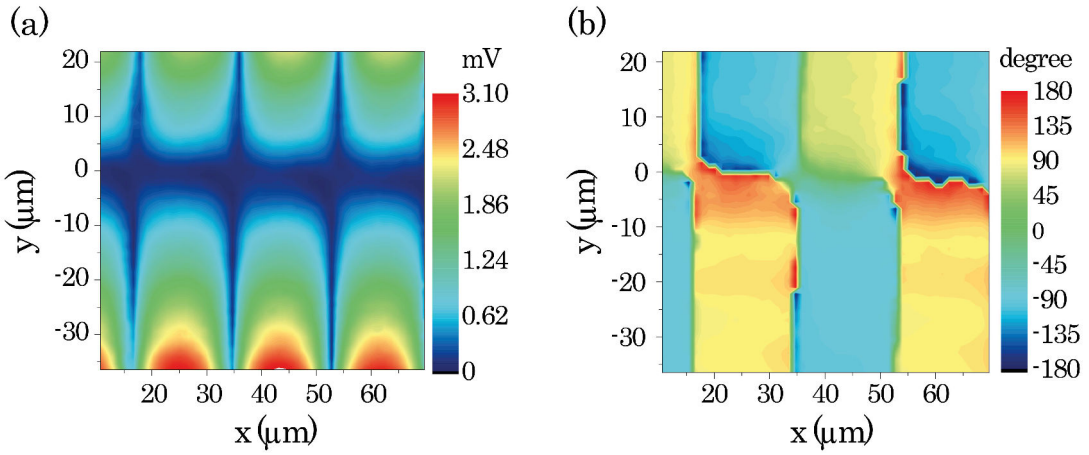

Figure 4.13: (a) Amplitude and (b) phase (measured phase) images of the Pockels signal from periodically poled KTP crystal structures obtained by PLEOM. The measured phase of the signal is the difference between the phase of EO signal and that of the reference voltage from the lock-in amplifier, as described in part 2.5.2.

$y = 0$ axis due to the symmetry of the pair of electrodes through this axis. The amplitude of the signal is zero because of the cancellation of the E_z component at $y = 0$ with a symmetric (rest. antisymmetric) distribution for the amplitude (rest. phase) images.

Fig. 4.14 shows cross-sectional profiles of amplitude and phase images along x and y at $y = -35.1$ µm and $x = 43.3$ µm positions respectively. From the amplitude profile (Fig. 4.14c), we got the cancellation of the signal amplitude at $y = 0$ and the linear dependency of the signal amplitude with respect to y. Moreover, the expected π shift of the phase signal confirms for the inversion of the orientation of the E_z component. These results are fully consistent with our simulation results, confirming that the Pockels phase shift of the laser beam in this experimental configuration is induced by the sole E_z component of the external electric field.

From the amplitude and phase images in Fig. 4.13, the periodic structure of the quasi-phase matched crystal along x comes out clearly. The amplitude signal is minimal at the domain walls and maximal at the center of a ferroelectric domain as seen in Fig. 4.14a. The measured period of 35.9 µm is in a good agreement with the the nominal definition of 36 µm. The π shift of the phase signal in Fig. 4.14b

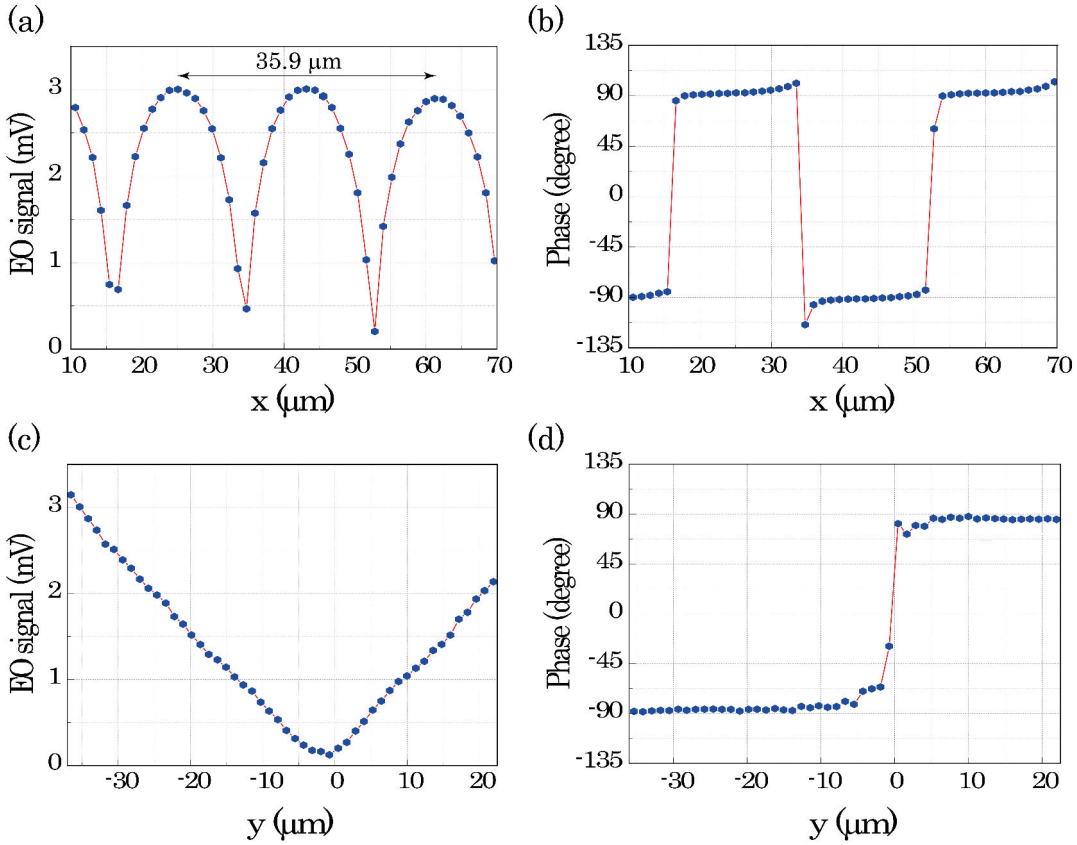

FIGURE 4.14: Cross-sectional profiles of the amplitude (a) and phase (b) images along x for $y = -35.1$ µm and along y for $x = 43.3$ µm (c) and (d) respectively. The period of 35.9 µm is in excellent agreement with the structural definition of the sample (36 µm).

is a clear signature of the difference between a normal and an inverted ferroelectric domain. The non-zero value of the signal amplitude at the domain wall can be explained by the step of the scan (1.2 µm per step), which does not permit to guarantee a perfectly symmetric incidence at the domain wall. It can also be that the non-zero minimum originates from other contributions such as the piezo elasto-optic effect [175, 176] or from the background noise. Taking a closer look at the phase of this measurement in Figs. 4.13b, 4.14b and 4.14d, at positions around the domain walls and the $y = 0$ symmetry axis, the phase appears to take random values (described by different colours in Fig. 4.13b) as a result of the low Pockels signal at these positions, which appears to be buried in the noise and taking random values.

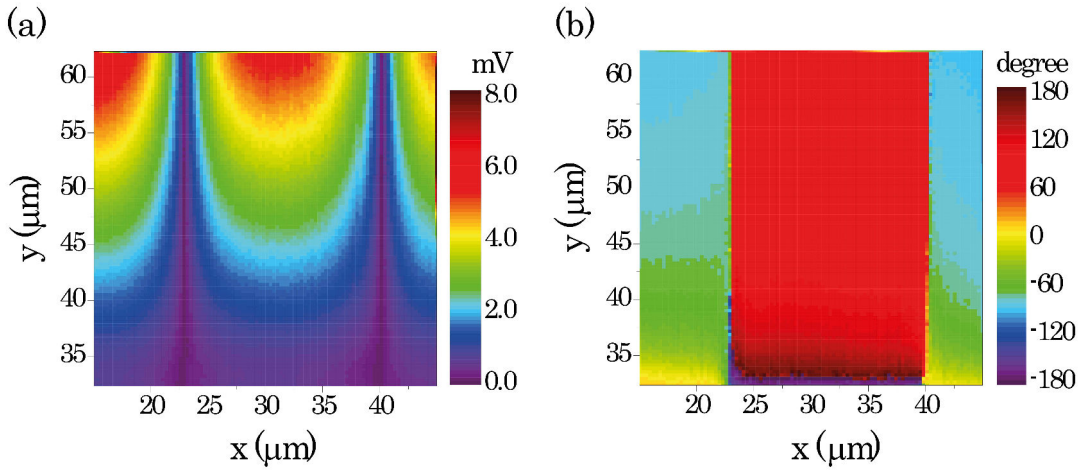

Figure 4.15: (a) Amplitude and (b) phase (measured phase) images of the Pockels signal from a periodically poled KTP crystal obtained by PLEOM. The two-dimensional scan in the xy plane covers a 30×30 μm^2 area by 300 nm steps with 100 ms acquisition time and synchronous detection.

Due to the limitations of confocal microscopy, the resolution of PLEOM is of the order of the focused spot ($\sim$ 630 nm). Fig. 4.15 shows amplitude and phase images of the Pockels response from a ppKTP crystal obtained by PLEOM when performing a two-dimensional scan in the xy plane with 300 nm steps to improve the resolution of the scan as compared to images in Fig. 4.13. With this higher resolution scan, the amplitude of the Pockels signal comes much closer to the zero at the domain walls, which brings credit to our explanation for the non-zero case in Fig. 4.14a.

In this study, we used a standard gold electrode system to generate the external electric field responsible for the Pockels effect inside the ppKTP crystal. The spatial inhomogeneity and inversion of the E_z component along y confirms the model and simulation. The homogeneity of E_z along x axis allows to map and distinguish inverted ferroelectric domains from regular ones. In order to check the quality of the poling process in ferroelectric crystals, the electrode design which generates a E_z component with a spatially uniform (x, y) distribution is preferred. In special cases, for a fast quality test of a 1D quasi-phase matched crystal with some unknown parameters such as the period length, defect domains, and others, a scan along x

which provides results as in Figs. 4.14a and 4.14b may be sufficient.

4.5 Summary and conclusion

In this chapter, we have presented a new, non-invasive method towards the characterization of the ferroelectric domain structure in 1D periodically poled crystals. The excellent agreement between simulated and experimental results provides a better understanding of the Pockels effect induced inside a ferroelectric crystal, which demonstrates a new application of PLEOM.

More specifically, our method enables to visualize the inversion of ferroelectric domains by using the Pockels effect, as manifested by a π phase leap in the measured phase and by our cancellation of the signal amplitude at the domain walls. From these results, our method can be further applied to determine poling periods and duty cycles, study the domain morphology, detect and characterize defects in the domain structure. PLEOM can be further extended for other types of ferroelectric crystal as well as to study two-dimensional poled structures [68] or nonlinear photonic crystals [40, 128, 152].

From theoretical calculations and experimental results, PLEOM can be used to map the spatial distribution of an externally applied electric field including its amplitude and direction. Experimental and theoretical models for the 2D or 3D external electric field mapping are given in Appendix A.2 part.

5

Electro-optic interferometric microscopy of aperiodic ferroelectric structures

Following the previously acquired theoretical and experimental results on the characterization of 1D periodically poled ferroelectric KTP crystalline structures, the PLEOM can be further applied to investigate periodically and aperiodically poled ferroelectric crystal structures of 2D or 3D spatially modulated the second order susceptibility $\chi^{(2)}$. I present in this chapter the demonstration of such an application of using the PlEOM to visualize and characterize the domain structure of two-dimensional decagonal quasi-periodic $LiNbO_3$ nonlinear crystal. These results demonstrate the potential of the PLEOM towards a more complete investigation of the ferroelectric domain structures of two- and three-dimensional photonic or quasi-periodically poled crystals.

5.1 Introduction

As was introduced in the previous chapter, optical frequency conversion schemes are among the most interesting applications of ferroelectric materials. Nonlinear processes in these crystals are governed by phase-matching requirements, with periodically poled crystals standing out as the most convenient and traditional implementation of this condition as theoretically predicted by Armstrong et al. in 1962 [10] and firstly demonstrated by Jundt et al. in 1991 [11]. During the following decade, a large research effort had been dedicated to the understanding and the development of fabrications technologies and to the applications of devices based on 1D periodically poled ferroelectric crystals [113–127], which are the simplest form of the nonlinear photonic crystals. It soon emerged quite natural that the concept and realization of one-dimensional quasi phase-matched crystals can be extended to higher dimensions starting with 2D structures. Nonlinear frequency conversion in two-dimensional photonic crystal was firstly investigated from a theoretical point of view by Berger in 1998 [12]. Much faster than in the case of the 1D periodically poled crystals, it took only two years from the proposition of two-dimensional nonlinear photonic crystal concept into its actual implementation as demonstrated by N. G. R. Broderick et al. with a Hexagonally poled Lithium Niobate structure [128]. To this day, two-dimensional nonlinear photonic or quasi-periodic crystals have remained attractive systems in the view of their unique properties in nonlinear optics and potential applications [40, 129, 152, 177–182].

As in the case of one-dimensional periodically poled crystals, the visualization and the characterization of two- or three-dimensional domain structure is a necessary step for the control of the poling process, in order to bring further improvements to nonlinear frequency conversion's efficiency. The domain structure of ferroelectric crystals is usually investigated by the selected etching methods [128, 177, 179], which are well-known and simple methods albeit destructive and with the limitations of applicability only to surface topography. The investigation of the domain structures can also be performed by all the methods with their respective drawbacks discussed

in the previous chapter. Among these, a new method based on the Čerenkov-type second-harmonic generation is very promising for visualization of domain boundaries in ferroelectric crystals [68–71, 174], as shown in Fig. 5.1.

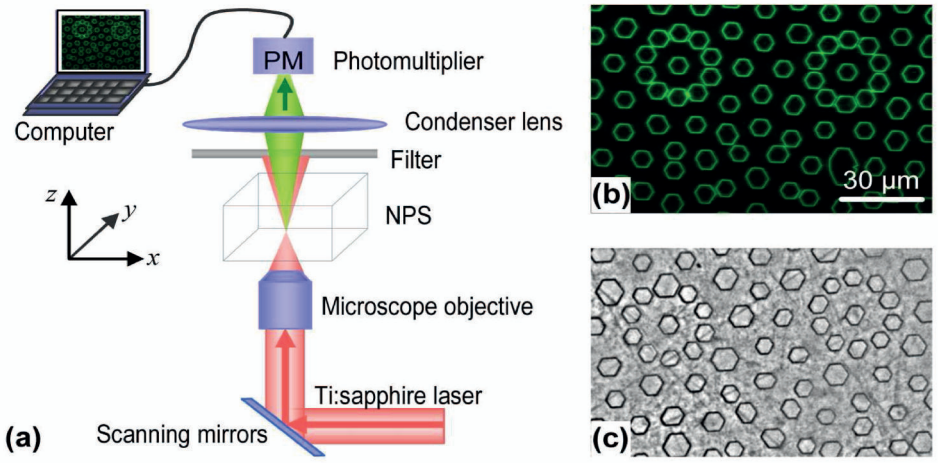

Figure 5.1: (a) Schematic of the Čerenkov-type second harmonic generation setup; (b-c) Images of the inverted domain pattern of a 2D quasi-periodic nonlinear photonic structure (NPS) obtained via (b) Čerenkov SHG inside the NPS and (c) optical microscopy after selective etching of the NPS surface [68].

This method permits imaging the domain boundary structure in three-dimensions with confocal microscopy resolution. In the general case of the majority of well-known ferroelectric materials such as KTP, $LiNbO_3$, KDP, etc, their domains can have only two orientations, up and down, with respect to the Z principal optical axis, allowing for the Čerenkov method to display it full potential towards the characterization and imaging of the domain contour in two-dimensional photonic (quasi) crystals.

Let me now discuss the kinetics of domain build-ups during electric field poling process, as shown in Fig. 5.2 [42]. A ferroelectric volume that is inverted by electric field poling must successfully pass six steps. Any error during the process will reduce the inversion to a small volume under electrode edges, limiting the poling process only to steps a and b in Fig. 5.2, and thus resulting in incompletely poled domain. As the Čerenkov method allows only to visualize the domain boundary of

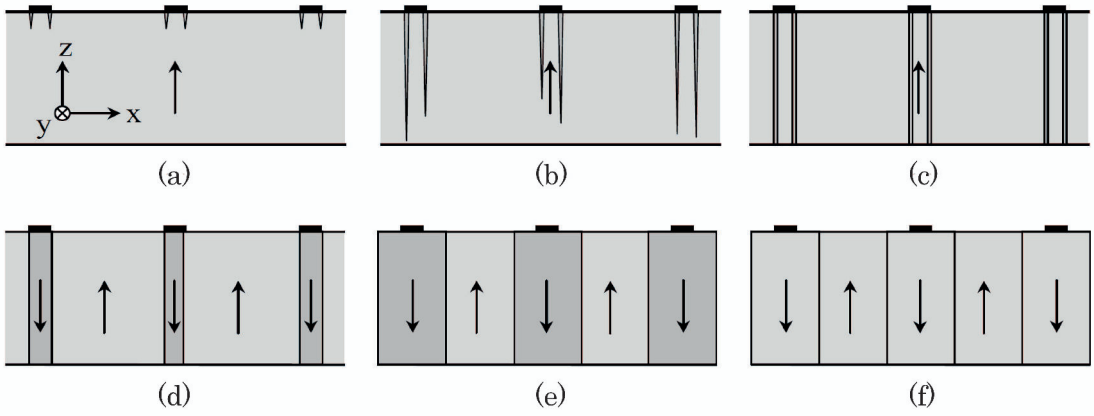

FIGURE 5.2: The six steps of domain growth kinetics during the poling process. (a) Domain nucleation at the electrode edges; (b) domain tip propagation towards the opposite face of the crystal; (c) termination of the tip at the opposite side of the crystal; (d) rapid coalescence under the electrodes; (e) propagation of the domain walls out from under the electrodes and (f) stabilization of the new domains [42].

ferroelectric crystals, it does not permit the discrimination of incompletely inverted domain from fully inverted one.

The abilities of PLEOM to visualize and characterize ferroelectric domains as detailed in the previous chapter makes it a complementary technique to the Čerenkov method for domain border visualization, and for investigating the interior of the domains in 2D patterned structures. Therefore, we used PLEOM in this study to characterize and visualize the domain structure of two-dimensional decagonal quasiperiodic $LiNbO_3$ nonlinear crystals (Fig. 5.1c) which has been developed to nonlinearly generate red-green-blue coherent light [129]. Its domain structure has been imaged by Čerenkov SHG microscopy (Fig. 5.1a) with the domain contours clearly evidenced in Fig. 5.1b [68]. Using PLOEM technique, we can complement the results of the Čerenkov microscopy study of decagonal quasiperiodic $LiNbO_3$ nonlinear crystal structure by acquiring the detailed topographic of the domain structure of the ferroelectric crystal, including the identification of completely and incompletely poled domains.

5.2 Lithium Niobate: structure and optical properties

Lithium Niobate ($LiNbO_3$) is a synthetic dielectric material, not existing in nature contrary to such traditional NLO materials as Quartz, albeit also not of comparable use in the applications. Lithium Niobate is indeed one of the most important nonlinear materials for integrated optics, and is widely used in many applications in nonlinear optics including second-harmonic generation, acoustic wave transducers, beam deflectors, optical modulators, etc [183]. In particular, this material is one of the most widely used materials for mid-IR range optical parametric oscillations. Lithium Niobate is a non-centrosymmetric, negative uniaxial and ferroelectric material, featuring large pyroelectric, piezoelectric, nonlinear, photo-elastic and electrooptic coefficients [184, 185].

5.2.1 Structure of Lithium Niobate

Lithium Niobate is an oxide compound with low-symmetry ABO_3 perovskite-like structure. At room temperature (much below T_C), $LiNbO_3$ is a trigonal crystal with point group $3m$ and space group $R3c$, thus lacking inversion symmetry. In the trigonal system, two different unit cells can be chosen: either hexagonal or rhombohedral. The conventional hexagonal unit cell in $LiNbO_3$ contains six molecular units with lattice parameters at room temperature: $a = 5.1483$ Å and $c = 13.863$ Å [184, 186, 187].

Above the Curie temperature T_C, $LiNbO_3$ goes to a paraelectric phase which is deprived of spontaneous polarization, as the Li atoms are lying in an oxygen layer displaced by $c/4$ distance away from Nb atoms, along the higher symmetry axis. At the same time, Nb atoms are equally distant from the oxygen layers as shown in Fig. 5.3b. Below the Curie temperature, lattice elastic forces dominate the thermal fluctuations of the atom positions, thereby forcing Li and Nb ions into new sites as shown in Fig. 5.3a. This rearrangement generates a spontaneous dielectric

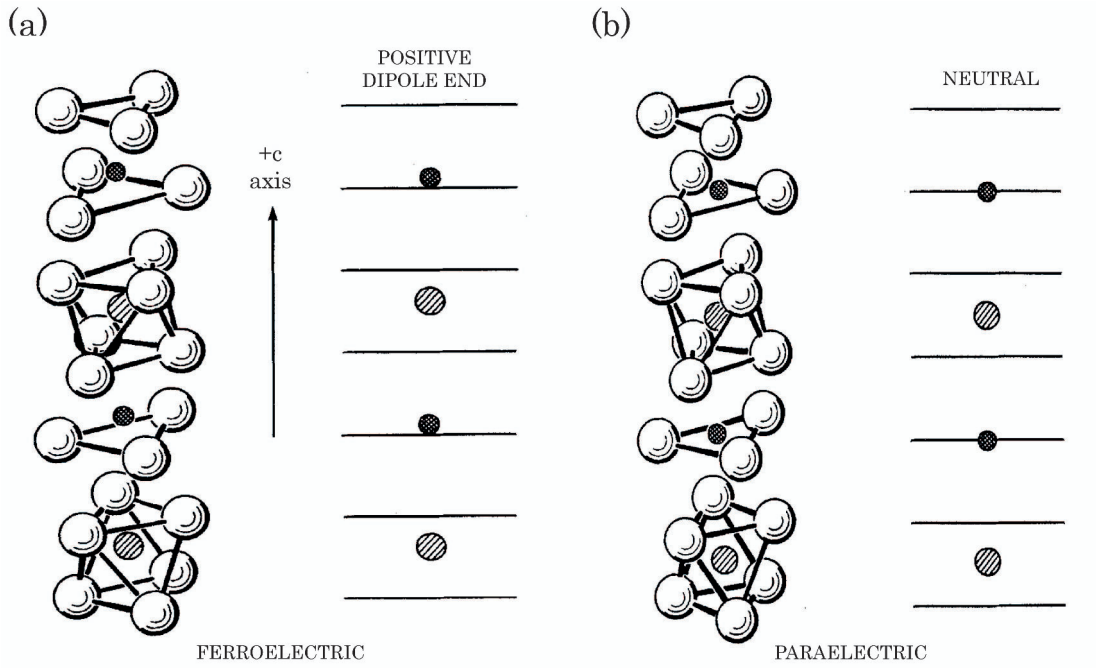

FIGURE 5.3: Positions of the Lithium atoms (double cross-hatched circles) and Niobium atoms (single cross-hatched circles) with respect to oxygen octahedra in the ferroelectric phase ($T < T_C$) (a) and the paraelectric phase ($T \geqslant T_C$) (b) of Lithium Niobate with the transition temperature of $T_C = 1210°\text{C}$ [184].

polarization along the c direction (z axis in the attached Cartesian coordinates for the principal dielectric frame) which accounts for the ferroelectric phase of $LiNbO_3$.

5.2.2 Optical properties of Lithium Niobate

$LiNbO_3$ is a negative uniaxial crystal. Thus, it has ordinary and extraordinary refractive indices, respectively n_o and n_e with $n_o > n_e$ corresponding to two orthogonal polarization [184, 185]. The values of those refractive indices are 2.2910 and 2.2005 respectively [184], at the room temperature ($T = 25°\text{C}$) and 632.8 nm wavelength of He-Ne laser [184].

$LiNbO_3$ belongs to the $3m$ class crystal so that the SHG optical tensor in contracted index form has the following form [41]:

$$[d] = \begin{bmatrix} 0 & 0 & 0 & 0 & d_{31} & -d_{22} \\ -d_{22} & d_{22} & 0 & d_{31} & 0 & 0 \\ d_{31} & d_{31} & d_{33} & 0 & 0 & 0 \end{bmatrix} \tag{5.1}$$

with the following values for the nonlinear optical coefficients: $d_{22} = 7.4$ pm/V; $d_{31} = 14$ pm/V; and $d_{33} = -98$ pm/V [41].

The electrooptic tensor, also in contracted form for the first index, can be simplified into [41, 188]:

$$[r] = \begin{bmatrix} 0 & -r_{22} & r_{13} \\ 0 & r_{22} & r_{13} \\ 0 & 0 & r_{33} \\ 0 & r_{42} & 0 \\ r_{42} & 0 & 0 \\ -r_{22} & 0 & 0 \end{bmatrix} \tag{5.2}$$

where the values of the non-zero coefficients at 632.8 nm are: $r_{13} = 8.6$ pm/V, $r_{22} = 3.4$ pm/V, $r_{33} = 30.8$ pm/V and $r_{42} = 28.0$ pm/V [41, 189].

5.3 Sample preparation

5.3.1 Two-dimensional decagonal quasi-periodic $LiNbO_3$ nonlinear crystal

In this study, we have investigated a two-dimensional decagonal quasi-periodic superlattice patterned by a selective electric field poling technique onto a z-cut $LiNbO_3$ wafer from Australian National University (within a cooperation with the research group of Prof. W. Krolikowski), which had been engineered towards efficient red-green-blue laser emission [129]. The microscopic $+z$ surface of the etched sample is shown in Fig. 5.4 [129] which exhibits the quasi-periodic geometric tiling with

a tenfold local symmetric axis. It is composed of thin (with vertex angles of 36° and 144°) and thick rhombs (72° and 108°). The side length of the rhombs is about $a = 13.19$ μm. The poled circular cylinders are placed at the vertices of rhombi and their diameters are of the order of 5.2 μm.

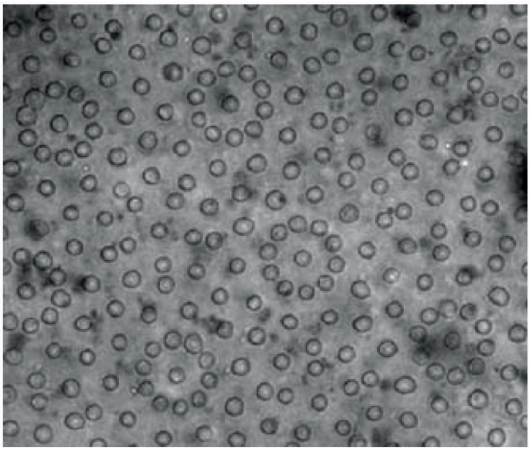

FIGURE 5.4: $+z$ face image of the poled decagonal $LiNbO_3$ quasi crystal after a selective etching process [129].

5.3.2 Configuration of the sample with respect to the optical beam and externally applied voltage

In this experiment, the flat gold ribbon electrodes had been prepared by vacuum evaporation and soft lithography as described in Section 3.4.1, and used here too, in order to generate quasi-static external electric field by connection with a generator, like in the previous experiments on single KTP nano-crystals and s 1D periodically poled KTP crystals. However, in the present case, the thickness of the gold ribbon electrodes was lowered to 20 nm, comprising a 10 nm thick chromium layer and 10 nm thick gold layer. With such thinner electrodes, the attenuation of the transmitted sample beam when it passes through the electrode area is reduced. As a result, this ribbon electrode system allows PLEOM to expand the scanning zone not only over the free spaces in-between electrodes, but also over areas covered by the electrodes.

$LiNbO_3$ crystals were oriented in the same way as periodically poled KTP crystals, as shown in Fig. 4.4a. The principal dielectric axis of the $LiNbO_3$ crystal was taken as the laboratory reference frame. The linearly polarized sample beam propagated along the crystallographic Z axis (coinciding with the z axis in laboratory frame). The incident beam was focused onto the bottom surface of the crystal, close to the ribbon electrodes, where the electric field was the strongest.

5.4 Results and discussion

5.4.1 Theoretical calculation

As already presented in the previous chapters, the external electric field generated from this ribbon gold electrode system exhibits only two non-zero components along the y and z axis because of the mirror symmetry conditions with respect to x, and due to the length of the ribbon electrodes which are much longer than their width. Fig. 5.5b shows the 2D map of the electric field generated by the ribbon electrodes in yz plane. In the region above the free area in-between electrodes, E_y and E_z components are significant, whereas above the gold electrodes, E_y component is negligible compared to the E_z component as shown in Fig. 5.5b.

After adequate focusing the sample beam by the first microscope objective at the bottom surface of the crystal, the intersection of the sample beam and the effective space of the crystal (where the external electric field can penetrate effectively) defines a conical interaction volume. Consequently, the initially linearly polarized state of light rays is not maintained. Due to Gaussian distribution of the sample beam, the main part of the optical energy propagates along the center beam. Based on the validity of the assumption presented in the previous chapter to simulate periodically poled KTP, we assume that the sample beam maintains its linear polarization within the xy plane while propagating along z. The electrooptic phase retardation $\Delta\varphi_i$ of a light ray with its linear polarization along the i axis (i being either x or y) when

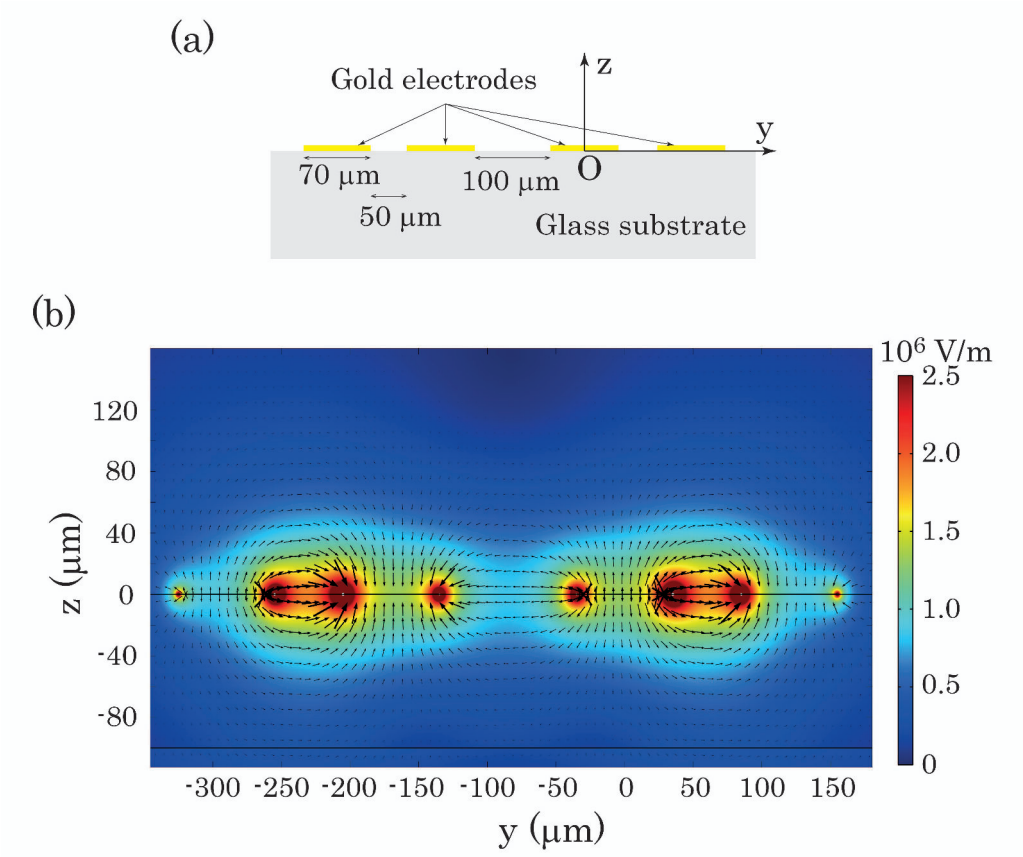

FIGURE 5.5: (a) Electrodes' cross-section in the yz plane. The thickness and width of the gold electrodes are respectively 20 nm and 70 µm which are much smaller than the electrode's length, and the distance between the electrodes alternates between 100 µm or 50 µm. (b) Two-dimensional map of the electric field generated from these electrodes in yz plane. Its orientation is shown by black arrows and its magnitude is colour coded.

it propagates along the z is given by the following formula:

$$\Delta\varphi_i = \frac{\pi n_o^3}{\lambda} \int \sum_j r_{ij} E_j^{\Omega} \mathrm{d}z \tag{5.3}$$

where n_o is the ordinary refractive index of the crystal, E_j^{Ω} is the j component of the external electric field at Ω frequency, r_{ij} is the linear electrooptic coefficient which is given from expression 5.2, and λ is the wavelength of the laser beam.

If the polarization of the incident ray is along the x, its electrooptic phase shift is given by:

$$\Delta\varphi_x = \frac{\pi n_o^3}{\lambda} \int \left(-r_{22} E_y^{\Omega} + r_{13} E_z^{\Omega}\right) \mathrm{d}z \tag{5.4}$$

In the case of linearly y-polarized sample beam, the corresponding linear electrooptic phase retardation is given by the following expression:

$$\Delta\varphi_y = \frac{\pi n_o^3}{\lambda} \int \left(r_{22} E_y^{\Omega} + r_{13} E_z^{\Omega} \right) \mathrm{d}z \tag{5.5}$$

Expressions 5.4 and 5.5 account for the phase retardations introduced in the light beam by the Pockels effect in $LiNbO_3$ crystal in the configuration where both E_y^{Ω} and E_z^{Ω} components of the external electric field contribute. This situation is more complex than that in the case of the KTP crystal, where the Pockels phase shift was seen to depend only on single E_z^{Ω} component. In order to simplify the case at hand, the scanning zone was chosen above the gold electrode area where the E_y^{Ω} component can be neglected as evidenced in Fig. 5.5b. As a result, the Pockels phase retardation for the scanning beam with a linear polarization along y (or x) axis becomes:

$$\Delta\varphi_y = \frac{\pi n_o^3}{\lambda} \int r_{13} E_z^{\Omega} \mathrm{d}z \tag{5.6}$$

Building-up on the model that had been proposed and confirmed for the case of periodically poled KTP, the Pockels phase shift experienced by this optical wave can take a positive or a negative values, depending on beam's path. If the optical path stays within a regular (resp. inverted) ferroelectric domain, the Pockels phase shift takes a positive (resp. negative) value. In the paraxial approximation, the linear electrooptic phase shift experienced by the sample beam can be averaged over all contributing rays. Consequently, the signal is minimal when destructive compensation occurs due to equal and opposed contribution from opposite domains, e.g. when the beam waist of the sample beam is centered at the domain boundary.

5.4.2 Experimental results

In this study, a 150 V AC voltage at $\Omega = 20$ kHz modulated frequency was applied to the ribbon electrode system to generate external quasi-static electric field. The scanning zones were chosen above the electrode area where the E_y^{Ω} component was

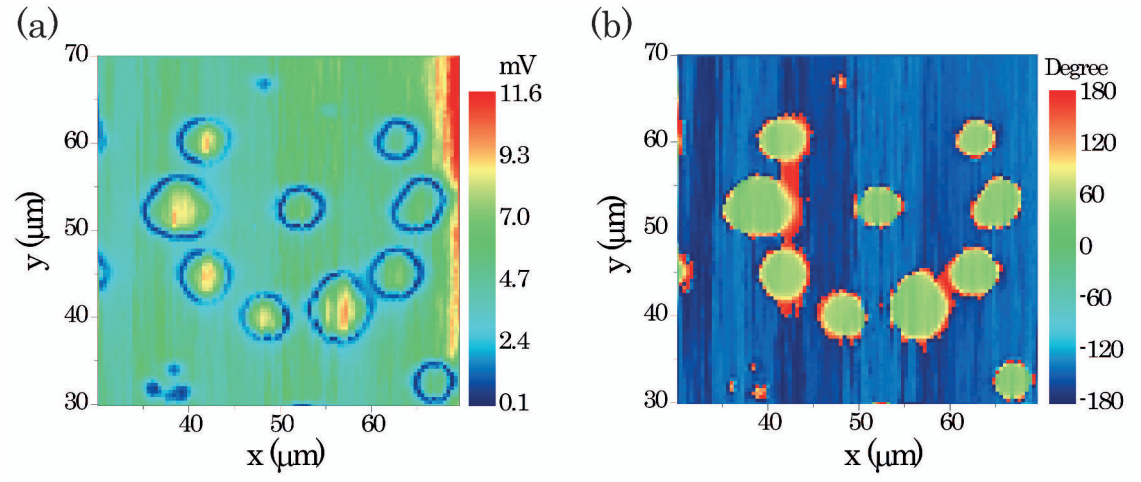

FIGURE 5.6: (a) Amplitude and (b) phase (measured phase) images of the Pockels signal from the two-dimensional decagonal quasi-periodic $LiNbO_3$ nonlinear crystal obtained by PLEOM with the magnitude is colour coded. Measured phase of the signal is the difference between the phase of EO signal and that of the reference voltage from lock-in amplifier.

neglected and the E_z^{Ω} component considered as an approximately spatially homogeneous electric field within xy plane.

The image decagonal quasi-periodic $LiNbO_3$ nonlinear crystal in the amplitude and phase images of the Pockels signal are shown in Fig. 5.6. The images were obtained with the PLEOM working in synchronous detection mode, performing a 2D scan in the xy plane over a 40×40 μm^2 area with a 400 nm step, 100 ms acquisition time. In the scanned area, both images are clearly seen to correspond to a grouping of domains abiding to tenfold local symmetric according to the designed pattern. The colour code in these images describes the magnitude of the Pockels signal including both amplitude and phase. The red coded zone at the right side of the amplitude image corresponds to high Pockels signal at the vicinity of the electrode edge where the E_z^{Ω} component is peaking.

In contrast with the case of 1D periodically poled nonlinear crystals, the amplitude image of the current two-dimensional quasi-periodic structures only shows the domain boundaries corresponding to the minima of the amplitude of the Pockels signal. This minimal amplitude originates from the destructive compensation when the beam waist of the sample beam is equally shared by regular and inverted

structures. The frontiers of the inverted domains are marked with the blue coloured contours of different sizes an shapes, as shown in the amplitude image. An expected π shift allows to distinguish inverted domains from the regular ones as shown in Fig. 5.6b. The average diameter of inverted domains is found to be approximately 5.5 µm, which is in good agreement with the structural design. The characteristic PLEOM signature of completely poled domain are a closed border line (coded in blue) in the amplitude image and a phase value inside such boundary shifted by 180° with respect to the exterior (that is, the regular un-poled structure) as shown in Figs. 5.6, 5.7 and 5.8.

The PLEOM amplitude image of the domain pattern (Fig. 5.6a) is in excellent agreement with that from Čerenkov SHG microscopy as shown in Fig. 5.1b. In Čerenkov SHG microscopy, the image is built from Čerenkov SHG signal generated at the beamwaist of strongly focused fundamental beam, which act as quasi-point harmonic source. In contrast, the image obtained by the PLEOM is build from progressive accumulation of the Pockels phase shift along the optical beam path through the crystal. Thus, in contrast to Čerenkov SHG microscopy, which brings a signal only from the walls of the inverted domains, the PLEOM provides the information from entire crystal. Taking a closer look at Fig. 5.6, we can see only 8 inverted domains surrounding a central one, whereas the original design included 10 inverted domains. Two inverted domains are missing at the upper positions in order to fulfill the local ten-fold symmetry. At the location of one of the two missing inverted domains defined by the coordinates(48 µm, 67 µm), one can identify a small area coded in blue colour corresponding to low magnitude Pockels signal. The very small size of this blue spot can be the signature of an incompletely poled domain at this location, as well as that of a completely poled domain of very small radius. The case of an incompletely poled domain is better evidenced at (38 µm, 33 µm) coordinates, as in Fig. 5.6a, where the blue line delineated domain frontiers, and the characteristic π shift from inside to outside are both absent. However, for such incompletely poled domain which only small volume around the electrode edge with the shape as the boundary contour of a completely poled one is poled as shown in

Figs. 5.2a, b and c, the Čerenkov SHG microscopy would provide a domain wall image similar to that of the completely poled one.

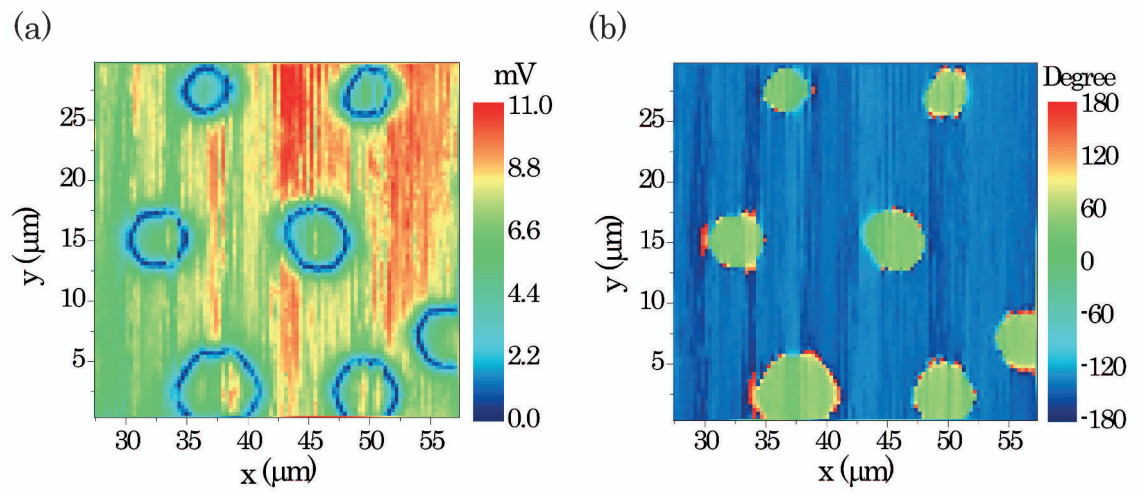

FIGURE 5.7: PLEOM generated (a) Amplitude and (b) Phase images of the Pockels signal from a two-dimensional decagonal quasi-periodic $LiNbO_3$ nonlinear crystal of thin rhomboid shape.

Performing another scan over a 30×30 μm^2 area with a smaller 300 nm step, 100 ms acquisition time and synchronous detection, the amplitude and phase image in Fig. 5.7 captures a thin rhomboid structure with six inverted ferroelectric domains arranged on a quasi-hexagon around a centered domains. The average lateral length of the rhomb is around 13.0 μm and the diameter of the inverted domain ranges from 4 to 8 μm, very much in consistent with the structure design [129]. In this area, PLEOM exhibits completely poled domains without any incomplete one as in the previous scan.

The electrooptic dephasing carried by the optical beam and then measured by PLEOM is sensitive to variations of the refractive of the sample that have been captured within the conical volume carved by the incident beam in the sample. Domain boundaries are then visualized by the destructive interference compensation of the Pockels response of the two parts of the laser beam that propagate in oppositely poled domains. If the diameter of an inverted domain is small with respect to the

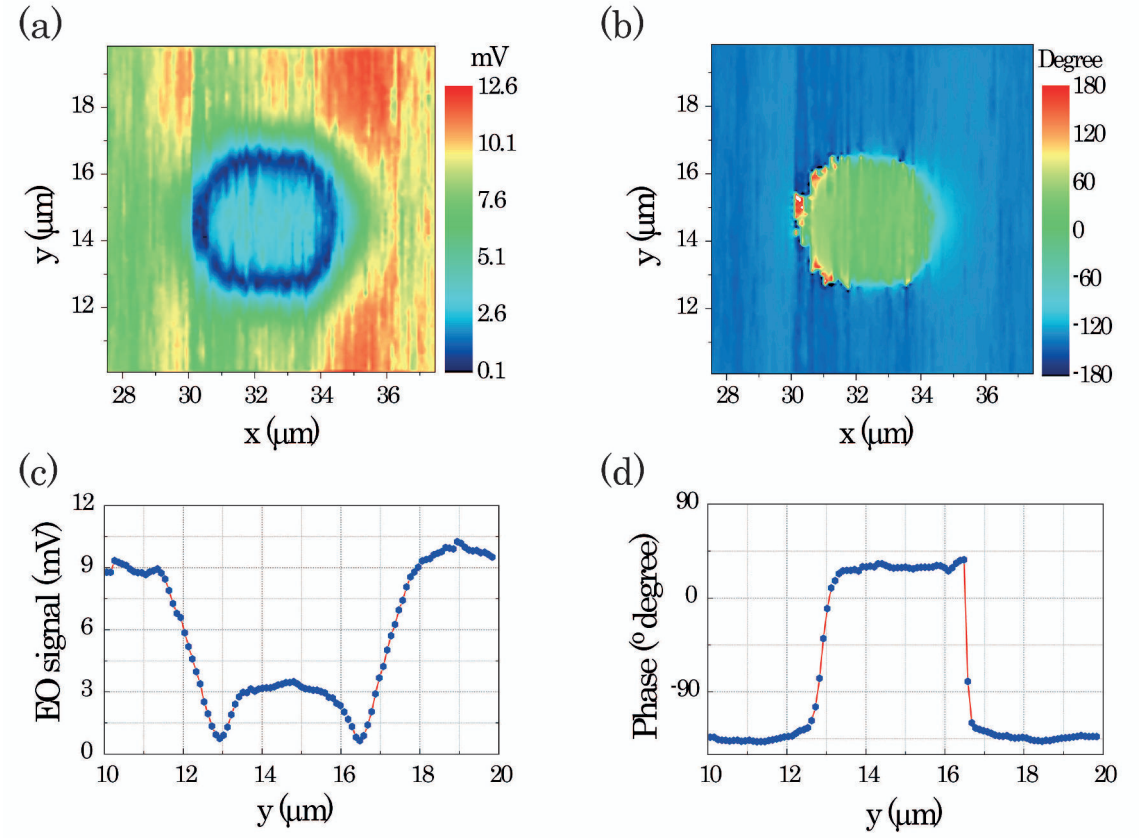

Figure 5.8: (a) Amplitude and (b) phase (measured phase) images of the Pockels signal from a two-dimensional decagonal quasi-periodic $LiNbO_3$ nonlinear crystal as obtained by PLEOM over an area including an inverted domain. Cross-sectional profile lines along y at $x = 32.4$ μm of the amplitude (c) and phase image (d).

beam waist, a fully destructive compensation can not occur. Consequently, this sets a lower limit to the size of a completely inverted domain that PLEOM is capable to visualize. Such limit size depends on the thickness via a linear relation. In this work, the thickness of sample is thicker than the effective penetrating depth of the external electric field E_z^{Ω} which could be estimated to be of the order of 150 μm as the simulation in the previous chapter.

Performing a scan over a small area comprising only one inverted domain with a diameter of the order of 4 μm, amplitude and phase images from the Pockels signal for this area are shown in Figs. 5.8a and b. The cross-sectional profiles of the amplitude and phase image along y at $x = 32.4$ μm are represented in Figs. 5.8c and d respectively. Fig. 5.8d clearly evidences a π phase shift from the inverted

to the regular domain whereas Figs. 5.8a and c point-out the boundary in-between these, where the Pockels response is minimal. The smaller signal at the interior of the inverted domain compared to that for the regular domain is due to the conical volume of the sample beam even when its focused spot is posited inside the inverted domain, always overlaps a part of the regular one, thus responsible to a partially destructive interference. Further reduction of the domain size would increase this destructive contribution. Accordingly, PLEOM can not visualize and characterize an inverted domain below a certain domain which depends on the focusing conditions and sample thickness. In the present configuration, the lower limit size for an inverted domain to be visualized by PLEOM is of the order of 2 μm. In other cases, the thinner the thickness of the sample, the lower the limit of an inverted domain which can be detected by PLEOM. In conclusion, PLEOM has the potential to visualize and characterize two-dimensional nonlinear photonic crystals with periodic length as small as the size of the beam waist of the laser in the sample, for an appropriate thickness.

5.5 Conclusion

The results detailed in this chapter clearly establish the potential of PLEOM for investigating both one-and two-dimensional nonlinear crystals. An inverted domain is distinguished from a normal one by a measurable π shift in the phase image, whereas the amplitude image points at boundaries between ferroelectric domains. Incompletely poled domains can be detected by PLEOM, thus providing an efficient characterization tool for the domain structure. Combined with Čerenkov SHG microscopy, it is able to provide detailed quantitative information on each ferroelectric domain in a periodic as well as aperiodic nonlinear structure.

The success of this study in the case of the more complex $LiNbO_3$ electrooptic crystal that sustains eight non-zero linear electrooptic tensor coefficients compared with the simpler case of KTP confirms the ability of PLEOM to image and characterize the domain properties of all ferroelectric materials with one- or two-dimensional

periodic or aperiodic photonic structures, moreover bringing in important phase related information that is not readily available from Čerenkov SHG microscopy.

Using PLEOM, I could visualize with a very good resolution inverted domains in a two-dimensional decagonal quasi-periodic $LiNbO_3$ nonlinear crystal with a diameter down to 4 μm. Results in the chapter substantiate the potential of PLEOM for further characterization ferroelectric domains down to the diffraction limit.

6

Conclusion and perspectives

Advances in the fabrication of tailored nonlinear materials with artificial domain structures towards nonlinear optical frequency conversion triggered the activity of a numerous research groups worldwide. Nonlinear crystals which feature a spontaneous dielectric polarization belong to the important ferroelectric class are particularly relevant in the this research. Accordingly, high resolution quantitative imaging of ferroelectric domain structures are in high demand towards a better understanding of these materials for upstream physical reasons as well towards the improvement of fabrication processes of nonlinear optical and related ferroelectric based devices. Following the work of two previous doctoral thesis [66, 67], and the conception and earlier demonstration of a homemade microscopy that combines confocal microscopy with Mach-Zehnder interferometry and balanced homodyning,with

its operating principle based on the Pockels effect, our purpose has been here to improve this setup and allow it to embrace new applications. In this perspective, we proposed to investigate ferroelectric materials, which currently account for an important part of nonlinear materials from bulk format such as in laser pointers or optical parametric sources, down to the nano-scale as for nonlinear labels in bioimaging of cells, membranes or tissues [38, 46, 48, 58, 102].

We recall in this thesis the experimental setup, working principle and applications to nonlinear materials of our home made Pockels Linear Electro-Optical Microscope (PLEOM). In this study, we have demonstrated the relevance of PLEOM towards the investigation of ferroelectric domain structures from bulk down to nano scale. The main results of this work are summarized in the following:

Firstly, we have developed a full theoretical analysis of electrooptic light scattering from randomly oriented KTP single domain nano-crystals. Based on experimental results obtained from 150 μm KTP nano-crystals by PLEOM as presented in Chapter 3, we have demonstrated for the first time that the orientation and more specifically the vectorial features attached to the dielectric dipole moment of a single random ferroelectric nano-crystal could be accurately extracted from the polarization plot and the phase of its Pockels response. These results validate the capacity of PLEOM to be applied to 3D imaging by use of ferroelectrics as nano-scale probes. The full determination of the vectorial features of single ferroelectric domains at the nano-scale allows to use ferroelectric nano-crystals quantitative Voltage or field nano-scale sensors with applications in optoelectronics and biology. The good agreement between our theoretical model and the experimental results qualify PLEOM towards the investigation of a broad range of ferroelectrics down to the nano-scale. Moreover, the high signal-to-noise ratio and broad detection dynamics of PLEOM open the way to the mapping of even smaller nano-crystals of even smaller sizes (from 100 to 10 nm) especially for nonlinear materials with high Pockels coefficients such as $BaTiO_3$ or $Sr_{0.6}Ba_{0.4}NbO_6$, etc... Then nano-scale applicability of PLEOM could then compare to that of second-harmonic generation microscopy where a record of 11 nm was reached in our laboratory for II-VI CdSe

based semiconductor nanoparticles [61].

We have also introduced in this work a new and non-invasive method towards the characterization of the ferroeelctric domain structure of 1D periodically poled crystals, choosing for this demonstration a KTP structure with 36 μm period and the cubic micrometer volume range ($10\times2\times0.5$ mm^3). We have reported in Chapter 4 the ability of PLEOM to visualize the inversion of ferroelectric domains by a π shift from the phase signal whereas the domain boundaries could be clearly singled-out and mapped, based on the cancellation of the signal amplitude. A theoretical model for the evaluation of Pockels response via PLEOM periodically poled KTP crystals was proposed, and used in simulations. The excellent agreement between simulated and experimental results provide a better understanding of the Pockels effect induced within the ferroelectric KTP crystal as well as the experimental potential of PLEOM to address such issues. Using the configuration of this experiment, a fast test of the quality of 1D quasi-phase matched crystals in order to evaluate some unknown parameters such as their period length, defect domains, and others can be efficiently performed in a fast mode, by restricting the scan form 2D to 1D, along the x direction only.

Furthermore and along the same direction, PLEOM bears the ability to characterize and visualize periodic or aperiodic domain structures of the ferroelectric poled crystals of higher order than just two- or three-dimensions. Building-up on this possibility, we proved that PLEOM could be fruitfully applied to a decagonal quasi-periodic superlattice of Lithium Niobate, another benchmarking ferroelectric crystal, namely $LiNbO_3$ as reported in Chapter 5. In this case, microscale cylindric inverted domains could be distinguished from the regular background domains by a π shift of the phase signal, whereas the amplitude image displays the domain boundaries. A quasi-periodic geometric tiling with ten-fold symmetric axis and a thin rhomb could thus be imaged by PLEOM. The average diameter of the inverted domains and side length of the rhomb in this structure are approximately 5.5 μm and 13.0 μm respectively, which are in excellent agreement with the pre-defined design of the structure. Completely poled domains are characterized by PLEOM through

their closed contours in the amplitude image and opposite phase values in the phase image, whereas incompletely poled domains fail to satisfy those criteria. The lowest boundary size for a completely poled domain to be investigated by PLEOM can be estimated to be of the order of 2 µm for a thick crystal with the thickness higher than 150 µm and can come down to the size of the focusing spot when considering a thinner crystal.

The successful outcome of PLEOM based investigations of crystals including one- to two-dimensional periodic as well as aperiodic electrooptic structures, confirms the potential of PLEOM to visualize and characterize domain structures of all ferroelectric patterned structures, from crystalline to liquid crystalline phases [190, 191].

Based on results reported in this work, PLEOM offers most promising perspective in the field of nonlinear optical materials and structures, entailing important applications in life sciences or optoelectronics devices. Moreover, full characterization by PLEOM at nano-scale enables the use of nano-crystals as nano-probes for 2 or 3D imaging of biological objects, which is currently the most promising and demanded applications for nonlinear optical crystalline structure. Beside the application in order to investigate nonlinear materials, the evaluation of an external electric field comprising its magnitude and direction can be performed as detailed in part A.3.

After setting-up and testing the advanced configuration of PLEOM presented in Section 2.5.3, and increasing number of entities such as plasmon sustaining metallic or non-transparent nano-particle can be investigated via electrooptic scattering from their surface.

A

Appendix

A.1 Pockels cell as a reference for the Pockels retarded phase measured by PLEOM

In this Section, we will briefly introduce the working principle and application of a Pockels cell, which is used as a bench-marking reference for the conversion of an electric signal measured by PLEOM onto a Pockels retarded phase. In our PLEOM set-up, we have used a Pockels cell with a double Q-switch interface produced by the LEYSOP company.

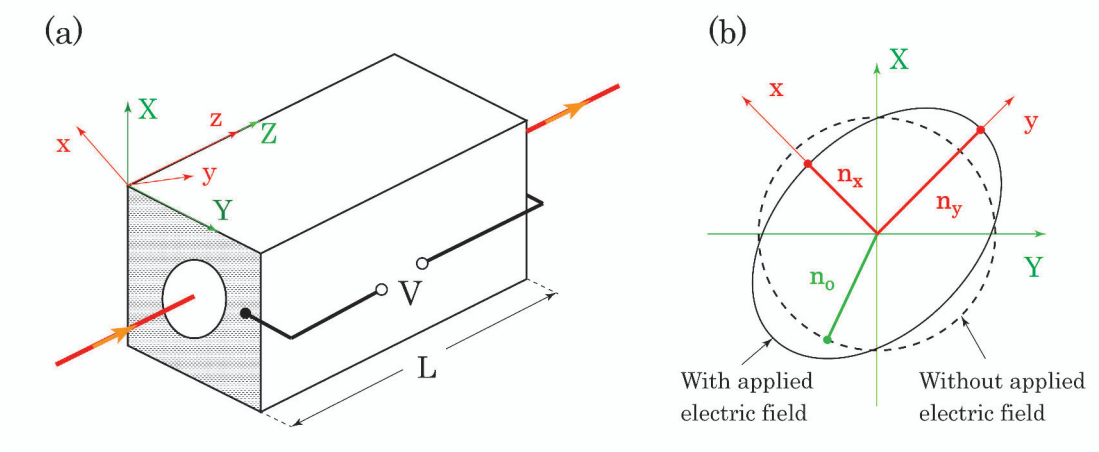

Figure A.1: (a) Schematic diagram of a Pockels cell using a KD*P crystal in longitudinal mode (applied electric field along the Z). (b) The index ellipse of the KD*P crystal corresponds to light propagating along the z direction. $\{XYZ\}$ is the crystalline principal dielectric frame which rotates into $\{xyz\}$ under an externally applied electric field [41].

A.1.1 Pockel cell function in PLEOM

Expanding over the brief outline in Section 2.4.4, I describe in more detail in this Appendix the purpose, working principle and function of a Pockels cell within our PLEOM setup.

The KD_2PO_4 (KD*P) nonlinear optical crystal was used in our Pockels cell, KD*P being an uniaxial crystal which the index ellipsoid reduced to an ellipse of revolution about the optic axis (Z) with $n_X = n_Y = n_o$ and $n_Z = n_e$. The optical indicatrix expression for the (KD*P) crystal is given by:

$$\frac{X^2}{n_o^2} + \frac{Y^2}{n_o^2} + \frac{Z^2}{n_e^2} = 1 \tag{A.1}$$

For a crystal abiding to $\bar{4}2m$ symmetry point group, the electrooptic coefficients

of the (KD*P) crystal reduce the following form:

$$[r] = \begin{bmatrix} 0 & 0 & 0 \\ 0 & 0 & 0 \\ 0 & 0 & 0 \\ r_{41} & 0 & 0 \\ 0 & r_{41} & 0 \\ 0 & 0 & r_{63} \end{bmatrix} \tag{A.2}$$

with $r_{41} = 8.8$ pm/V and $r_{63} = 26.4$ pm/V at the 0.5461 μm wavelength [41]. Under the application of an external electric field $\overrightarrow{E} = (\ 0 \quad 0 \quad E_Z\ )$ as in Fig. A.1a, the optical indicatrix expression A.1 is modified as:

$$\frac{X^2}{n_o^2} + \frac{Y^2}{n_o^2} + \frac{Z^2}{n_e^2} + 2r_{63}E_Z XY = 1 \tag{A.3}$$

Applying a 45° rotation about the Z axis, the new ellipse axis become x and y with

$$X = \frac{x-y}{\sqrt{2}}; \qquad Y = \frac{x+y}{\sqrt{2}} \qquad \text{and} \quad Z = z$$

and the ellipse equation now becomes:

$$\left(\frac{1}{n_o^2} + r_{63}E_z\right)x^2 + \left(\frac{1}{n_o^2} - r_{63}E_z\right)y^2 + \frac{z^2}{n_e^2} = 1 \tag{A.4}$$

which describes an ellipsoid in the new coordinate system xyz. Assuming a physically realistic value of $r_{63}E_z$ much smaller than 1, the new principal values of the refractive index are given by:

$$n_x = n_o - \frac{1}{2}n_o^3 r_{63}E_z \tag{A.5}$$

$$n_y = n_o + \frac{1}{2}n_o^3 r_{63}E_z \tag{A.6}$$

Under the application of an external electric field, the index ellipse of the crystal for light propagating along the z axis is reshaped from circular to elliptic as shown in Fig. A.1b. The variation of this refractive index in the new optical principal axis is proportional to the amplitude of the external electric field and depends only on the r_{63} electro-optical coefficient.

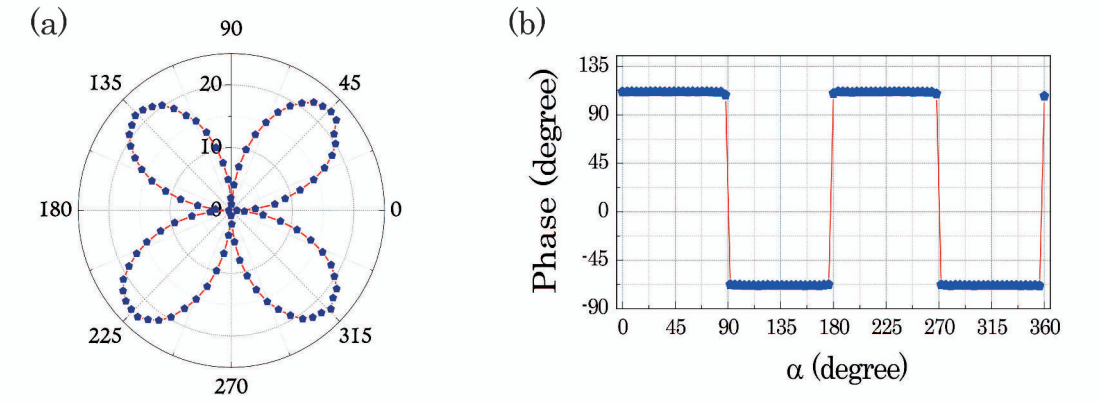

Figure A.2: Experimental intensity (a) and phase (b) of the polarization response from the Pockels cell under the application of a 10 mV AC Voltage at 20 kHz frequency measured by PLEOM. α is the angle of the polarization of the incident beam in the $\{XY\}$ plane. The magnitude of the electrooptic intensity is at the mV scale.

A.1.2 Application of Pockels cell in the PLEOM

We have used the Pockels cell as a reference back-up in our PLEOM set-up in view of its well known electro-optical parameters. More specifically, the Pockels electric signal from samples measured with a lock-in amplifier in PLEOM are converted into a retarded phase with an instrument dependent conversion ratio. Replacing the unknown sample by the Pockels cell and leaving other experimental conditions unchanged, allows to determine this coefficient. A Pockels cell normally works under the application of a DC high voltage such as towards Q-switching functions, whereas in our case, we have applied an AC voltage with a high frequency above the low frequency cut-off at 10 kHz. A prerequisite is therefore the characterization of the electrooptic effect from the Pockels cell under the application of an AC voltage.

Fig. A.2 displays the experimental intensity and phase of the polarized response from our Pockels cell. The polarization intensity exhibits four identical lobes with the maximal value at the angles corresponding to the new principal optical axis (after rotation by 45° from the initial one). The phase response (Fig. A.2b) exhibits an expected π shift discontinuity for different α intervals following sign changes of the effective electrooptic coefficient. These results are in good agreement with the

model presented in Section A.1.1.

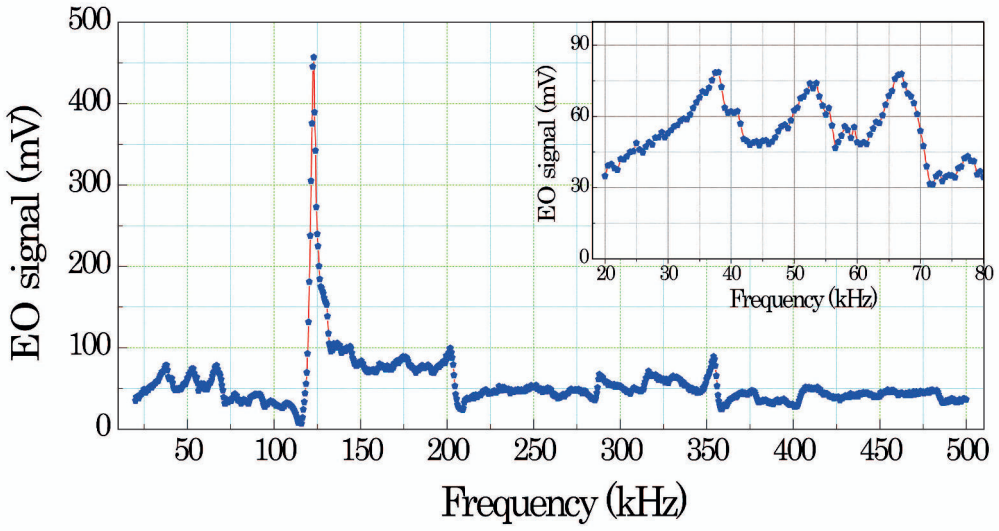

FIGURE A.3: Intensity of the electrooptic response from the Pockels cell under the application of a 10 mV AC voltage at frequencies ranging from 20 to 500 kHz. The incident beam propagates along the Z axis, whereas its polarization is along the rotated principal dielectric axis x at 45° from X within the $\{xy\}$ plane.

Fig. A.3 presents the dependence of the electrooptic response from our Pockels cell for a modulated frequency ranging from 20 to 500 kHz as determined by PLEOM. Our results are consistent with the experiment performed by Gerlach et al. who measured the electrooptic coefficient of KDP at high frequency [192]. Fig. A.3 exhibits the electrooptic retarded phase from the Pockels cell with respect to the modulated frequency. It exhibits different peaks, the highest one at a resonance frequency of 123.7 kHz. These variations originate from the frequency dispersion of crystalline deformations of various physical origins under the application of an AC electric field. The contribution of this deformation to the Pockels effect is captured in the following expression [184, 192]:

$$r_{ij}^{T} = r_{ij}^{S} + \sum_{k} p_{ik} d_{jk}, \text{ with } 1 \leqslant k \leqslant 6 \tag{A.7}$$

where r_{ij}^{T} is the total Pockels coefficient measured at constant stress (for a free crystal), r_{ij}^{S} the value measured at constant strain, p_{ik} the photoelastic coefficient and d_{jk} the piezoelectric coefficient.

Let us concentrate on the r_{63} coefficient, as given by:

$$r_{63}^{T} = r_{63}^{S} + p_{66}d_{36} \tag{A.8}$$

The frequency dependence of the photo-elastic and piezoelectric coefficients with respect to the external electric field leads to a variation of the total Pockels coefficient as measured by PLEOM and displayed in Fig. A.3. Until today, there is no report of a full investigation of the relation between the total Pockels coefficient of the KD*P crystal with the frequency of the externally applied electric field. This would require to measure a phase shift for light propagating along the Z axis of the crystal under the application of an AC voltage at a well defined frequency, allowing to infer the value of the r_{63}^{T} coefficient at this frequency via PLEOM. In the absence of such a facility, we can only at this stage use our Pockels cell to estimate the order of magnitude of the Pockels phase retardation from the measured electric signal by comparison with that from the KD*P crystal via the r_{63}^{T} coefficient in order with the well known r_{63}^{S} value (26.4 pm/V [41]).

A.2 Simulation of the scan along the x axis of a periodically poled KTP crystal

As briefly described in Section 4.4.1, we used a simple model in our simulation. We assume that the intersecting volume between the incident beam and the sample defines a conical volume as shown in Fig. A.4a. The height of this conical volume $h = 150$ µm is of the order of the depth of the crystal which is effectively penetrated by the external electric field.

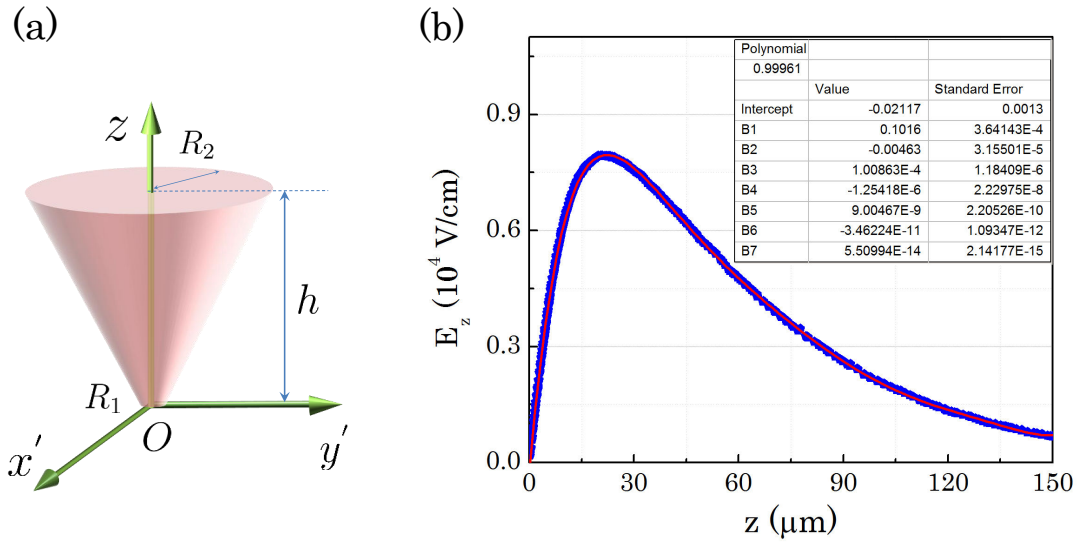

FIGURE A.4: (a) Simplification of the sample beam shape to a cone of height h. The radii of the section of the conical beam are R_1 and R_2 where R_1 is the size of the beam-waist which is of order of the wavelength of light, the $\{Ox'y'z\}$ frame defining coordinates for a conical shape. (b) z dependence of the E_z component from our COMSOL simulation(in blue) and fitted function represented by a red line.

The radius of the beam waist is given by:

$$R_1 = \frac{1.22\lambda}{2 \times \mathrm{NA}} \tag{A.9}$$

where $\lambda = 632.8$ nm and the numerical aperture NA $= 0.6$.

Whereas the upper radius R_2 is given by:

$$R_2 = \frac{\mathrm{NA}}{\sqrt{1 - \mathrm{NA}^2}} \times h + R_1 \tag{A.10}$$

At the z altitude, with conical section given by:

$$R = \frac{\mathrm{NA}}{\sqrt{1-\mathrm{NA}^2}} \times (z-h) + R_2 = \frac{\mathrm{NA}}{\sqrt{1-\mathrm{NA}^2}} \times z + R_1 \tag{A.11}$$

the sample beam follows within this plane a Gaussian radial function leading to a power density:

$$I(x^{'}, y^{'}, z) = I_0 f(z).e^{-\frac{2(x^{'2}+y^{'2})}{(R/2)^2}} \tag{A.12}$$

where I_0 is a constant and $f(z)$ is a function of z following $f(z) \sim 1/R^2$ so as to conversation of the total energy flux of the beam at different z positions.
Expression A.4 can then be re-expressed:

$$I(x^{'}, y^{'}, z) = I_0 \frac{1}{(R/2)^2}.e^{-\frac{2(x^{'2}+y^{'2})}{(R/2)^2}} \tag{A.13}$$

And now the $\mathrm{d}\overline{\alpha}_s$ in expression 4.9 can be replaced by:

$$\mathrm{d}\overline{\alpha}_s = \sqrt{I_0}\frac{2}{R}.e^{-\frac{x^{'2}+y^{'2}}{(R/2)^2}}\,\mathrm{d}x^{'}\mathrm{d}y^{'} \tag{A.14}$$

Whereas the $\overline{\Delta\varphi_j}$ in expression 4.12 is an integral along z with $E_z^{\Omega}(z)$ is evaluated by the fitted function from the simulation of the electric field as displayed in Fig. A.4b (one of the simulation results as given in Fig. 4.6b). The $E_z^{\Omega}(z)$ z dependence is expressed as:

$$\begin{aligned} E_z^{\Omega}(z) = &-21170.74 + 101601.6z - 4630.93z^2 + 100.86z^3 \\ &- 1.254z^4 + 0.009z^5 - 3.46.10^{-5}z^6 + 5.51.10^{-8}z^7 \end{aligned} \tag{A.15}$$

Expression 4.9 can be expressed as:

$$\overline{\Delta i} = -2\rho\overline{\alpha}_r\sqrt{I_0}\frac{\pi n_y^3}{\lambda}r_{23}\iiint \frac{2}{R}.e^{-\frac{x^{'2}+y^{'2}}{(R/2)^2}}E_z^{\Omega}(z)\mathrm{d}x^{'}\mathrm{d}y^{'}\mathrm{d}z \tag{A.16}$$

Which can be further simplified into:

$$\overline{\Delta i} = \alpha\iiint \frac{2}{R}.e^{-\frac{x^{'2}+y^{'2}}{(R/2)^2}}E_z^{\Omega}(z)\mathrm{d}x^{'}\mathrm{d}y^{'}\mathrm{d}z \tag{A.17}$$

where α is a proportionality factor.

As from Exp. A.17, the electrooptic signal is proportional to a volume integral within our quasi-conical beam approximation when the sample beam propagates through a single domain. In the more general case where the sample beam propagates through alternating domains, the conical volume has to be sliced into different portions corresponding to truncations by domains. The electrooptic signal for each truncated sections is calculated from Exp. A.17, the volume integration taking a positive value over a regular domain, and a negative one over an inverted domain. The overall electrooptic signal is obtained from the summation of integrals over the single-domain truncated cones.

A.3 Electric field mapping in three-dimensions

A quantitative electric field mapping method can be elaborated from our results in PLEOM based investigations of periodically poled KTP. In particular, we have evidenced in Figs. 4.13a and 4.14c the y dependence of the electric field which shows-up via the E_z contribution to the $r_{23}E_z$ product as from Exp. 4.12. Following the Pockels effect, which expresses the variation of the refractive index Δn of a nonlinear crystal upon application of an external electric field E_{ext}, PLEOM can be used to investigate nonlinear crystals starting now from a clear understanding of the external electric field. In such an inverse scheme, PLEOM can be used to map an unknown electric field including its three components and full orientation, when a well-known ferroelectric crystal is used as a probing medium.

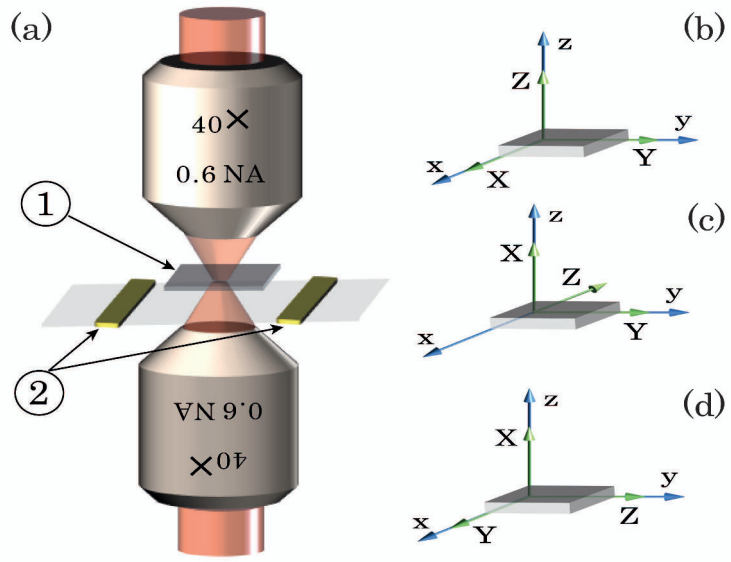

Figure A.5: (a) Scheme for the electric field mapping of PLEOM in which a well know probing crystal (1) is fixed at the beam waist of the sample beam whereas an electrode system (2) is mounted on a piezoelectric stage which allows to perform a 3D scan. (b), (c) and (d) are three different orientations of the probing crystal, corresponding to the detection of the E_z, E_x and E_y components respectively. $Oxyz$ is the laboratory frame and $OXYZ$ is the principal dielectric frame of the crystal.

The integral in expression 4.12 can be approximated by a local (x,y,z) dependent value when the thickness Δz along the z of the electro-optic media ensures that the

field variations across Δz can be neglected (i.e. $(\mathrm{d}E/\mathrm{d}z)\Delta z \ll E$), in other terms that the field can be assumed constant over the crystal thickness, thus allowing to reduce the integral to $rE\Delta z$. One can view this approach as a spatial variant of electro-optic sampling where the sampling medium is here a thin electro-optic film. It can be either an electro-optic polymer film or a single crystalline thin film such as from KTP, with the advantage in the former case of a smaller thickness in the micron range which can be readily obtained by spin-coating techniques over large surfaces, or even reduced to sub-micron thickness by controlled etching methods. In contrast, the thickness of crystalline ferroelectric samples can hardly be reduced below a few tens of microns under current fabrication techniques [193]. Indeed, the smaller the thickness of the electro-optic structure, the more valid the approximation of the phase accumulation integral by an averaged phase and hence, the higher the spatial resolution from slicing the electric field distribution along planes perpendicular to the film depth.

Following this direction, we propose a method for the electric field mapping by using PLEOM in the configuration shown in Fig. A.5a. In this configuration, a simple KTP crystal with a thickness of the order of a few micrometers is used as a probing crystal, which is set at the beamwaist of the sample beam. The sample beam propagates through the crystal along z. An electrode system is mounted on the surface of a piezoelectric stage, which allows to perform a scan in two- or three-dimensions.

- **E_z mapping**

  A Z-cut KTP crystal of thickness e in the range of a few micrometers is orientated as in Fig. A.5b. In this case $E_z = E_Z$. If the linear polarization of the sample beam is along the x (X), its electrooptic phase retardation is an integral along the optical path inside the crystal, given by:

  $$\Delta\varphi_X = \frac{\pi n_X^3}{\lambda}\int_0^e r_{13}E_Z \mathrm{d}l = \frac{\pi n_X^3}{\lambda} e r_{13}E_Z \tag{A.18}$$

  where the electrooptic coefficients r_{ij} is obtained from Table 3.2.

  In the other case, when the linear polarization of the sample beam is along

the y (Y) axis, its electrooptic phase retardation is given by:

$$\Delta\varphi_Y = \frac{\pi n_Y^3}{\lambda}\int_0^e r_{23}E_Z \mathrm{d}l = \frac{\pi n_Y^3}{\lambda} e r_{23}E_Z = \frac{\pi n_Y^3}{\lambda} e r_{23}E_z \tag{A.19}$$

Using PLEOM to measure the electrooptic phase retardation, the E_z component can then be inferred.

- **E_x mapping**

  In this case, a X-cut KTP crystal of similar thickness e is orientated as in Fig. A.5b leading to $E_x = -E_Z$. The sample beam propagates through the crystal along the z (X) axis, with its linear polarization along the x (Z) axis. The electrooptic phase retardation is then given by:

  $$\Delta\varphi_Z = \frac{\pi n_Z^3}{\lambda}\int_0^e r_{33}E_Z \mathrm{d}l = \frac{\pi n_Z^3}{\lambda} e r_{33}E_Z = -\frac{\pi n_Z^3}{\lambda} e r_{33}E_x \tag{A.20}$$

  Using PLEOM to measure the electrooptic phase retardation, the E_x component can be inferred.

- **E_y mapping**

  In this case, a X-cut KTP crystal with a similar multi-micron thickness e is orientated as in Fig. A.5c, with $E_y = E_Z$. The sample beam propagates through the crystal along the z (X) axis with its linear polarization along the y (Z) axis, the electrooptic phase retardation being given by:

  $$\Delta\varphi_Z = \frac{\pi n_Z^3}{\lambda}\int_0^e r_{33}E_Z \mathrm{d}l = \frac{\pi n_Z^3}{\lambda} e r_{33}E_Z = \frac{\pi n_Z^3}{\lambda} e r_{33}E_y \tag{A.21}$$

  Using PLEOM to measure the electrooptic phase retardation, the E_y component can be inferred, thus completing the full determination of the electric field components.

Fig. A.6 shows an example of the E_z mapping, as can be obtained from PLEOM. In this case, the amplitude and phase images achieved by PLEOM provide an image of the E_z component, including its magnitude and direction over the scanned zone. A 2D image of the E_x or E_y component also an be obtained likewise.

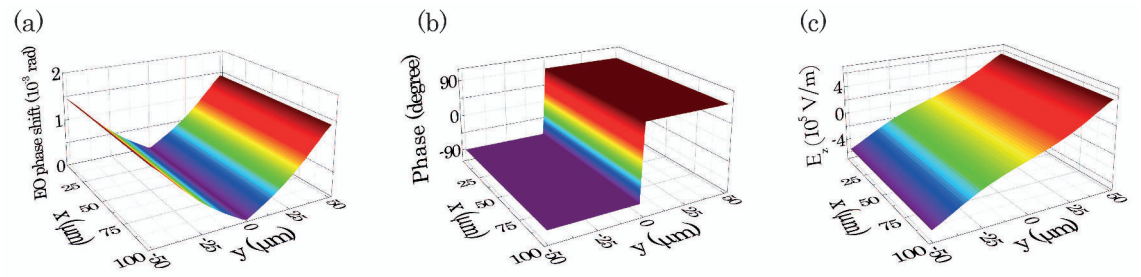

FIGURE A.6: Example of the E_z component mapping in the $\{xy\}$ plane, where E_z is a component of the electric field generated from two ribbon electrodes as shown in Fig. A.5a. (a) Simulated amplitude and (b) phase images by PLEOM and (c) 2D image of the E_z component as a result from (a) and (b).

Along similar lines, one can also envision to set an electrooptic nano-probe with well known orientation (that can be determined by PLEOM as in the case of the single KTP nano-crystal) at the focal point of the objectives, while the position of the planar electrode structure is being displaced by a piezoelectric mount to various positions, allowing the nano-particle to sense different values of the electric field.

A.4 Application of PLEOM to biological samples

Nowadays, a growing number of research results primarily generated in physics or chemistry, tend to be spun-off to biological studies. In order to investigate biological samples, non-invasive methods (non-destructive methods) have been in high demand towards the study of living tissues.

Membranes, such as lipid bilayers play an essential role as barriers which protect the cell and their intracellular organelles. The ion concentration gradients between the internal and external solutions of the membrane maintain an equilibrium potential which controls the exchange process between cells and their external environment. Various experimental methods have been used to stimulate and measure this potential, among which patch-clamp technique is the best known [194–196]. Other methods are based on voltage sensitive fluorescence probes [197] and more recently, an adaptation of the electric field induced second-harmonic generation method [98, 99, 101]. Building-up on its non-invasive character and the very low intensity level of the illumination beam that is required (typically less than 10% of a 1.5 mW laser beam from a CW He-Ne laser), PLEOM stands out as a most promising candidate to investigate biological samples. This direction has been followed since the previous doctoral thesis [67], starting with the imaging of dye-doped artificial lipidic membranes [2].

In the wake of this previous study, our new goal was to use PLEOM in order to measure the membrane potential. Let us start by discussing the case of lipid bilayers stained by nonlinear molecules. The effective susceptibility for second-order nonlinear molecules in the present of a static electric field (membrane potential) is given by [198]:

$$\chi^{'(2)} = \chi^{(2)} + \chi^{(3)} E_m \tag{A.22}$$

where $\chi^{'(2)}$ is the effective second-order susceptibility and E_m is the membrane electric field.

The third-rank second-order nonlinear susceptibility tensor $\chi^{'(2)}_{ijk}$ is linked to the

Pockels electro-optical tensor r_{ijk} by the following relation:

$$r'_{ijk}(-\omega;\omega,0) = -\frac{2}{\epsilon_{ii}\epsilon_{jj}}\chi'^{(2)}_{ijk}(-\omega;\omega,0) \tag{A.23}$$

Exps. A.22 and A.23 exhibit a linear dependency of the effective Pockels coefficient r'_{ijk} with respect to the membrane electric field E_m.

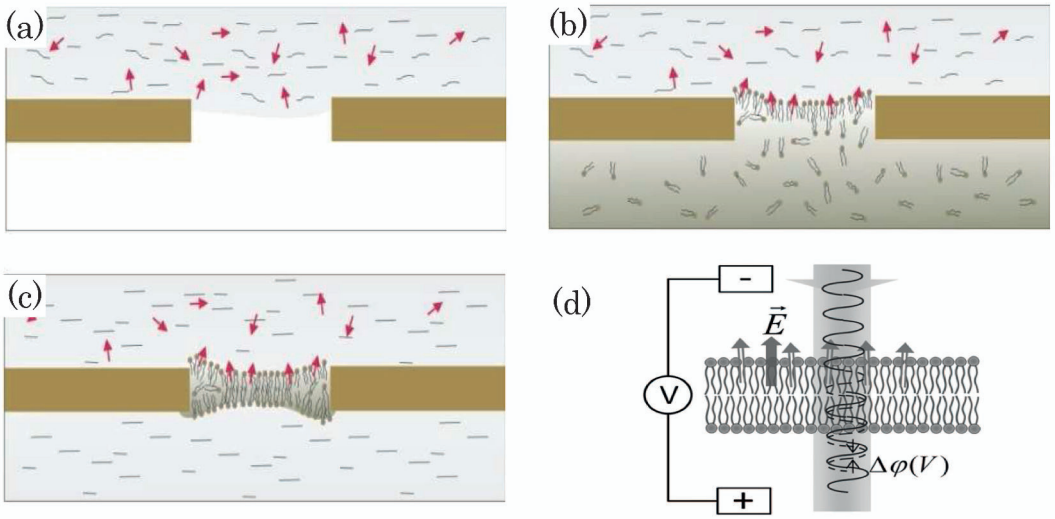

FIGURE A.7: Steps of bilayer formation such as (a) insertion of the buffer and the dye (red arrows) in the upper channel; (b) injection of the lipid into the lower channel; (c) injection of the buffer solution in the lower channel and formation of the bilayer [67]. (d) Principle of probing the electrooptic effect of a one-side dye-doped membrane [2].

In this study, artificial lipidic bilayers were used as a model for the lipid matrix in biological cell membranes. A lipid bilayer is prepared in a biochip through three main steps as shown in Fig. A.7. Firstly, 15 ml of a buffer solution with 0.1 M KCl and 10 mM of 3-(*n*-morpholino)propane sulfonic acid (MOPS) at pH7 stained with Di-8-ANEPPS dye molecules, is inserted in the upper chamber (Fig. A.7a). An 8 ml liped solution prepared from the dissolution of L-α-phosphatidylcholine (Egg chicken, Avanti Polar Lipids) with 20 mg/ml in decane, is injected in the lower channel, leading to the build-up of the first lipid layer as depicted in Fig. A.7b. In the next step, 30 ml of a buffer solution is injected in the lower channel. The second lipid layer is then formed as in Fig. A.7c. Following this three step recipe, we tried to prepare lipid bilayers for our study, but the rate of success of the process

was below 10%. In order to investigate the best condition for this preparation, all parameters such as the quality of the buffer solution, lipid and biochip, and the protocol were studied carefully. In particular, we found that the buffer and lipid solutions need to be kept in an oven at 35° C during at least 15 minute before usage, allowing to reach under these improved conditions, a success rate surpassing than 90%.

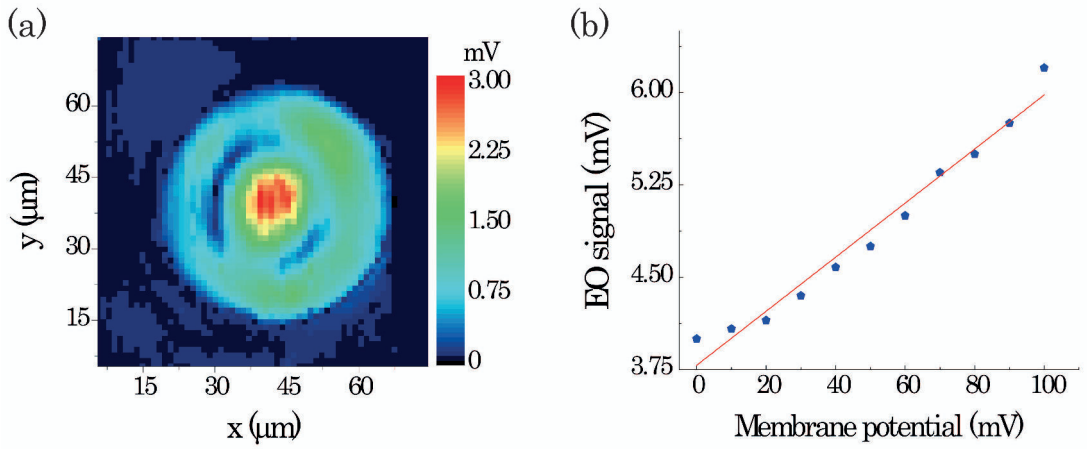

Figure A.8: (a) Amplitude of the spatial electrooptic response of a lipid bilayer stained by Di-8-ANEPPS dye molecules. (b) Dependence of the magnitude of the electrooptic response from a dropped lipid bilayer with respect to the DC voltage mimicking the membrane potential. Blue dots are the experimental data from PLEOM and the red line is a linear fit.

Fig. A.8a shows the spatial electrooptic response in amplitude over a large area under a 500 mV peak-to-peak sinusoidal voltage at a 20 kHz modulation frequency. The lipid bilayer can be clearly identified from the high amplitude of the electrooptic response from the Di-8-ANEPPS dye molecules, with a 50 μm membrane size in excellent agreement with the diameter of the supporting hole in the biochip.

In order to study the dependence of the electrooptic response from the dye molecules which are staining the first lipid layer of the membrane with respect to the membrane potential, a DC voltage is applied to the lipid bilayer, thus mimicking a membrane potential. The relation between the electrooptic response from the dye molecules and the artificial membrane potential was investigated by varying the DC

voltage from 0 to 100 mV in the same magnitude range as for natural membrane potential (e.g. 60 mV). Fig. A.8 shows the first observation of this dependence, whereby the electrooptic response from the dye can be considered as a linear function of the applied DC voltage, in agreement with Exp. A.23.

Due to the time constraints of this thesis work, I can only report here what may be considered as the demonstration of a new PLEOM based methodology to image and investigate the membrane potential in a non-invasive method at a very low level of illumination.

References

[1] T. Toury, S. Brasselet, and J. Zyss. *Electro-optical microscopy: mapping nonlinear polymer films with micrometric resolution.* Optics letters **31**(10), 1468 (2006). vi, viii, 12, 57

[2] B. Hajj, S. De Reguardati, L. Hugonin, B. Le Pioufle, T. Osaki, H. Suzuki, S. Takeuchi, H. Mojzisova, D. Chauvat, and J. Zyss. *Electro-optical imaging microscopy of dye-doped artificial lipidic membranes.* Biophysical journal **97**(11), 2913 (2009). vi, viii, 57, 139, 140

[3] B. Hajj, S. Perruchas, J. Lautru, G. Dantelle, T. Gacoin, J. Zyss, and D. Chauvat. *Electro-optical pockels scattering from a single nanocrystal.* Optics express **19**(10), 9000 (2011). vi, viii, 57, 67, 80

[4] P. A. Franken, A. E. Hill, C. W. Peters, and G. Weinreich. *Generation of optical harmonics.* Phys. Rev. Lett. **7**, 118 (1961). 2, 54, 56

[5] T. H. Maiman. *Stimulated optical radiation in ruby* (1960). 2

[6] D. Kleinman. *Theory of second harmonic generation of light.* Physical Review **128**(4), 1761 (1962). 2, 4

[7] D. A. Kleinman. *Nonlinear dielectric polarization in optical media.* Phys. Rev. **126**, 1977 (1962). 3, 4, 7

[8] J. Giordmaine. *Mixing of light beams in crystals.* Physical Review Letters **8**(1), 19 (1962). 3

[9] P. Maker, R. Terhune, M. Nisenoff, and C. Savage. *Effects of dispersion and focusing on the production of optical harmonics.* Physical Review Letters **8**(1), 21 (1962). 3, 7

[10] J. Armstrong, N. Bloembergen, J. Ducuing, and P. Pershan. *Interactions between light waves in a nonlinear dielectric.* Physical Review **127**(6), 1918 (1962). 3, 7, 82, 106

[11] D. Jundt, G. Magel, M. Fejer, and R. Byer. *Periodically poled linbo3 for high-efficiency second-harmonic generation.* Applied physics letters **59**(21), 2657 (1991). 3, 7, 8, 13, 82, 106

[12] V. Berger. *Nonlinear photonic crystals.* Physical review letters **81**(19), 4136 (1998). 3, 106

[13] C. C. Wang and G. W. Racette. *Measurement of parametric gain accompanying optical difference frequency generation.* Applied Physics Letters **6**(8), 169 (1965). 3

[14] J. A. Giordmaine and R. C. Miller. *Tunable coherent parametric oscillation in linbo$_3$ at optical frequencies.* Phys. Rev. Lett. **14**, 973 (1965). 3

[15] S. E. Harris. *Tunable optical parametric oscillators.* Tech. rep., DTIC Document (1970). 3

[16] S. Harris. *Method to lock an optical parametric oscillator to an atomic transition.* Applied Physics Letters **14**(11), 335 (1969). 3

[17] M. Barbieri, F. De Martini, G. Di Nepi, P. Mataloni, G. M. D'Ariano, and C. Macchiavello. *Detection of entanglement with polarized photons: Experimental realization of an entanglement witness.* Phys. Rev. Lett. **91**, 227901 (2003). 3

[18] C. Cinelli, M. Barbieri, R. Perris, P. Mataloni, and F. D. Martini. *All-versus-nothing nonlocality test of quantum mechanics by two-photon hyperentanglement.* Phys. Rev. Lett. **95**, 240405 (2005). 3

[19] S. Kurtz and T. Perry. *A powder technique for the evaluation of nonlinear optical materials.* Journal of Applied Physics **39**(8), 3798 (1968). 4

[20] P. Rentzepis and Y.-H. Pao. *Laser-induced optical second harmonic generation in organic crystals.* Applied Physics Letters **5**(8), 156 (1964). 4

[21] J. Gott. *Effect of molecular structure on optical second-harmonic generation from organic crystals.* Journal of Physics B: Atomic and Molecular Physics **4**(1), 116 (1971). 4

[22] J. Zyss. *Molecular nonlinear optics: materials, physics, and devices*, vol. 260 (Academic press Boston, 1994). 4

[23] J. Nicoud, R. Twieg, D. Chemla, and J. Zyss. *Nonlinear optical properties of organic molecules and crystals.* Academic Press, London (1987). 4

[24] C.-F. Sun, C.-L. Hu, X. Xu, J.-B. Ling, T. Hu, F. Kong, X.-F. Long, and J.-G. Mao. *Banbo (io3) 5: A new polar material with a very large shg response.* Journal of the American Chemical Society **131**(27), 9486 (2009). 4

[25] D. Frattarelli, M. Schiavo, A. Facchetti, M. A. Ratner, and T. J. Marks. *Self-assembly from the gas-phase: design and implementation of small-molecule chromophore precursors with large nonlinear optical responses.* Journal of the American Chemical Society **131**(35), 12595 (2009).

[26] I. Asselberghs, C. Flors, L. Ferrighi, E. Botek, B. Champagne, H. Mizuno, R. Ando, A. Miyawaki, J. Hofkens, M. V. d. Auweraer, *et al. Second-harmonic generation in gfp-like proteins.* Journal of the American Chemical Society **130**(46), 15713 (2008).

[27] B. Babgi, L. Rigamonti, M. P. Cifuentes, T. C. Corkery, M. D. Randles, T. Schwich, S. Petrie, R. Stranger, A. Teshome, I. Asselberghs, *et al. Length-dependent convergence and saturation behavior of electrochemical, linear optical, quadratic nonlinear optical, and cubic nonlinear optical properties of dipolar alkynylruthenium complexes with oligo (phenyleneethynylene) bridges.* Journal of the American Chemical Society **131**(29), 10293 (2009). 4

[28] P. Czarnecki, W. Nawrocik, Z. Pajak, and J. Wasicki. *Ferroelectric properties of pyridinium perchlorate.* Journal of Physics: Condensed Matter **6**(26), 4955 (1994). 4

[29] P. Czarnecki, W. Nawrocik, Z. Pajak, and J. Wasicki. *Ferroelectric properties of pyridinium tetrafluoroborate.* Physical Review B **49**(2), 1511 (1994). 4

[30] P. Innocenzi and B. Lebeau. *Organic–inorganic hybrid materials for non-linear optics.* Journal of Materials Chemistry **15**(35-36), 3821 (2005). 4

[31] M. Wojtaś, A. Bil, R. Jakubas, A. Gagor, A. Pietraszko, O. Czupiński, Z. Tylczyński, and D. Isakov. *Organic-inorganic compounds with strong nonlinear optical properties based on 2, 4, 6-trimethylpyridinium and tetrahedral bf 4-networks.* Physical Review B **83**(14), 144103 (2011).

[32] E. Cariati, R. Macchi, D. Roberto, R. Ugo, S. Galli, N. Casati, P. Macchi, A. Sironi, L. Bogani, A. Caneschi, *et al. Polyfunctional inorganic-organic hybrid materials: An unusual kind of nlo active layered mixed metal oxalates with tunable magnetic properties and very large second harmonic generation.* Journal of the American Chemical Society **129**(30), 9410 (2007). 4

[33] G. Heilmeier, N. Ockman, R. Braunstein, and D. Kramer. *Relationship between optical second harmonic generation and the electro-optic effect in the molecular crystal hexamine.* Applied Physics Letters **5**(11), 229 (1964). 4

[34] R. Hellwarth and P. Christensen. *Nonlinear optical microscopic examination*

of structure in polycrystalline znse. Optics Communications **12**(3), 318 (1974). 5

[35] R. Hellwarth and P. Christensen. *Nonlinear optical microscope using second harmonic generation*. Applied optics **14**(2), 247 (1975). 5

[36] I. Freund, M. Deutsch, and A. Sprecher. *Connective tissue polarity. optical second-harmonic microscopy, crossed-beam summation, and small-angle scattering in rat-tail tendon*. Biophysical journal **50**(4), 693 (1986). 5

[37] B. E. Cohen. *Biological imaging: Beyond fluorescence*. Nature **467**(7314), 407 (2010). 5

[38] P. Pantazis, J. Maloney, D. Wu, and S. E. Fraser. *Second harmonic generating (shg) nanoprobes for in vivo imaging*. Proceedings of the National Academy of Sciences **107**(33), 14535 (2010). 5, 123

[39] M. M. Fejer, G. Magel, D. H. Jundt, and R. L. Byer. *Quasi-phase-matched second harmonic generation: tuning and tolerances*. Quantum Electronics, IEEE Journal of **28**(11), 2631 (1992). 5, 6, 8

[40] A. Arie and N. Voloch. *Periodic, quasi-periodic, and random quadratic nonlinear photonic crystals*. Laser & Photonics Reviews **4**(3), 355 (2010). 5, 6, 7, 8, 83, 87, 104, 106

[41] R. W. Boyd. *Nonlinear optics* (Academic press, 2003). 6, 17, 28, 29, 59, 60, 74, 80, 111, 127, 128, 131

[42] G. D. Miller. *Periodically poled lithium niobate: modeling, fabrication, and nonlinear-optical performance*. Ph.D. thesis, Stanford University (1998). 8, 107, 108

[43] C. Sheppard, J. Gannaway, R. Kompfner, and D. Walsh. *The scanning harmonic optical microscope*. Quantum Electronics, IEEE Journal of **13**(9), 912 (1977). 8

[44] C. Sheppard and R. Kompfner. *Resonant scanning optical microscope.* Applied optics **17**(18), 2879 (1978).

[45] J. Gannaway and C. Sheppard. *Second-harmonic imaging in the scanning optical microscope.* Optical and Quantum Electronics **10**(5), 435 (1978). 8

[46] P. Pantazis, J. Maloney, D. Wu, and S. E. Fraser. *Second harmonic generating (shg) nanoprobes for in vivo imaging.* Proceedings of the National Academy of Sciences **107**(33), 14535 (2010). 10, 11, 123

[47] W. Denk, J. H. Strickler, and W. W. Webb. *Two-photon laser scanning fluorescence microscopy.* Science **248**(4951), 73 (1990). 9

[48] W. P. Dempsey, S. E. Fraser, and P. Pantazis. *Shg nanoprobes: Advancing harmonic imaging in biology.* BioEssays **34**(5), 351 (2012). 11, 123

[49] C.-L. Hsieh, R. Grange, Y. Pu, and D. Psaltis. *Three-dimensional harmonic holographic microcopy using nanoparticles as probes for cell imaging.* Optics express **17**(4), 2880 (2009). 11, 56

[50] E. V. Rodriguez, C. B. de Araújo, A. M. Brito-Silva, V. Ivanenko, and A. Lipovskii. *Hyper-rayleigh scattering from batio 3 and pbtio 3 nanocrystals.* Chemical Physics Letters **467**(4), 335 (2009). 11

[51] A. V. Kachynski, A. N. Kuzmin, M. Nyk, I. Roy, and P. N. Prasad. *Zinc oxide nanocrystals for nonresonant nonlinear optical microscopy in biology and medicine.* The Journal of Physical Chemistry C **112**(29), 10721 (2008). 11

[52] J. C. Johnson, H. Yan, R. D. Schaller, P. B. Petersen, P. Yang, and R. J. Saykally. *Near-field imaging of nonlinear optical mixing in single zinc oxide nanowires.* Nano Letters **2**(4), 279 (2002). 11

[53] L. Bonacina, Y. Mugnier, F. Courvoisier, R. Le Dantec, J. Extermann,

Y. Lambert, V. Boutou, C. Galez, and J.-P. Wolf. *Polar fe (io3) 3 nanocrystals as local probes for nonlinear microscopy.* Applied Physics B **87**(3), 399 (2007). 11, 56, 76

[54] J. Extermann, L. Bonacina, E. Cuña, C. Kasparian, Y. Mugnier, T. Feurer, and J.-P. Wolf. *Nanodoublers as deep imaging markers for multi-photon microscopy.* Optics express **17**(17), 15342 (2009). 11

[55] L. Le Xuan, C. Zhou, A. Slablab, D. Chauvat, C. Tard, S. Perruchas, T. Gacoin, P. Villeval, and J.-F. Roch. *Photostable second-harmonic generation from a single ktiopo4 nanocrystal for nonlinear microscopy.* Small **4**(9), 1332 (2008). 11, 56, 67, 72, 76

[56] N. Sandeau, L. Le Xuan, D. Chauvat, C. Zhou, J.-F. Roch, and S. Brasselet. *Defocused imaging of second harmonic generation from a single nanocrystal.* Optics express **15**(24), 16051 (2007). 56

[57] L. Le Xuan, S. Brasselet, F. Treussart, J.-F. Roch, F. Marquier, D. Chauvat, S. Perruchas, C. Tard, and T. Gacoin. *Balanced homodyne detection of second-harmonic generation from isolated subwavelength emitters.* Applied physics letters **89**(12), 121118 (2006). 56, 57, 67

[58] L. Mayer, A. Slablab, G. Dantelle, V. Jacques, A.-M. Lepagnol-Bestel, S. Perruchas, P. Spinicelli, A. Thomas, D. Chauvat, M. Simonneau, *et al. Single ktp nanocrystals as second-harmonic generation biolabels in cortical neurons.* Nanoscale **5**(18), 8466 (2013). 11, 55, 56, 70, 72, 76, 123

[59] E. M. Rodriguez, A. Speghini, F. Piccinelli, L. Nodari, M. Bettinelli, D. Jaque, and J. G. Solé. *Multicolour second harmonic generation by strontium barium niobate nanoparticles.* Journal of Physics D: Applied Physics **42**(10), 102003 (2009). 11

[60] Y. Nakayama, P. J. Pauzauskie, A. Radenovic, R. M. Onorato, R. J. Saykally,

J. Liphardt, and P. Yang. *Tunable nanowire nonlinear optical probe.* Nature **447**(7148), 1098 (2007). 11, 56

[61] M. Zielinski, D. Oron, D. Chauvat, and J. Zyss. *Second-harmonic generation from a single core/shell quantum dot.* Small **5**(24), 2835 (2009). 11, 124

[62] M. Zielinski, S. Winter, R. Kolkowski, C. Nogues, D. Oron, J. Zyss, and D. Chauvat. *Nanoengineering the second order susceptibility in semiconductor quantum dot heterostructures.* Optics express **19**(7), 6657 (2011). 11, 55, 56, 67, 72, 76

[63] G. W. Bryant and A. Liu. *Second-harmonic generation of semiconductor quantum dots studied by near-field optical microscopy.* Superlattices and microstructures **25**(1), 361 (1999). 11

[64] N. Thantu. *Second harmonic generation and two-photon luminescence upconversion in glasses doped with znse nanocrystalline quantum dots.* Journal of luminescence **111**(1), 17 (2005). 11

[65] M. R. Singh. *Enhancement of the second-harmonic generation in a quantum dot–metallic nanoparticle hybrid system.* Nanotechnology **24**(12), 125701 (2013). 11

[66] T. Toury. *La microscopie électro-optique Etude, conception, applications.* Ph.D. thesis, École normale supérieure de Cachan-ENS Cachan (2005). 12, 17, 38, 122

[67] B. Hajj. *Imagerie électro-optique Pockels aux échelles micro et nanométriques en physique et biophysique.* Ph.D. thesis, École normale supérieure de Cachan-ENS Cachan (2010). 12, 17, 38, 80, 122, 139, 140

[68] Y. Sheng, A. Best, H.-J. Butt, W. Krolikowski, A. Arie, and K. Koynov. *Three-dimensional ferroelectric domain visualization by čerenkov-type second harmonic generation.* Optics express **18**(16), 16539 (2010). 13, 85, 104, 107, 108

[69] K. Kalinowski, V. Roppo, Q. Kong, Y. Sheng, and W. Krolikowski. *Čerenkov second harmonic generation in nonlinear crystals.* In *Conference on Lasers and Electro-Optics/Pacific Rim*, p. C371 (2011).

[70] Y. Sheng, V. Roppo, M. Ren, K. Kalinowski, C. Cojocaru, J. Trull, Z. Li, K. Koynov, and W. Krolikowski. *Multi-directional čerenkov second harmonic generation in two-dimensional nonlinear photonic crystal.* Optics express **20**(4), 3948 (2012).

[71] T. Kämpfe, P. Reichenbach, M. Schröder, A. Haußmann, L. Eng, T. Woike, and E. Soergel. *Optical three-dimensional profiling of charged domain walls in ferroelectrics by cherenkov second-harmonic generation.* Physical Review B **89**(3), 035314 (2014). 13, 85, 107

[72] M. C. Teich and B. Saleh. *Fundamentals of photonics.* Canada, Wiley Interscience p. 3 (1991). 17, 22, 26, 29, 30, 31, 34

[73] M. Minsky. *Microscopy apparatus* (1961). US Patent 3,013,467. 17, 18

[74] S. J. Wright and D. J. Wright. *Introduction to confocal microscopy.* Cell Biological Applications of Confocal Microscopy, in Methods in Cell Biology **70**, 1 (2002).

[75] N. Lagali. *Confocal Laser Microscopy - Principles and Applications in Medicine, Biology, and the Food Sciences* (InTech, 2013).

[76] N. S. Claxton, T. J. Fellers, and M. W. Davidson. *Laser scanning confocal microscopy.* Department of Optical Microscopy and Digital Imaging, Florida State University, Tallahassee (2006). 17, 19

[77] E. Abbe. *ZEITSCHRIFT FUR INSTRUMENTENKUNDE.* (1881). 20

[78] K. Zetie, S. Adams, and R. Tocknell. *How does a mach-zehnder interferometer work?* Physics Education **35**(1), 46 (2000). 20

[79] P. Hariharan. *Basics of interferometry* (Academic Press, 2010). 20, 22

[80] M. G. A. Paris. *Entanglement and visibility at the output of a mach-zehnder interferometer*. Phys. Rev. A **59**, 1615 (1999). 23

[81] G. Haack, H. Förster, and M. Büttiker. *Parity detection and entanglement with a mach-zehnder interferometer*. Phys. Rev. B **82**, 155303 (2010). 23

[82] T. A. Maldonado and T. K. Gaylord. *Electrooptic effect calculations: simplified procedure for arbitrary cases*. Applied optics **27**(24), 5051 (1988). 29

[83] F. Agulló-López and J. M. Cabrera. *Electrooptics: phenomena, materials and applications*, vol. 1 (Academic Press, 1994). 31, 32

[84] C. Joo, H. Balci, Y. Ishitsuka, C. Buranachai, and T. Ha. *Advances in single-molecule fluorescence methods for molecular biology*. Annual Review of Biochemistry **77**(1), 51 (2008). 54

[85] F. Pinaud, S. Clarke, A. Sittner, and M. Dahan. *Probing cellular events, one quantum dot at a time*. Nature methods **7**(4), 275 (2010). 54

[86] V. Rombach-Riegraf, P. Oswald, R. Bienert, J. Petersen, M. Domingo, J. Pardo, P. Gräber, and E. Galvez. *Blinking effect and the use of quantum dots in single molecule spectroscopy*. Biochemical and biophysical research communications **430**(1), 260 (2013). 54

[87] Y.-R. Chang, H.-Y. Lee, K. Chen, C.-C. Chang, D.-S. Tsai, C.-C. Fu, T.-S. Lim, Y.-K. Tzeng, C.-Y. Fang, C.-C. Han, *et al. Mass production and dynamic imaging of fluorescent nanodiamonds*. Nature nanotechnology **3**(5), 284 (2008). 54

[88] X. Brokmann, J.-P. Hermier, G. Messin, P. Desbiolles, J.-P. Bouchaud, and M. Dahan. *Statistical aging and nonergodicity in the fluorescence of single nanocrystals*. Phys. Rev. Lett. **90**, 120601 (2003). 54

[89] X. Wang, X. Ren, K. Kahen, M. A. Hahn, M. Rajeswaran, S. Maccagnano-Zacher, J. Silcox, G. E. Cragg, A. L. Efros, and T. D. Krauss. *Non-blinking semiconductor nanocrystals*. Nature **459**(7247), 686 (2009). 54

[90] X. Brokmann, M.-V. Ehrensperger, J.-P. Hermier, A. Triller, and M. Dahan. *Orientational imaging and tracking of single cdse nanocrystals by defocused microscopy.* Chemical physics letters **406**(1), 210 (2005). 55

[91] B. Vohnsen, S. I. Bozhevolnyi, K. Pedersen, J. Erland, J. R. Jensen, and J. M. Hvam. *Second-harmonic scanning optical microscopy of semiconductor quantum dots.* Optics communications **189**(4), 305 (2001). 55

[92] C. Anceau, S. Brasselet, and J. Zyss. *Local orientational distribution of molecular monolayers probed by nonlinear microscopy.* Chemical physics letters **411**(1), 98 (2005). 56, 76

[93] V. Le Floc'h, S. Brasselet, J.-F. Roch, and J. Zyss. *Monitoring of orientation in molecular ensembles by polarization sensitive nonlinear microscopy.* The Journal of Physical Chemistry B **107**(45), 12403 (2003). 56, 76

[94] R. Jin, J. E. Jureller, H. Y. Kim, and N. F. Scherer. *Correlating second harmonic optical responses of single ag nanoparticles with morphology.* Journal of the American Chemical Society **127**(36), 12482 (2005). 56

[95] A. Slablab, L. Le Xuan, M. Zielinski, Y. de Wilde, V. Jacques, D. Chauvat, and J.-F. Roch. *Second-harmonic generation from coupled plasmon modes in a single dimer of gold nanospheres.* Optics express **20**(1), 220 (2012). 56

[96] R. Gauderon, P. Lukins, and C. Sheppard. *Three-dimensional second-harmonic generation imaging with femtosecond laser pulses.* Optics letters **23**(15), 1209 (1998). 56

[97] S. Brasselet, V. Le Floch, F. Treussart, J.-F. Roch, J. Zyss, E. Botzung-Appert, and A. Ibanez. *In situ diagnostics of the crystalline nature of single organic nanocrystals by nonlinear microscopy.* Physical review letters **92**(20), 207401 (2004). 56, 76

[98] L. Moreaux, O. Sandre, and J. Mertz. *Membrane imaging by second-harmonic generation microscopy.* JOSA B **17**(10), 1685 (2000). 56, 139

[99] L. Moreaux, T. Pons, V. Dambrin, M. Blanchard-Desce, and J. Mertz. *Electro-optic response of second-harmonic generation membrane potential sensors.* Optics letters **28**(8), 625 (2003). 139

[100] S. Schürmann, F. Von Wegner, R. H. Fink, O. Friedrich, and M. Vogel. *Second harmonic generation microscopy probes different states of motor protein interaction in myofibrils.* Biophysical journal **99**(6), 1842 (2010).

[101] R. Grange, T. Lanvin, C.-L. Hsieh, Y. Pu, and D. Psaltis. *Imaging with second-harmonic radiation probes in living tissue.* Biomedical optics express **2**(9), 2532 (2011). 139

[102] W. P. Dempsey, S. E. Fraser, and P. Pantazis. *Shg nanoprobes: Advancing harmonic imaging in biology.* BioEssays **34**(5), 351 (2012). 56, 123

[103] K. Kato and E. Takaoka. *Sellmeier and thermo-optic dispersion formulas for ktp.* Applied optics **41**(24), 5040 (2002). 57, 59

[104] J. D. Bierlein and H. Vanherzeele. *Potassium titanyl phosphate: properties and new applications.* JOSA B **6**(4), 622 (1989). 57, 58, 59, 60

[105] J. Bierlein and C. Arweiler. *Electro-optic and dielectric properties of ktiopo4.* Applied physics letters **49**(15), 917 (1986). 57, 60

[106] C. A. Ebbers and S. P. Velsko. *High average power ktiopo4 electro-optic q-switch.* Applied physics letters **67**(5), 593 (1995). 57

[107] X. Wang, P. Basseras, R. D. Miller, and H. Vanherzeele. *Investigation of ktiopo4 as an electro-optic amplitude modulator.* Applied physics letters **59**(5), 519 (1991). 57

[108] J. Valasek. *Piezo-electric and allied phenomena in rochelle salt.* Phys. Rev. **17**, 475 (1921). 82

[109] E. Soergel. *Visualization of ferroelectric domains in bulk single crystals.* Applied Physics B **81**(6), 729 (2005). 82, 84, 85, 86

[110] T. Hidaka, T. Maruyama, M. Saitoh, N. Mikoshiba, M. Shimizu, T. Shiosaki, L. Wills, R. Hiskes, S. Dicarolis, and J. Amano. *Formation and observation of 50 nm polarized domains in pbzr1- xtixo3 thin film using scanning probe microscope.* Applied physics letters **68**(17), 2358 (1996). 82

[111] Y. Cho, K. Fujimoto, Y. Hiranaga, Y. Wagatsuma, A. Onoe, K. Terabe, and K. Kitamura. *Tbit/inch2 ferroelectric data storage based on scanning nonlinear dielectric microscopy.* Applied physics letters **81**(23), 4401 (2002). 82

[112] R. Cudney, L. Ríos, and H. Escamilla. *Electrically controlled fresnel zone plates made from ring-shaped 180 domains.* Optics express **12**(23), 5783 (2004). 82

[113] M. M. Fejer, G. Magel, D. H. Jundt, and R. L. Byer. *Quasi-phase-matched second harmonic generation: tuning and tolerances.* Quantum Electronics, IEEE Journal of **28**(11), 2631 (1992). 82, 106

[114] M. Yamada, N. Nada, M. Saitoh, and K. Watanabe. *First-order quasi-phase matched linbo3 waveguide periodically poled by applying an external field for efficient blue second-harmonic generation.* Applied Physics Letters **62**(5), 435 (1993). 82, 83, 87

[115] A. Arie, G. Rosenman, V. Mahal, A. Skliar, M. Oron, M. Katz, and D. Eger. *Green and ultraviolet quasi-phase-matched second harmonic generation in bulk periodically-poled ktiopo¡ sub¿ 4¡/sub¿.* Optics communications **142**(4), 265 (1997). 83

[116] H. Karlsson, F. Laurell, and L. Cheng. *Periodic poling of rbtiopo4 for quasi-phase matched blue light generation.* Applied physics letters **74**(11), 1519 (1999).

[117] S. Wang, V. Pasiskevicius, F. Laurell, H. Karlsson, *et al. First-order type ii quasi-phase-matched uv generation in periodically poled ktp.* Optics letters **24**(14), 978 (1999).

[118] X. Mu and Y. J. Ding. *Efficient third-harmonic generation in partly periodically poled ktiopo¡ sub¿ 4¡/sub¿ crystal.* Optics letters **26**(9), 623 (2001).

[119] V. Pasiskevicius, S. Holmgren, S. Wang, and F. Laurell. *Simultaneous second-harmonic generation with two orthogonal polarization states in periodically poled ktp.* Optics letters **27**(18), 1628 (2002).

[120] R. C. Pooser and O. Pfister. *Observation of triply coincident nonlinearities in periodically poled ktiopo4.* Optics letters **30**(19), 2635 (2005).

[121] C. Canalias, V. Pasiskevicius, M. Fokine, and F. Laurell. *Backward quasi-phase-matched second-harmonic generation in submicrometer periodically poled flux-grown ktiopo4.* Applied Physics Letters **86**(18), 181105 (2005).

[122] A. Ganany, A. Arie, and S. Saltiel. *Quasi-phase matching in linbo3 using nonlinear coefficients in the xy plane.* Applied Physics B **85**(1), 97 (2006). 83

[123] O. Gayer, Z. Sacks, E. Galun, and A. Arie. *Temperature and wavelength dependent refractive index equations for mgo-doped congruent and stoichiometric linbo3.* Applied Physics B **91**(2), 343 (2008).

[124] M. Pysher, A. Bahabad, P. Peng, A. Arie, and O. Pfister. *Quasi-phase-matched concurrent nonlinearities in periodically poled ktiopo¡ sub¿ 4¡/sub¿ for quantum computing over the optical frequency comb.* Optics letters **35**(4), 565 (2010).

[125] A. Zukauskas, N. Thilmann, V. Pasiskevicius, F. Laurell, and C. Canalias. *5 mm thick periodically poled rb-doped ktp for high energy optical parametric frequency conversion.* Optical Materials Express **1**(2), 201 (2011).

[126] A. Dot, A. Borne, B. Boulanger, P. Segonds, C. Félix, K. Bencheikh, and J. A. Levenson. *Energetic and spectral properties of triple photon downconversion in a phase-matched ktiopo¡ sub¿ 4¡/sub¿ crystal.* Optics letters **37**(12), 2334 (2012).

[127] H. Lee, H. Kim, M. Cha, and H. Moon. *Simultaneous type-0 and type-ii spontaneous parametric down-conversions in a single periodically poled ktiopo4 crystal.* Applied Physics B **108**(3), 585 (2012). 83, 106

[128] N. Broderick, G. Ross, H. Offerhaus, D. Richardson, and D. Hanna. *Hexagonally poled lithium niobate: a two-dimensional nonlinear photonic crystal.* Physical review letters **84**(19), 4345 (2000). 83, 104, 106

[129] Y. Sheng, J. Dou, B. Cheng, and D. Zhang. *Effective generation of red-green-blue laser in a two-dimensional decagonal photonic superlattice.* Applied Physics B **87**(4), 603 (2007). 83, 106, 108, 111, 112, 118

[130] Q. Chen and W. Risk. *Periodic poling of ktiopo4 using an applied electric field.* Electronics Letters **30**(18), 1516 (1994). 83

[131] H. Karlsson and F. Laurell. *Electric field poling of flux grown ktiopo4.* Applied physics letters **71**(24), 3474 (1997). 83

[132] A. Peña, B. Ménaert, B. Boulanger, F. Laurell, C. Canalias, V. Pasiskevicius, P. Segonds, C. Félix, J. Debray, S. Pairis, *et al. Template-growth of periodically domain-structured ktiopo¡ sub¿ 4¡/sub¿[invited].* Optical Materials Express **1**(2), 185 (2011). 83

[133] Y. Furuhata and K. Toriyama. *New liquid-crystal method for revealing ferroelectric domains.* Applied Physics Letters **23**(7), 361 (1973). 84

[134] J. Fousek, M. Safrankova, and J. Kaczer. *A new dew method for revealing ferroelectric domains.* Applied Physics Letters **8**(8), 192 (1966). 84

[135] G. Pearson and W. Feldmann. *Powder-pattern techniques for delineating ferroelectric domain structures.* Journal of Physics and Chemistry of Solids **9**(1), 28 (1959). 84

[136] J. Hatano, F. Suda, and H. Futama. *Improved powder-pattern technique for delineating ferroelectric domains.* Japanese Journal of Applied Physics **12**(10), 1644 (1973). 84

[137] M. Qi, N. Tikhomirova, and L. Shuvalov. *Investigation of switching processes in laminar domain structure in triglycine sulfate crystal doped with l-and d-alanine by the liquid-crystal method.* Journal of applied physics **79**(6), 3188 (1996). 84

[138] J. A. Hooton and W. J. Merz. *Etch patterns and ferroelectric domains in batio$_3$ single crystals.* Physical Review **98**(2), 409 (1955). 84

[139] H. Stadler and P. Zachmanidis. *Nucleation and growth of ferroelectric domains in batio3 at fields from 2 to 450 kv/cm.* Journal of Applied Physics **34**(11), 3255 (1963).

[140] H. Stadler. *Etched hillocks in batio3.* Journal of Applied Physics **34**(3), 570 (1963). 84

[141] G. Rosenman, A. Skliar, Y. Lareah, N. Angert, M. Tseitlin, M. Roth, M. Oron, and M. Katz. *Asymmetric secondary electron emission flux in ferroelectric ktiopo4 crystal.* Journal of applied physics **80**(12), 7166 (1996). 84

[142] S. Zhu and W. Cao. *Imaging of 180 ferroelectric domains in litao 3 by means of scanning electron microscopy.* physica status solidi(a) **173**(2), 495 (1999).

[143] S. Zhu and W. Cao. *Direct observation of ferroelectric domains in lita o 3 using environmental scanning electron microscopy.* Physical review letters **79**(13), 2558 (1997). 84

[144] B. Zhang, F. Jiang, Y. Yang, Q. Yin, and S. Kojima. *Electron acoustic imaging of batio3 single crystals.* Journal of applied physics **80**(3), 1916 (1996). 85

[145] X. Liu, R. Heiderhoff, H. Abicht, and L. Balk. *Scanning near-field acoustic study of ferroelectric batio3 ceramics.* Journal of Physics D: Applied Physics **35**(1), 74 (2002). 85

[146] M. Zurbuchen, G. Asayama, D. Schlom, and S. Streiffer. *Ferroelectric domain structure of srbi 2 nb 2 o 9 epitaxial thin films.* Physical review letters **88**(10), 107601 (2002). 85

[147] Y. Ding, J. Liu, and Y. Wang. *Transmission electron microscopy study on ferroelectric domain structure in srbi2ta2o9 ceramics.* Applied physics letters **76**(1), 103 (2000).

[148] Y. Li, L. Chen, G. Asayama, D. Schlom, M. Zurbuchen, and S. Streiffer. *Ferroelectric domain structures in srbi2nb2o9 epitaxial thin films: Electron microscopy and phase-field simulations.* Journal of applied physics **95**(11), 6332 (2004). 85

[149] T. Jungk and E. Soergel. *Depth-resolved analysis of ferroelectric domain structures in bulk linbo$_3$ crystals by scanning force microscopy.* Applied Physics Letters **86**(24), 242901 (2005). 85

[150] M. Abplanalp, L. Eng, and P. Günter. *Mapping the domain distribution at ferroelectric surfaces by scanning force microscopy.* Applied Physics A: Materials Science & Processing **66**, S231 (1998).

[151] B. J. Rodriguez, R. Nemanich, A. Kingon, A. Gruverman, S. Kalinin, K. Terabe, X. Liu, and K. Kitamura. *Domain growth kinetics in lithium niobate single crystals studied by piezoresponse force microscopy.* Applied Physics Letters **86**(1), 012906 (2005).

[152] T. Jungk, Á. Hoffmann, and E. Soergel. *Contrast mechanisms for the detection of ferroelectric domains with scanning force microscopy.* New Journal of Physics **11**(3), 033029 (2009). 104, 106

[153] C. Sones, C. Valdivia, J. Scott, S. Mailis, R. Eason, D. Scrymgeour, V. Gopalan, T. Jungk, and E. Soergel. *Ultraviolet laser-induced sub-micron periodic domain formation in congruent undoped lithium niobate crystals.* Applied Physics B **80**(3), 341 (2005). 85

[154] Y. Lu, T. Wei, F. Duewer, Y. Lu, N.-B. Ming, P. Schultz, and X.-D. Xiang. *Nondestructive imaging of dielectric-constant profiles and ferroelectric domains with a scanning-tip microwave near-field microscope.* Science **276**(5321), 2004 (1997). 85

[155] V. Bhide and N. Bapat. *Interferometric study of domain structure in barium titanate.* Physica **27**(6), 531 (1961). 85

[156] M. Canut and R. Hosemann. *X-ray analysis of ferroelectric domains in the paraelectric phase of nano2.* Acta Crystallographica **17**(8), 973 (1964). 85

[157] S. Kim, V. Gopalan, and B. Steiner. *Direct x-ray synchrotron imaging of strains at 180 domain walls in congruent linbo 3 and litao 3 crystals.* Applied Physics Letters **77**(13), 2051 (2000).

[158] V. Antipov, A. Blistanov, E. Roshchupkina, R. Tucoulou, L. Ortega, and D. Roshchupkin. *High-resolution x-ray topography and diffraction study of bulk regular domain structures in linbo 3 crystals.* Applied physics letters **85**(22), 5325 (2004). 85

[159] S. MacCormack and J. Feinberg. *Revealing 180 domains in ferroelectric crystals by photorefractive beam coupling.* Applied optics **35**(30), 5961 (1996). 85

[160] S. I. Bozhevolnyi, K. Pedersen, F. Laurell, H. Karlsson, T. Skettrup, M. Belmonte, *et al. Second-harmonic imaging of ferroelectric domain walls.* Applied physics letters **73**(13), 1814 (1998). 85, 86

[161] S. Kurimura and Y. Uesu. *Application of the second harmonic generation microscope to nondestructive observation of periodically poled ferroelectric domains in quasi-phase-matched wavelength converters.* Journal of applied physics **81**(1), 369 (1997). 86

[162] J. Harris, G. Norris, and G. McConnell. *Characterisation of periodically poled materials using nonlinear microscopy.* Optics express **16**(8), 5667 (2008).

[163] Y. Uesu, H. Yokota, S. Kawado, J. Kaneshiro, S. Kurimura, and N. Kato. *Three-dimensional observations of periodically poled domains in a litao 3 quasiphase matching crystal by second harmonic generation tomography.* Applied Physics Letters **91**(18), 182904 (2007). 85

[164] S. Kluge, F. Budde, I. Dohnke, P. Rechsteiner, and J. Hulliger. *Phase-sensitive second-harmonic microscopy reveals polarity of topologically centrosymmetric molecular crystals.* Applied physics letters **81**(2), 247 (2002). 85

[165] B. Zwicker and P. Scherrer. *Elektrooptische eigenschaften der seignette-elektrischen kristalle kh 2 po 4 und kd 2 po 4.* Helv. Phys. Acta **17**, 346 (1944). 85

[166] W. J. Merz. *Domain formation and domain wall motions in ferroelectric bati o 3 single crystals.* Physical Review **95**(3), 690 (1954). 85

[167] M. Müller, E. Soergel, M. Wengler, and K. Buse. *Light deflection from ferroelectric domain boundaries.* Applied Physics B **78**(3-4), 367 (2004). 85

[168] M. Muller, E. Soergel, K. Buse, C. Langrock, and M. Fejer. *Investigation of periodically poled lithium niobate crystals by light diffraction.* Journal of applied physics **97**(4), 44102 (2005).

[169] S. Grilli, P. Ferraro, M. Paturzo, D. Alfieri, P. De Natale, M. de Angelis, S. De Nicola, A. Finizio, and G. Pierattini. *In-situ visualization, monitoring and analysis of electric field domain reversal process in ferroelectric crystals by digital holography.* Optics express **12**(9), 1832 (2004). 85

[170] B. Sugg, F. Kahmann, R. Pankrath, and R. Rupp. *Observation of ferroelectric 180 domains by microphotometry of holographic gratings.* Applied optics **33**(23), 5386 (1994). 85

[171] K. Buse, J. Imbrock, E. Krätzig, and K. Peithmann. *Photorefractive effects in linbo3 and litao3.* In *Photorefractive Materials and Their Applications 2*, pp. 83–126 (2007). 85

[172] M. De Angelis, S. De Nicola, A. Finizio, G. Pierattini, P. Ferraro, S. Grilli, and M. Paturzo. *Evaluation of the internal field in lithium niobate ferroelectric domains by an interferometric method.* Applied physics letters **85**(14), 2785 (2004). 85

[173] M. Wengler, M. Müller, E. Soergel, and K. Buse. *Poling dynamics of lithium niobate crystals.* Applied Physics B **76**(4), 393 (2003). 85

[174] S. M. Saltiel, Y. Sheng, N. Voloch-Bloch, D. N. Neshev, W. Krolikowski, A. Arie, K. Koynov, and Y. S. Kivshar. *Cerenkov-type second-harmonic generation in two-dimensional nonlinear photonic structures.* IEEE Journal of Quantum Electronics **45**(11), 1465 (2009). 85, 107

[175] S. Wemple and M. DiDomenico Jr. *Theory of the elasto-optic effect in nonmetallic crystals.* Physical Review B **1**(1), 193 (1970). 102

[176] S. Bernhardt, L. Mize, P. Delaye, and G. Roosen. *Evaluation of electro-optic, elasto-optic, piezoelectric, and elastic coefficients of ba 0.77 ca 0.23 tio 3 through orientation dependent photorefractive beam coupling.* Journal of applied physics **92**(10), 6139 (2002). 102

[177] P. Ni, B. Ma, X. Wang, B. Cheng, and D. Zhang. *Second-harmonic generation in two-dimensional periodically poled lithium niobate using second-order quasiphase matching.* Applied physics letters **82**(24), 4230 (2003). 106

[178] R. Lifshitz, A. Arie, and A. Bahabad. *Photonic quasicrystals for nonlinear optical frequency conversion.* Physical review letters **95**(13), 133901 (2005).

[179] N. G. Broderick, R. T. Bratfalean, T. M. Monro, D. J. Richardson, and C. M. De Sterke. *Temperature and wavelength tuning of second-, third-, and fourth-harmonic generation in a two-dimensional hexagonally poled nonlinear crystal.* JOSA B **19**(9), 2263 (2002). 106

[180] S. M. Russell, P. E. Powers, M. J. Missey, and K. L. Schepler. *Broadband*

mid-infrared generation with two-dimensional quasi-phase-matched structures. Quantum Electronics, IEEE Journal of **37**(7), 877 (2001).

[181] R. T. Bratfalean, A. C. Peacock, N. G. Broderick, K. Gallo, and R. Lewen. *Harmonic generation in a two-dimensional nonlinear quasi-crystal.* Optics letters **30**(4), 424 (2005).

[182] A. Bahabad, A. Ganany-Padowicz, and A. Arie. *Engineering two-dimensional nonlinear photonic quasi-crystals.* Optics letters **33**(12), 1386 (2008). 106

[183] W. Sohler and H. Suche. *Erbium-doped lithium niobate waveguide devices.* OPTICAL ENGINEERING-NEW YORK-MARCEL DEKKER INCORPORATED- **66**, 127 (1999). 109

[184] R. Weis and T. Gaylord. *Lithium niobate: summary of physical properties and crystal structure.* Applied Physics A **37**(4), 191 (1985). 109, 110, 130

[185] K.-K. Wong. *Properties of lithium niobate.* 28 (IET, 2002). 109, 110

[186] S. Abrahams, H. Levinstein, and J. Reddy. *Ferroelectric lithium niobate. 5. polycrystal x-ray diffraction study between 24 and 1200 c.* Journal of Physics and Chemistry of Solids **27**(6), 1019 (1966). 109

[187] H. D. Megaw. *A note on the structure of lithium niobate, linbo3.* Acta Crystallographica Section A: Crystal Physics, Diffraction, Theoretical and General Crystallography **24**(6), 583 (1968). 109

[188] P. Lenzo, E. Spencer, and K. Nassau. *Electro-optic coefficients in single-domain ferroelectric lithium niobate.* JOSA **56**(5), 633 (1966). 111

[189] E. Turner. *High-frequency electro-optic coefficients of lithium niobate.* Applied Physics Letters **8**(11), 303 (1966). 111

[190] J. Hulliger, P. Langley, and S. Roth. *A new design strategy for efficient electro-optic single-component organic crystals.* Crystal engineering **1**(3), 177 (1998). 125

[191] A. Quintel, S. W. Roth, J. Hulliger, and M. Wübbenhorst. *3d imaging and simulation of the polarisation distribution in molecular crystals.* Molecular Crystals and Liquid Crystals **338**(1), 243 (2000). 125

[192] H. Gerlach. *A new method for measuring electrooptic constants at high frequencies.* Applied physics **1**(5), 279 (1973). 130

[193] M. Okazaki, T. Chichibu, S. Yoshimoto, T. Inoue, and T. Suhara. *Electrooptic bragg deflection modulator for uv laser light using periodically poled mgo: s-litao.* Photonics Technology Letters, IEEE **23**(22), 1709 (2011). 136

[194] A. L. Hodgkin and A. F. Huxley. *Action potentials recorded from inside a nerve fibre.* Nature **144**(3651), 710 (1939). 139

[195] R. Llinas and M. Sugimori. *Electrophysiological properties of in vitro purkinje cell somata in mammalian cerebellar slices.* The Journal of Physiology **305**(1), 171 (1980).

[196] B. Sakmann and E. Neher. *Patch clamp techniques for studying ionic channels in excitable membranes.* Annual review of physiology **46**(1), 455 (1984). 139

[197] D. Ze&cbreve *et al. Multiple spike-initiation zones in single neurons revealed by voltage-sensitive dyes* (1996). 139

[198] P. Theer, W. Denk, M. Sheves, A. Lewis, and P. B. Detwiler. *Second-harmonic generation imaging of membrane potential with retinal analogues.* Biophysical journal **100**(1), 232 (2011). 139